Acoustics and optimisation of vibration attenuation of composite structures through banded behaviour.

Submitted for the Degree of Ph.D., APRIL 2019

by **Theofanis Ampatzidis**

Composites Group, Faculty of Engineering,

University of Nottingham

Supervisors: Dr. Dimitrios Chronopoulos (Primary),

Prof. Seamus Garvey, Prof. Shuguang Li


The University of
Nottingham

Contents

List of Figures **3**

Abstract **10**

1 Introduction **3**

1.1 Aim and objectives 8

1.2 Publications 9

1.3 Thesis outline 10

2 Literature review **12**

2.1 Wave propagation methods 12

2.1.1 Analytical methods 12

2.1.2 Finite Element(s) methods 17

2.2 Damping enhancement methods 22

2.3 Band gap engineering 25

2.4 Band gap and additive manufacturing 29

2.5 Band gap optimisation 30

2.6 Sandwich structures 31

2.7 Conclusion 33

3 Methodology **35**

3.1 Periodic structure theory 35

3.1.1 The two dimensional WFEM 38

3.1.2 Loss factor 41

3.2 Computation of the energy analysis quantities 42

3.2.1 Calculation of the modal density 42

3.2.2 Calculation of the radiation efficiency 43

3.2.3 Energy analysis 43

3.3 Script's structure 47

3.4 Optimisation 49

3.5 Experimental setup 52

4 Pre-stressed composite structures **55**

4.1 Introduction 55

4.2 Numerical results 56

4.2.1 Monolithic laminate - Tensioned and Compressed . . 57

4.2.2 Sandwich laminate 58

4.3 Concluding remarks 69

5 Band gap sandwich structures **71**

5.1 Introduction 71

5.2 Case study 1 71

5.2.1 Results 73

5.2.2 Conclusion and further work 76

5.3 Case study 2 77

5.3.1 Proposed core architecture 77

5.3.2 Experimental and numerical validation 81

5.4 Concluding remarks 87

6 Band gap AM composite structures **88**

6.1 Introduction 88

6.2 Numerical results 90

6.3 Parametric analysis 93

6.4 FEA and experiment 96

6.5 Concluding remarks 99

7 Conclusions and Future Work **101**

7.1 Conclusions 101

7.2 Contribution to knowledge and potential industrial applications 103

7.3 Future work 104

Bibliography **107**

List of Figures

1.1 Typical vibration isolators, used to isolate vibrating parts from the structure, such as a car's internal combustion engine. 3

1.2 Displacement transmissibility graph of a mass-damper-spring system, like the isolator seen above. γ is the damping coefficient and Ω the ratio of the frequency ω over the resonant frequency ω_r. [1] 4

1.3 Schematic representation of constrained and unconstrained damping layers and their operating principle (retrieved from http://en.vibratec.se/constrained-free-layer-damping/). . . 5

1.4 The structural response of a band gap mass-spring structure and the examination of the effect of the number of periodic unit cells on vibration attenuation in band gap region (the band gap is observed between the two dashed vertical lines) [2]. 7

2.1 Force and moment resultants on a plate element. 13

2.2 SEA and FEM analysis strategy in aerospace research area [3]. 17

2.3 Finite elements mesh of 1D waveguide. [4] 18

2.4 DOFs of two-dimensional model of periodic structure. 19

2.5 Schematic representation of the examined beams in [5]. The procedure of building the unit cell model is depicted. 21

2.6 Hybrid composite pyramidal truss sandwich panel (and its unit cell) examined in [6], presenting enhanced damping capacity. 24

2.7 One-dimensional periodic model examined by Newton representing the mechanics of the particles of a continuous body. . 26

2.8 A schematic representation of a phononic crystal, made of a square lattice of finite cylinders deposited on a homogeneous plate. All the dimensions are less than 1 mm. [7] 27

2.9 3D printed band gap structure as examined in [8]. 29
2.10 A representative result of the phononic band gap optimization is shown as examined in [9]. 30
2.11 Sandwich beam with periodic honeycomb core and unit cell, as examined in [10]. 31
2.12 Graphic representation of a sandwich beam with internal resonators [11]. 32

3.1 Several schemes of periodic structures. 35
3.2 The employed FE model for investigation of 1D wave propagation. 36
3.3 Representation of the modelled internally pressurised periodic segment with its edges 1, 2, 3 and 4 38
3.4 Representation of the considered SEA model and all the energy and power exchanges between the systemts of the model. 44
3.5 Flow diagram of the master script used to acquire wave propagation characteristics of the examined structures. The text boxes with dashed lines are ANSYS processes while the rest of them are MATLAB ones. 48
3.6 Flow chart of the optimisation method. The method takes advantage of the fast calculation of wave propagation thanks to the master script and finds the optimal solution quicker than the full method when the whole model has to be solved. 49
3.7 The design of the vibration experiment rig with key dimensions (in mm). 52
3.8 Polytec PDV-100 single point laser vibrometer. 53
3.9 TBS K2007E1 electrodynamic shaker with internal amplifier, along with the impedance head (PCB 288D01). 53
3.10 View of the vibration setup, including: 1) the rig made of aluminium profiles, 2) the TBS K2007E1 electrodynamic shaker along with the impedance head (PCB 288D01) , 3) the Polytec VIB-E-400 Junction Box and 4) the Polytec PDV-100 single point laser vibrometer. 54

3.11 Graph of the vibration experiment process: 1) The Junction Box (A) generates the signal to excite the shaker (B). 2) The impedance head (C) gives as output the force acted on the specimen. 3) The laser vibrometer (E) measures the velocity, hence the acceleration of the specimen (D). 4) The desktop PC (F) handles the data and generates the relevant graphs as seen in the next sections. 54

4.1 The examined laminate with a periodic cell of it, where its nodes and dimensions' symbols can be seen. 56

4.2 Comparison of the bending wavenumber (x-direction) of the monolithic laminate: (-) non-stressed, (x) pre-stressed, tensile force $T = 100$ N in x direction, (o) pre-stressed, compressive force $T = -100$ N in x direction 59

4.3 Comparison of the loss factor of the monolithic laminate: (-) non-stressed, (x) pre-stressed, tensile force $T = 100$ N in x direction, (o) pre-stressed, compressive force $T = -100$ N in x direction 59

4.4 Comparison of the modal density of the monolithic laminate: (-) non-stressed, (x) pre-stressed, tensile force $T = 100$ N in x direction, (o) pre-stressed, compressive force $T = -100$ N in x direction 60

4.5 Comparison of the radiation efficiency of the monolithic laminate: (-) non-stressed, (x) pre-stressed, tensile force $T = 100$ N in x direction, (o) pre-stressed, compressive force $T = -100$ N in x direction 60

4.6 Comparison of the transmission loss of the monolithic laminate: (-) non-stressed, (x) pre-stressed, tensile force $T = 100$ N in x direction, (o) pre-stressed, compressive force $T = -100$ N in x direction 61

4.7 Representation of the sandwich laminate under consideration and its dimensions' symbols. 61

4.8 Comparison of the bending wavenumber (x-direction) of the sandwich plate: (-) non-stressed, (x) pre-stressed, tensile force $T = 100$ N in x direction, (o) pre-stressed, compressive force $T = -100$ N in x direction 62
4.9 Comparison of the loss factor of the sandwich plate: (-) non-stressed, (x) pre-stressed, tensile force $T = 100$ N in x direction, (o) pre-stressed, compressive force $T = -100$ N in x direction 63
4.10 Comparison of the modal density of the sandwich plate: (-) non-stressed, (x) pre-stressed, tensile force $T = 100$ N in x direction, (o) pre-stressed, compressive force $T = -100$ N in x direction 63
4.11 Comparison of the radiation efficiency of the sandwich plate: (-) non-stressed, (x) pre-stressed, tensile force $T = 100$ N in x direction, (o) pre-stressed, compressive force $T = -100$ N in x direction 64
4.12 Comparison of the transmission loss of the sandwich plate: (-) non-stressed, (x) pre-stressed, tensile force $T = 100$ N in x direction, (o) pre-stressed, compressive force $T = -100$ N in x direction 64
4.13 Representation of the internally pressurised sandwich laminate. As it is shown, the pressure is asked on the skins of the sandwich. 65
4.14 Comparison of the bending wavenumber (x-direction) of the sandwich plate: (-) non-pressurised, (x) pre-stressed, internal pressure $p = 1$ MPa, (o) pre-stressed, internal pressure $p = 10$ MPa 66
4.15 Comparison of the loss factor of the sandwich plate: (-) non-pressurised, (x) pre-stressed, internal pressure $p = 1$ MPa, (o) pre-stressed, internal pressure $p = 10$ MPa 66

4.16 Comparison of the modal density of the sandwich plate: (-) non-pressurised, (x) pre-stressed, internal pressure $p = 1$ MPa, (o) pre-stressed, internal pressure $p = 10$ MPa 67
4.17 Comparison of the radiation efficiency of the sandwich plate: (-) non-pressurised, (x) pre-stressed, internal pressure $p = 1$ MPa, (o) pre-stressed, internal pressure $p = 10$ MPa 68
4.18 Comparison of the transmission loss of the sandwich plate: (-) non-pressurised, (x) pre-stressed, internal pressure $p = 1$ MPa, (o) pre-stressed, internal pressure $p = 10$ MPa 68
4.19 Comparison of the transmission loss of the sandwich plate: (-) non-stressed, (x) pre-stressed, internal pressure $p = 1$ MPa, (o) pre-stressed, internal pressure $p = 10$ MPa, (+) pre-stressed, tensile force T=100N 69
4.20 Comparison of the transmission loss of the sandwich plate: (-) non-stressed, (x) pre-stressed, internal pressure $p = 1$ MPa, (o) pre-stressed, internal pressure $p = 10$ MPa, (+) pre-stressed, tensile force $T = 100$ N 70

5.1 Infinite beam with periodic cell. 72
5.2 Left: Geometry of infinite beam. Right: Pressure applied in the hollow part of the core. 72
5.3 Graphs of the flexural waves of the first three *Ratios* with no pressure applied on the skins. 74
5.4 Graphs of the flexural waves of the last two *Ratios* with no pressure applied on the skins. 75
5.5 Geometry of the core of the scheme 1 and 2 unit cells. 78
5.6 Skin and core of scheme 1 and 2 specimen. 79
5.7 Schematic representation of the cantilever beam simulation used to compare bending stiffness. 80
5.8 Flexural wave propagation of scheme 1 (.) and regular sandwich beam (x). The shaded area represents the bending band gap. 81

5.9 Flexural wave propagation of scheme 2 (.) and regular sandwich beam (x). The shaded area represents the bending band gap. 82
5.10 Left: The points that are examined in the experimental procedure and FE analyses. The point of excitation is marked as 'X'. Right: the points that are measured during the vibration experiment. 82
5.11 The two core schemes as manufactured. The cores are then cemented on cured carbon fibre sheets. 83
5.12 Frequency response function (FRF) of FEA (-o) and experimental results (–) of all the measured points of scheme 1. The points of the line connecting the FEA graphs consists of the middle value of the band gap. 84
5.13 FRF of FEA (-o) and experimental results (–) of all the measured points of scheme 2. The points of the line connecting the FEA graphs consists of the middle value of the band gap. 84
5.14 Scheme 1 experimental (–) and FEA (-o) results of point 10. 85
5.15 Scheme 2 experimental (–) and FEA (-o) results of point 10. 85
5.16 FEA of scheme 1 at 2430 Hz (displacements in meters). . . . 86
5.17 FEA of scheme 2 at 2000 Hz (displacements in meters). . . . 86

6.1 Schema of periodic beam and unit cell. 89
6.2 Cost functions used in the optimisation method. 90
6.3 Pyramid frustum (left) and trapezoid (right). 91
6.4 Wave numbers of the numerical analysis of the beam with geometric characteristics given by the optimal parameters. The shaded area represents the band gap. 92
6.5 Parametric analysis results of further cases with t_{st} out of the optimisation limits, $t_{st} \in [0.021\text{ m}, 0.030\text{ m}]$ and $l_{top} \in [0.005\text{ m}, 0.025\text{ m}]$. 94
6.6 Objective function of the optimisation as calculated using the parametric analysis results ($t_{st} \in [0.005\text{ m}, 0.030\text{ m}]$ and $l_{top} \in [0.005\text{ m}, 0.025\text{ m}]$). 94

6.7 Relation of the optimised variables m, b_s, b_g and $b_g_{m_f}$ with regards to parameters t_{st} and l_{top} ($t_{st} \in [0.005\text{ m}, 0.030\text{ m}]$ and $l_{top} \in [0.005\text{ m}, 0.025\text{ m}]$). 95
6.8 Representation of simulation of the experiment. The same logic is followed in all beam simulations, with the excitation force being asked always on the lowest, middle point of one edge and the response on the highest, middle point of the opposite edge. 97
6.9 FRF of FEA of hybrid composite beam with: (-.) 5 unit cells, (–) 10 unit cells, (- -) 15 unit cells. The shaded area represents the numerically calculated band gap. 97
6.10 Experimental setup of the vibration testing. The setup is specifically designed and manufactured to accomodate small specimens for vibration testing. 98
6.11 The points at which the FRF graphs are presented. Each point's number is indicative of the number of the unit cells. . 98
6.12 Experimental and FEA results of the FRF of point 1 where (–) is FRF of experimental results and (- -) is the FEA results. 99
6.13 Experimental and FEA results of the FRF of point 3 where (–) is FRF of experimental results and (- -) is the FEA results. 99
6.14 Experimental and FEA results of the FRF of point 5 where (–) is FRF of experimental results and (- -) is the FEA results..100

Abstract

Noise and vibration transmission within payload and passenger compartments is a major issue for modern transport vehicles. To ensure the quality of their products, manufacturers in the transport industry are simultaneously trying to optimise the mechanical and the vibroacoustic performance of structural assemblies. In the same time, current research in most industries focuses on materials that offer low density along with superior dynamic and static performance. This goal has led to increasing use of sandwich structures and composite materials in general, whose high stiffness-to-weight ratio along with the tailoring of their properties make them quite appealing. This property, though, comes with a significant cost in their vibroacoustic behaviour, being responsible for high noise and displacement resonant vibrations. Prompted by that, elevated quality and quantity of research is about modelling the behaviour of these materials, along with conventional ones, using time and cost-efficient computational methods. These methods are used to reach the goal of enhanced stiffness, weight and vibration performance. Using efficient tools developed for the aforementioned methods, it has been demonstrated that judiciously designed periodic structures can induce vibration attenuation and stop-band behaviour in specific frequency ranges (so-called *band gaps* or *stop bands*). The mechanisms that generate band gaps, though, usually do not leave the structure's stiffness unaffected, which renders it incapable of bearing loads.

In this work the potential of the application of banded schemes on load bearing structures is examined. Special care is taken so that the designs are easy-to-manufacture and plausible to be industrialised. For this to be achieved several steps are followed with each one preparing the ground for the next one. Firstly, the necessary computational tools are developed using periodic structure theory, wave finite element method and commercially available finite element software package and the effect of the prestress on acoustic and damping performance of composite monolithic and

sandwich laminates is examined. It is shown that pre-stress (both tension/compression and pressure) must be taken into consideration when a structure is designed to achieve vibroacoustics targets and produce reliable predictions. Then, having developed the initial form of mathematical and programming tools, the banded behaviour of sandwich beams is calculated. Three different case studies are considered, with the first one being non-structural and the rest two being capable of bearing loads. This part of the work proves that unconventional but easy-to-manufacture core architectures can demonstrate banded behaviour, which makes it a lightweight and easily industrialised solution with possible high-volume applications. A rig is designed and manufactured, and a vibration experimental setup is developed consisting of an electrodynamic shaker and a single-point laser vibrometer. This setup is used to validate the numerical and finite element calculations. It is also demonstrated that band gaps can be achieved in load bearing structures, an observation which leads to the third part of the work. Having developed a more efficient version of computational tools, the master script, a way to examine numerous solutions is aimed for. Hence, a multi-disciplinary optimisation algorithm is developed which uses the master script and optimisation method to calculate the optimal solution for the geometry of a banded structure. An optimal geometry of a one-dimensional composite beam with additive manufactured stiffener is acquired, whose banded behaviour is experimentally verified.

In brief, this research produces designs and manufactures specimens of one-dimensional band gap structures capable of being load-bearing part of a structure. This is achieved by developing efficient multi-disciplinary optimisation tools and experimentally validating the results by developing a vibration testing setup.

Acknowledgements

First of all, I would like to thank my main supervisor, Dr. Chronopoulos for his guidance and support. If it was not himself I am sure I would not have been able to produce even a chapter. Additionally, I would like to thank all the people of the Composites Group for helping me with my progress and for all the technical support they provided to me. Special thanks to Petros, Wahyudin and Waiel for their help with the Metrology lab, and also to Prof. Leach and Prof. Tuck for the technical support with my research.

Now for the most important part of my acknowledgements: I would be nothing without my friends and my family. They say friends is the family you choose. Well, I could not have chosen better brothers and parents than I have... And my friends, all of them made me who I am through the years, and this includes this PhD, which would not even be a word, a letter without them.

Abbreviations

1D, 2D, 3D	one-, two- and three-dimensional
AM	Additive manufacturing
CLPT	Classical laminate plate theory
FE	Finite elements
FEA	Finite elements analysis
FFT	Fast Fourier transform
FRF	Frequency response function
FSDT	First-order shear deformation theory
HSDT	High-order shear deformation theory
PST	Periodic structure theory
PVB	Polyvinyl butyral
PVC	Polyvinyl chloride
SEA	Statistical energy analysis
SFE	Spectral finite element
STL	sound transmission loss
TL	Transmission loss
TM	Transfer matrix
WFEM	Wave finite element method

.

Chapter 1: Introduction

According to the Oxford Dictionary, vibration is defined as *an oscillation of the parts of a fluid or an elastic solid whose equilibrium has been disturbed*, where oscillation is defined as *regular variation in magnitude or position about a central point*. Most of the times vibration is undesirable and it consists one of the main issues transport vehicles' industry deal with, especially the noise and vibration transmission within payload and passenger compartment. Vibrations can inconveniently be caused by many sources, such as unbalanced rotating masses, airborne vibration or even natural phenomena, such as earthquake. Across the years humans have tried to overcome these problems using several methods, e.g. vibration isolators, damping treatment, mass dampers and active control. Each one of those solutions have their advantages and disadvantages which need to be considered before their application.



Figure 1.1: Typical vibration isolators, used to isolate vibrating parts from the structure, such as a car's internal combustion engine.

Typical vibration isolators, like the ones shown in Fig. 1.1, are usually made from a plastic material with high damping properties. The use of these parts is to isolate the vibrations from the structure by reducing the resonant frequency and adding damping to the structure to decrease the vibration amplitude near the resonance frequency area. This kind of isolators are widely used in automotive applications to isolate the power unit vibration from the chassis avoiding this way the deterioration of the passengers'

comfort with research focusing on optimisation of the isolators efficiency [12, 13]. Nevertheless, this method requires low stiffness which leads to high static displacements and decreased robustness, a characteristic that is crucial for the structural integrity of the assembly. Additionally, as it can be seen in Fig. 1.2, which illustrates the displacement transmissibility of a single degree system, as damping increases the vibration amplitude increases in high frequencies. Displacement transmissibility is the ratio of the absolute displacement of the mass over the displacement of the base on which the spring is connected, which essentially shows the degree that the mass' displacement is decreased compared to the base's.

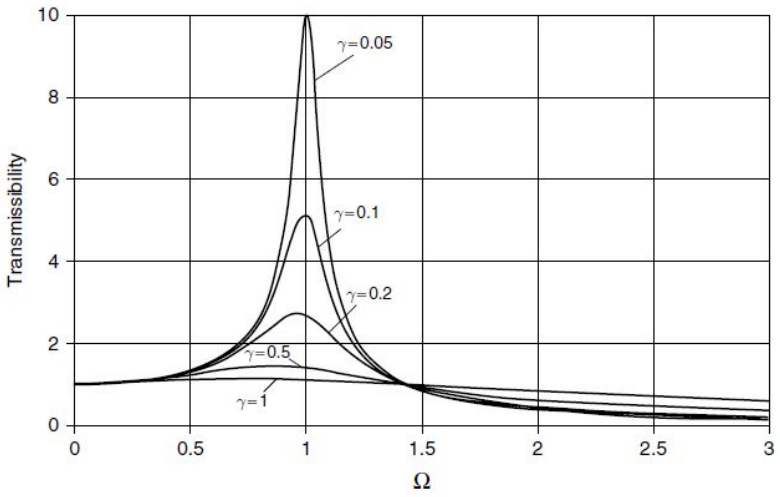


Figure 1.2: Displacement transmissibility graph of a mass-damper-spring system, like the isolator seen above. γ is the damping coefficient and Ω the ratio of the frequency ω over the resonant frequency ω_r. [1]

Staying on the principle of using damping to limit the harmful effects of vibrations, layers of material with enhanced damping properties, such as viscoelastic materials (e.g. polyvinyl butyral [PVB]) are applied on a surface either constrained or unconstrained (see Fig. 1.3). During the vibration these layers are transformed due to shear strain (constrained) or extension (unconstrained) and thanks to their nature, which demonstrates hysteretic behaviour in cyclic loading, mechanical energy is dissipated in the form of heat. The advantage of this vibration damping method is that the only

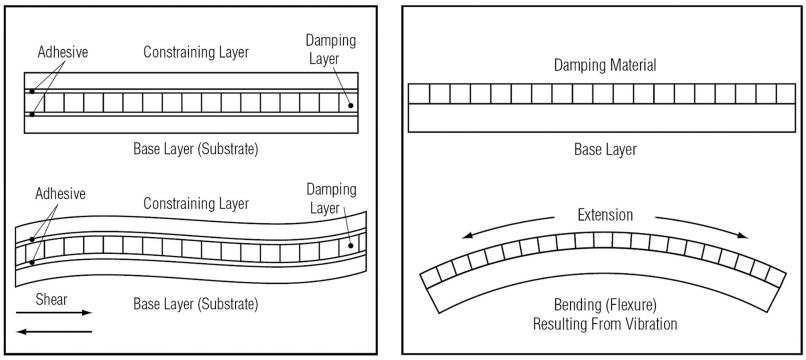


Figure 1.3: Schematic representation of constrained and unconstrained damping layers and their operating principle (retrieved from http://en.vibratec.se/constrained-free-layer-damping/).

limit is the available size of the layer and it is widely used in aerospace and automotive industry [14]. On the other hand, the nature of damping layers is also responsible for the major disadvantage which is the dependency of their efficiency on temperature and humidity. Additionally, in some applications relatively large mass is added using damping layers and on top of that, their performance is not ideal at low frequencies. Nevertheless, research focuses on improving the application of damping layers [15, 16] and employing other methods to enhance the damping of a structure, especially in frequencies where damping layers struggle [17, 18].

Going over damping layers and vibration isolators and thanks to the advance of the technology, engineers have turned their attention to active noise and vibration cancelling using actuators to attenuate or even annihilate the propagation of the vibration in the structure. These systems consist of sensors which 'read' the sound or vibration source and send signals to actuators to produce the 180^o out of phase excitation signal resulting in destructive interference. This technology has been employed for some time now in aerospace [19] where inertial actuators are used while similar technology is observed in automotive industry, where smart panels with piezoelectric actuators following the same principle [20, 21] are utilised. Active vibration control mechanisms, though, consist usually of very expensive and complicated systems which increase significantly the cost and mass of the

structure. Additionally, the complexity of the systems makes it difficult to design and manufacture a highly reliable system with no need of regular service or replacement.

In general the application of vibration isolation measures should be characterised by simplicity of design and mechanism, endurability, high static stiffness and wide range of working frequency band. This combination is quite difficult to achieve without adding significant mass to the structure. In this scope it has been demonstrated that judiciously designed periodic structures can induce vibration attenuation and stop-band behaviour in specific frequency ranges (so-called *band gaps* or *stop bands*, Fig. 1.4) [22]. This periodic structures characteristics are taken advantage off during the design to enhance vibration isolation using simple design with the use of limited or none additional mass or simple lightweight mechanisms in most cases. In this work, banded load-bearing structures with no need of additional mass or mechanisms are examined.

There are two major mechanisms that have been identified to generate band gap behaviour in periodic structures: Bragg scattering and local resonance. Bragg scattering is observed when a structure exhibits periodic impedance mismatches and the waves are scattered at the borders of the unit-cell (the part of the structure that is periodically repeated). This scattering can be caused by means of inclusions, and geometrical or material inconsistencies, and leads to the interaction of the reflected waves with the incoming ones. When specific circumstances are met, this interaction causes the partial or complete annihilation of wave propagation [23, 24]. It can easily be shown that the frequency at which the band gap is observed depends on the length and the material/geometrical mismatch of the unit cell of the periodic structure [25]. This leads to the need for prohibitively large dimensions to achieve low frequency band gaps.

Therefore, researchers' focus was shifted to local resonances [26], where a solid core material with relatively high density is usually preferred, suppressed by an elastically soft material. When this sub-wavelength inclusion/addition resonates, it exhibits behaviour that cancels the propagation

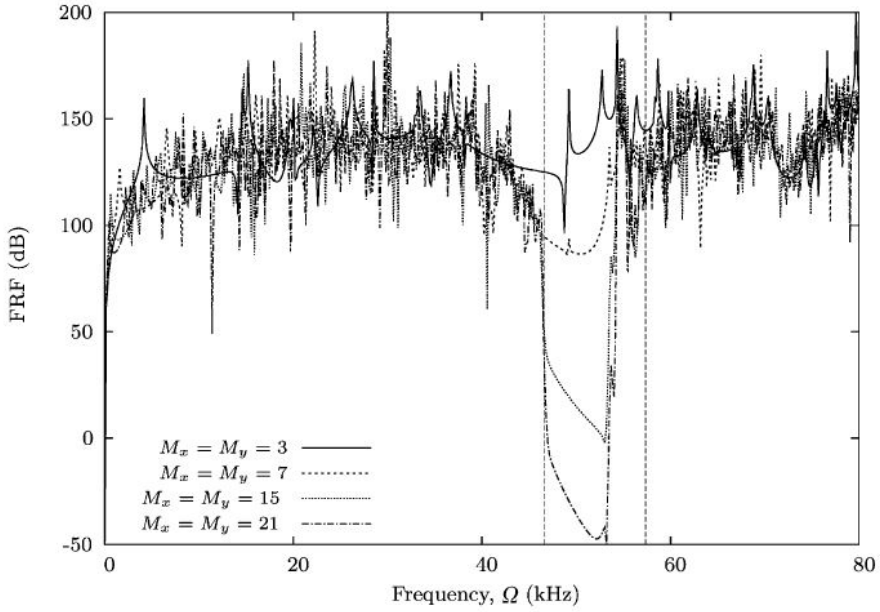


Figure 1.4: The structural response of a band gap mass-spring structure and the examination of the effect of the number of periodic unit cells on vibration attenuation in band gap region (the band gap is observed between the two dashed vertical lines) [2].

of waves, giving rise to effective negative elastic constants or group velocities at certain frequency ranges which are significantly lower than those observed in Bragg scattering. Liu et al. [27] examined the transition between the two band gap production mechanisms and there has been research on coupling of the two mechanisms [8, 28]. This design has been implemented in numerous applications, one of them being the hexagonal chiral lattice examined in [29]. Several physical properties were examined and their influence on the banded behaviour of the lattice was studied, with the writers suggesting the use of the considered lattices in novel phononic meta-materials.

Recently an additional mechanism of band gap generations is gaining interest. This mechanism is called inertial amplification and has been proposed as band gap generator by Yilmaz et al. [30, 31]. In this approach inertial forces are enhanced between two points in a periodic cell of a structure. This way anti-resonance frequencies are generated, where the enhanced inertia cancels the elastic forces. The solution has been examined

in various applications, where it offered wide low-frequency band gaps. In [32] Acar et al. produced numerical and experimental results examining the application of the inertial amplification mechanism in a two-dimensional solid structure. In the same scope Yuksel et al. [33] optimised the shape of phononic band gap structure implementing inertial amplification mechanism and produced wide band gap below 1 kHz. These applications, though, compromised the structural integrity of the final result. Then, in [34, 35] researchers applied the inertial amplification mechanism on load-bearing structures without compromising their stiffness by adding the mechanism on the structure. Nevertheless, in both cases examined in these works the application resulted in additional mass or compromised structural integrity. Another way to categorise band gaps is their application, where the characterisation of *phononic* refers to the periodic structures where elastic wave propagation is cancelled, while *photonic* refers to the electromagnetic counterpart of them. Additional explanation is provided in Sec. 2.3.

As a whole, research on all types of band gaps has been increasing. The majority of the researchers, though, focus on structural parts with high frequency band gaps or non-structural ones with low frequency band gaps. As described above and in the literature review (Sec. 2), the nature of the band gap generating mechanisms renders the low-frequency stop bands in load-bearing structures quite difficult to achieve. Hence, researchers developed a significant number of methodologies, whether they are optimisation algorithms or mathematical tools with improved efficiency and their applications are limited to non-structural parts. Additionally, the produced designs have quite complex geometry which renders the manufacture of large batches costly and nearly impossible. The presented work is aiming to cover the gap in literature.

1.1 Aim and objectives

The aim of this thesis is to examine the application of band gap theory on load-bearing structures which are easy-to-manufacture. By the term

"easy-to-manufacture" the objective to achieve a design which consists of low cost materials and require the smallest possible number of processes to manufacture is stated. As mentioned above, the novelty lies on the fact that there has not been any research on banded structures that contribute to the vibration attenuation and forming a load-bearing part of the structure. Additionally, the work presented in this thesis tried to keep the design limitations on a level that allows the industrialisation of the solution thanks to easy-to-manufacture geometry. The objectives are listed below:

- Development of an algorithm to examine the wave propagation characteristics of periodic structures using periodic structure theory (PST).
- Examination of the effect of pre-stress on the acoustic and damping performance of a composite structure.
- Designing and setting up an experimental method to test the vibration behaviour of small composite structures.
- Examination of both non-structural and load-bearing sandwich composite structures.
- Development of an efficient multi-disciplinary optimisation framework capable of simultaneously optimising static stiffness, mass and band gap behaviour of a composite structure.

1.2 Publications

During this PhD study two conference papers (with one of them being peer-reviewed) and two journal papers were published, and one journal paper is currently under review.

The conference papers are:

- T. Ampatzidis and D. Chronopoulos, *Wave propagation in pressurised composite structures with frequency band gap behaviour*, 2016 Leuven Conference on Noise and Vibration Engineering, 19-21 September 2016, Leuven, Belgium.

- T. Ampatzidis and D. Chronopoulos, *Parametric study of control of frequency banded behaviour of periodic pressurised composite structures*, 24th International Congress on Sound and Vibration, ICSV 2017, 2017, pp. 17 (peer reviewed).

and the journal publications are listed below:

- T. Ampatzidis and D. Chronopoulos, *Acoustic transmission properties of pressurised and pre-stressed composite structures*, Composite Structures, vol. 152, pp. 900-912, Sep. 2016.

- T. Ampatzidis, R. K. Leach, C. J. Tuck, and D. Chronopoulos, *Band gap behaviour of optimal one-dimensional composite structures with an additive manufactured stiffener*, Composites Part B: Engineering, vol. 153, pp. 26-35, Nov. 2018.

- T. Ampatzidis, D. Chronopoulos, *Mid-frequency band gap performance of sandwich composites with unconventional core geometries*, Composite Structures (Under review).

Part of the work here contributed in the following publication:

- D. Chronopoulos, I. Antoniadis, and T. Ampatzidis, *Enhanced acoustic insulation properties of composite metamaterials having embedded negative stiffness inclusions*, Extreme Mechanics Letters, vol. 12, 2016.

1.3 Thesis outline

The thesis is organised as follows: in Chapter 2 existing literature on topics related to this project is presented, which consist of acoustic and damping performance of composite periodic structures and banded behaviour of periodic sandwich and hybrid composite structures with additive manufacturing (AM) stiffener. In this way the existing approach of vibration isolation methods is presented and the gap in the literature is identified. In Chapter 3 the complete methodology used in this work is presented in detail,

which consists of mathematical equations, programming scripts and experimental setup design. Chapter 4 is the first section presenting the proposed innovative work, where the effect of pressure and pre-tension on damping and acoustic performance of composite monolithic and sandwich structure is presented. In this part of the work the initial form of the used tools is developed. Using these computational tools and developing more efficient versions of them in Chapter 5, the first study case of a stop band structure is examined comprising of sandwich formations which cannot be considered as structural element. The second case study of the chapter consists of load-bearing sandwich structures. Three unconventional core architectures are presented, with two of them implemented in load-bearing composite sandwich beams and validated against experimental results. Having applied the efficient tools, the potential of their implementation in a multi-disciplinary optimisation algorithm is presented in Chapter 6. This optimisation method examines the banded behaviour along with the structural performance of the case study. The algorithm is used to produce an optimal solution for a hybrid composite load-bearing structure with AM stiffener. Finally, in Chapter 7 the conclusions of the project are drawn, and future work is proposed.

Chapter 2: Literature review

2.1 Wave propagation calculation methods for composite structures

2.1.1 Analytical methods

Before the rapid evolution of the computing power, wave propagation and vibration analysis relied on analytical methods. This kind of methods can be found in classical publications [36, 37], where analytical formulas used to predict the wave propagation characteristics of numerous different structures are written in detail. Most of these methods could not be applied to composite structures due to the unique anisotropic mechanical characteristics of them. The barrier was the calculation of the stiffness matrix of a layered structure, since the different orientation and thickness of each layer demanded a method to determine its macroscopic behaviour, taking into account the contribution of all the constituents. This is where classical laminate plate theory (CLPT) [38] comes in the picture, a method which was developed as an extension of the Kirchhoff-Love's theory for isotropic panels and can be applied on thin orthotropic plates. When CLPT is formulated, there are some assumptions that need to be accepted a priori. These are listed below:

- Straight lines perpendicular to the midsurface remain straight after deformation.
- These lines, which are called transverse normals, do not elongate.
- The transverse normals rotate so that they remain perpendicular to the midsurface after the deformation.

In other words, the first two assumptions ensure the independence of the transverse displacement from the thickness of the plate and the transverse

normal strain, while the third assumption ensures zero transverse shear strains. Additionally, in order for the CLPT to be applied, the following assumptions and restrictions have to be covered:

- The layers of the laminate are perfectly bonded together (assumption).
- The material of each layer is linearly elastic and has three planes of material symmetry (restriction).
- Each layer is of uniform thickness (restriction).
- The strains and displacements are small (restriction).
- The transverse shear stresses on the top and bottom surfaces of the laminate are zero (restriction).

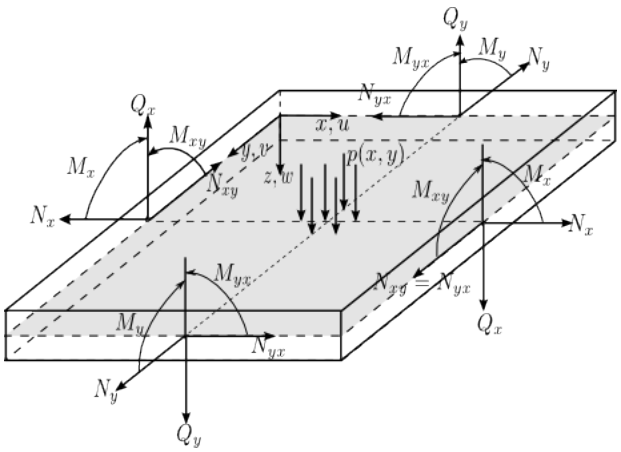


Figure 2.1: Force and moment resultants on a plate element.

The displacement field is formulated as follows:

$$\begin{aligned} u(x,y,z,t) &= u_0(x,y,t) - z\frac{\partial w_0}{\partial x}, \\ v(x,y,z,t) &= v_0(x,y,t) - z\frac{\partial w_0}{\partial y}, \\ w(x,y,z,t) &= w_0(x,y,t), \end{aligned} \tag{2.1}$$

where u_0, v_0 and w_0 are the displacements of the mid-plane of the plate and t is time. After the relevant calculations that are presented and explained

in detail in [38], the equations of motion of the plate are expressed as:

$$\begin{aligned} \delta u_0 : \frac{\partial N_{xx}}{\partial x} + \frac{\partial N_{xy}}{\partial y} &= \rho_s \frac{\partial^2 u_0}{\partial t^2}, \\ \delta v_0 : \frac{\partial N_{xy}}{\partial x} + \frac{\partial N_{yy}}{\partial y} &= \rho_s \frac{\partial^2 v_0}{\partial t^2}, \\ \delta w_0 : \frac{\partial^2 M_{xx}}{\partial x^2} + 2\frac{\partial^2 M_{xy}}{\partial x \partial y} + \frac{\partial^2 M_{yy}}{\partial y^2} &= \rho_s \frac{\partial^2 w_0}{\partial t^2}, \end{aligned} \tag{2.2}$$

where $\mathbf{N}$ and $\mathbf{M}$ are forces and moments respectively as shown in Fig. 2.1 and ρ_s is surface density. The expression of the forces and moments as a function of the panel's displacements needs to be introduced. This equation is the one that follows:

$$\begin{Bmatrix} \mathbf{N}_{xx} \\ \mathbf{N}_{yy} \\ \mathbf{N}_{xy} \end{Bmatrix} = \begin{bmatrix} \mathbf{A}_{11} & \mathbf{A}_{12} & \mathbf{A}_{16} \\ \mathbf{A}_{12} & \mathbf{A}_{22} & \mathbf{A}_{26} \\ \mathbf{A}_{16} & \mathbf{A}_{26} & \mathbf{A}_{66} \end{bmatrix} \begin{Bmatrix} \epsilon_{xx}^{(0)} \\ \epsilon_{yy}^{(0)} \\ \gamma_{xy}^{(0)} \end{Bmatrix} + \begin{bmatrix} \mathbf{B}_{11} & \mathbf{B}_{12} & \mathbf{B}_{16} \\ \mathbf{B}_{12} & \mathbf{B}_{22} & \mathbf{B}_{26} \\ \mathbf{B}_{16} & \mathbf{B}_{26} & \mathbf{B}_{66} \end{bmatrix} \begin{Bmatrix} \epsilon_{xx}^{(1)} \\ \epsilon_{yy}^{(1)} \\ \gamma_{xy}^{(!)} \end{Bmatrix} \tag{2.3}$$

and

$$\begin{Bmatrix} \mathbf{M}_{xx} \\ \mathbf{M}_{yy} \\ \mathbf{M}_{xy} \end{Bmatrix} = \begin{bmatrix} \mathbf{B}_{11} & \mathbf{B}_{12} & \mathbf{B}_{16} \\ \mathbf{B}_{12} & \mathbf{B}_{22} & \mathbf{B}_{26} \\ \mathbf{B}_{16} & \mathbf{B}_{26} & \mathbf{B}_{66} \end{bmatrix} \begin{Bmatrix} \epsilon_{xx}^{(0)} \\ \epsilon_{yy}^{(0)} \\ \gamma_{xy}^{(0)} \end{Bmatrix} + \begin{bmatrix} \mathbf{D}_{11} & \mathbf{D}_{12} & \mathbf{D}_{16} \\ \mathbf{D}_{12} & \mathbf{D}_{22} & \mathbf{D}_{26} \\ \mathbf{D}_{16} & \mathbf{D}_{26} & \mathbf{D}_{66} \end{bmatrix} \begin{Bmatrix} \epsilon_{xx}^{(1)} \\ \epsilon_{yy}^{(1)} \\ \gamma_{xy}^{(!)} \end{Bmatrix}, \tag{2.4}$$

where ϵ and γ are logarithmic and shear strain respectively, $\mathbf{A}_{ij}$ are called extensional stiffness matrices, $\mathbf{D}_{ij}$ bending stiffness matrices and $\mathbf{B}_{ij}$ bending-extensional coupling stiffness matrices. CLPT is an important method for vibration analysis as it offers a solution to the problem of the complicated calculation of the macroscopic behaviour of a composite structure.

CLPT's limitations start when high elastic modulus to shear modulus ratios are present. Additional and more advanced methods were needed to be developed to overcome these restrictions, with First-order shear deformation theory (FSDT) being one of them. FSDT [39] is based on the transverse shear deformation of the panel and can be used for the prediction of the dispersion characteristics at higher frequencies. The displacement field needs to be reformulated due to this new assumption and it is expressed as follows:

$$\begin{aligned} u(x, y, z, t) &= u_0(x, y, t) + z\phi_x(x, y, t), \\ v(x, y, z, t) &= v_0(x, y, t) + z\phi_y(x, y, t), \\ w(x, y, z, t) &= w_0(x, y, t), \end{aligned} \tag{2.5}$$

It can be seen now that FSDT has five degrees of freedom, with two of them being the ϕ_x and ϕ_y, which correspond to the rotations along x and y axis. After the relevant calculations the equations becomes

$$\begin{aligned}
\delta u_0 : \frac{\partial N_{xx}}{\partial x} + \frac{\partial N_{xy}}{\partial y} &= \rho_s \ddot{u}_0 + J_1 \ddot{\phi}_x, \\
\delta v_0 : \frac{\partial N_{xy}}{\partial x} + \frac{\partial N_{yy}}{\partial y} &= \rho_s \ddot{v}_0 + J_1 \ddot{\phi}_y, \\
\delta w_0 : \frac{\partial Q_x}{\partial x} + \frac{\partial Q_y}{\partial y} &= \rho_s \ddot{w}_0, \\
\delta \phi_x : \frac{\partial M_{xx}}{\partial x} + \frac{\partial M_{xy}}{\partial y} - Q_x &= J_1 \ddot{u}_0 + J_2 \ddot{\phi}_x, \\
\delta \phi_y : \frac{\partial M_{yy}}{\partial y} + \frac{\partial M_{xy}}{\partial x} - Q_y &= J_1 \ddot{u}_0 + J_2 \ddot{\phi}_y,
\end{aligned} \tag{2.6}$$

where J_1, J_2 the first and second moments of inertia respectively. These equations have similar solutions to CLPT, with the main difference being the order of the determinant, which in this case is fifth (5x5).

Many researchers have used this kind of classical theories producing satisfying outcomes, such as Leppington et al. [40, 41] who modelled the radiation efficiency and the vibroacoustic response under a reverberant field. Others [42, 43] have mathematically improved the existing equations and examined the vibrational behaviour of laminated plates. In the first work Alieldin et al. introduced a FSDT model to investigate the mechanical behaviour of the composite laminates and functionally graded plates where three different approaches were followed to produce a single layer functionally graded equivalent to the composite one. As for the second one, Thai et al. produced a simple FSDT with smaller number of unknowns than the original one. Kurtze and Waters [44] were the first to examine the wave dispersion of thick sandwich structures by developing a model where the core was treated as incompressible, which kept them from modelling the deformation of the panel in the thickness sense. Dym and Lang [45], using the kinematic assumptions of [46] developed a structural model for an infinite sandwich panel deriving the five equations of motion corresponding to the symmetric and antisymmetric motion of the panel. Sokolinsky et al. [47] developed a consistent higher-order shear deformation theory (HSDT) taking into account the core's shear deformation.

A method to calculate vibroacoustic response of periodic structures is the transfer matrix (TM) method. $\mathbf{T}$, as the TM is usually written, is a function of excitation frequency, ω, and is commonly used to relate the force and displacement on the input to the output of the structure. The starting point of this analysis is the definition of the TM, which is $\mathbf{T}_{(\omega)} = \mathbf{K} - \omega^2\mathbf{M}$. This leads to the following equation:

$$\begin{bmatrix} \mathbf{F}_{\mathrm{O}} \\ \mathbf{U}_{\mathrm{O}} \end{bmatrix} = \mathbf{T}_{(\omega)} \begin{bmatrix} \mathbf{F}_{\mathrm{I}} \\ \mathbf{U}_{\mathrm{I}} \end{bmatrix}, \tag{2.7}$$

where $\mathbf{F}$ and $\mathbf{U}$ are the force and displacement matrix, and $\mathbf{T}$ is the TM, and the subscripts O and I stand for output and input respectively. Using Bloch wave boundary conditions and after the necessary calculations the TM method gives the eigenvalue problem:

$$[\mathbf{T}_{(\omega)} - \lambda\mathbf{I}] \begin{bmatrix} \mathbf{F}_I \\ \mathbf{U}_I \end{bmatrix} = \mathbf{0}, \tag{2.8}$$

where $\mathbf{I}$ is the identity matrix. This eigenvalue problem is easily solved by inputting the ω values to get λ. TM method is quite similar to the finite element (FE) method described later with the main difference being that TM is not limited to using FE and can be used with other formulations and analytical solutions, like in [48].

Researchers needed to develop a way to examine high frequency vibroacoustic in a more reliable and effective way. Wang et al. [49, 50] used FSDT to construct a structural model of an infinitely long sandwich panel in which the vibroacoustic response within a statistical energy analysis (SEA) context was calculated. SEA is a statistical method developed to examine the wave propagation in mid- and high frequencies, as it can be seen in Fig. 2.2. The SEA development started in 1960s when engineers needed a method to predict the vibroacoustic behaviour of large structures, a need which essentially coincides with the rapid developments in the airspace industry [51]. SEA is also a statistical method, as it is implied by its name, and its main advantage is that it can take into account large numbers of resonant modes to calculate the vibroacoustic response. The deterministic methods

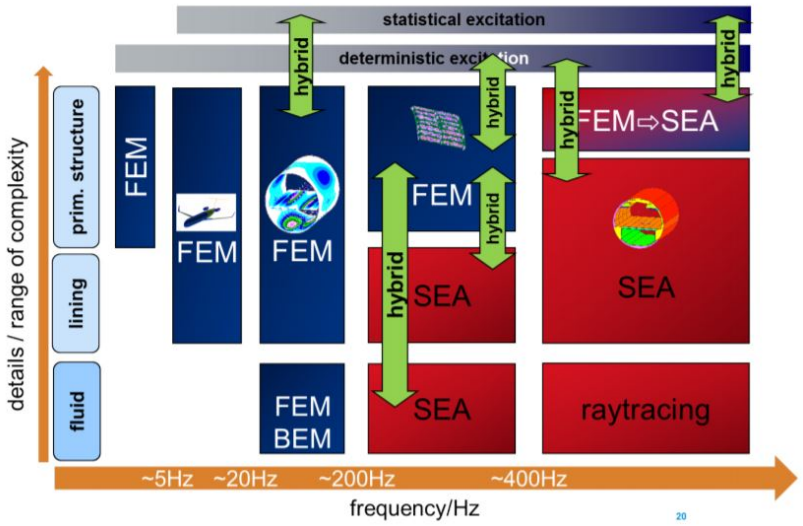


Figure 2.2: SEA and FEM analysis strategy in aerospace research area [3].

rely on the first low-frequency modes, so having the capacity of large number of modes is the reason why SEA is preferred for mid- to high frequency studies. SEA's equations used in this investigation are described in Sec. 3.2.

2.1.2 Finite Element(s) methods

As computational power increased and computational time significantly decreased, efficient numerical methods started to gain ground in vibroacoustic analysis. Wave propagation has been an object of intense research with numerous numerical methods being developed during the last decades. Finnveden [52] examined hollow beam structures and presented a method of calculating the modal density and group velocity using as input the wave propagation characteristics of the examined thin-walled schemes. In [53], the authors used spectral finite element (SFE) method to predict the wave propagation characteristics, overcoming the thresholds of CLPT in high frequencies. More specifically, CLPT fails to predict the generation of new structural waves as frequency gets higher, while SFE method can and offers a more precise wave dispersion analysis at higher frequencies. In [54] the phase constant surfaces of periodic composite and stiffened structures were

examined taking advantage of the periodicity using PST and FE. In that work, an expression for the computation of the radiation efficiency was presented and the sound transmission loss (STL) was expressed through the radiation and mechanical impedances of the structures. In [55] and [56], the authors used a multi-layer analytical model based on Mindlin theory to calculate the dispersion characteristics of layered structures. In this work, though, the symmetric mode of motion was not naturally expressed. The same authors [57] came back presenting an approach for taking into account the symmetric wave motion for thick panels.

Another quite useful and efficient method of examining wave propagation is the Wave Finite Element Method (WFEM), firstly introduced in [58] by Mead. Its main aspect is that it takes advantage of the periodicity of the structure and using existing classical literature's PST equations [37] managed to examine a structure's wave propagation by modelling only a small periodic part of it using FE for its analysis. In this way the calculation of the wavenumbers and eigenvectors was achieved with considerably lower cost of time than in other methods. Therefore, having acquired the wavenumbers, a complete examination of the vibroacoustic behaviour of a periodic structure can be done. Following the principles of a conventional

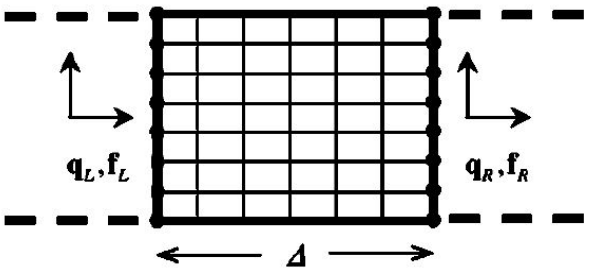


Figure 2.3: Finite elements mesh of 1D waveguide. [4]

FE analysis, the equation of the motion of the section (Fig. 2.3) is

$$\left[\mathbf{K} - \omega^2 \mathbf{M}\right] \mathbf{q} = \mathbf{f}, \tag{2.9}$$

where $\mathbf{K}$ and $\mathbf{M}$ are the stiffness and mass matrices respectively, $\mathbf{f}$ is the vector of the nodal forces and $\mathbf{q}$ the vector of the nodal degrees of freedom

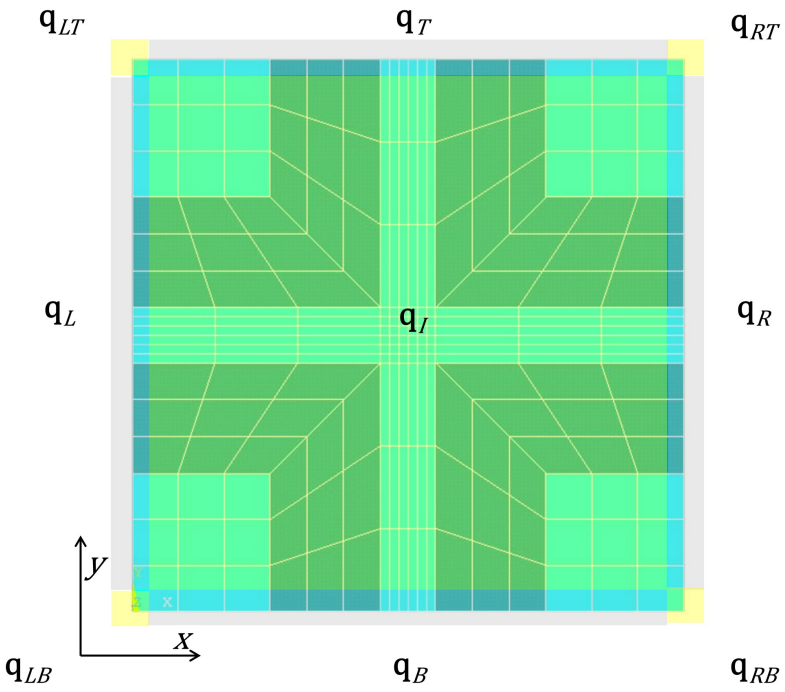


Figure 2.4: DOFs of two-dimensional model of periodic structure.

(DOFs). Damping can also be included in the analysis either with $\mathbf{K}$ being complex or as a viscous damping matrix $\mathbf{C}$.

According to Floquet's theorem, the equations that relate the displacements on the edges to the ones on the sides of the modelled unit cell are the following [58]:

$$\begin{aligned} \mathbf{q}_R &= \mathrm{e}^{-\mathrm{i}\varepsilon_x}\mathbf{q}_L, \qquad \mathbf{q}_T = \mathrm{e}^{-\mathrm{i}\varepsilon_y}\mathbf{q}_B, \\ \mathbf{q}_{RB} &= \mathrm{e}^{-\mathrm{i}\varepsilon_x}\mathbf{q}_{RL}, \quad \mathbf{q}_{LT} = \mathrm{e}^{-\mathrm{i}\varepsilon_y}\mathbf{q}_{LB}, \quad \mathbf{q}_{RT} = \mathrm{e}^{-\mathrm{i}\varepsilon_x-\mathrm{i}\varepsilon_y}\mathbf{q}_{LB}, \end{aligned} \tag{2.10}$$

where the terms $\varepsilon_x = k_x L_x$ and $\varepsilon_y = k_y L_y$ are referred to as "phase constants", B and T stands for bottom and top (see Fig. 2.4), L_x, L_y are the periodic element's length in the x and y directions and k_x, k_y are the wavenumbers. The complete vector of the local DOFs can be ordered as followed

$$\mathbf{q} = \begin{bmatrix} \mathbf{q}_I^T & \mathbf{q}_B^T & \mathbf{q}_T^T & \mathbf{q}_L^T & \mathbf{q}_R^T & \mathbf{q}_{LB}^T & \mathbf{q}_{LT}^T & \mathbf{q}_{RT}^T \end{bmatrix}^T. \tag{2.11}$$

In order to write the propagation relation in Eq. (2.10) in matrix form, the transform matrix $\mathbf{R}$ is considered, which is given by the following equation

[54]:

$$\mathbf{q} = \begin{bmatrix} \mathbf{I} & \mathbf{0} & \mathbf{0} & \mathbf{0} \\ \mathbf{0} & \mathbf{I} & \mathbf{0} & \mathbf{0} \\ \mathbf{0} & \mathbf{I}e^{-i\varepsilon_y} & \mathbf{0} & \mathbf{0} \\ \mathbf{0} & \mathbf{0} & \mathbf{I} & \mathbf{0} \\ \mathbf{0} & \mathbf{0} & \mathbf{I}e^{-i\varepsilon_x} & \mathbf{0} \\ \mathbf{0} & \mathbf{0} & \mathbf{0} & \mathbf{I} \\ \mathbf{0} & \mathbf{0} & \mathbf{0} & \mathbf{I}e^{-i\varepsilon_x} \\ \mathbf{0} & \mathbf{0} & \mathbf{0} & \mathbf{I}e^{-i\varepsilon_y} \\ \mathbf{0} & \mathbf{0} & \mathbf{0} & \mathbf{I}e^{-i\varepsilon_x - i\varepsilon_y} \end{bmatrix} \mathbf{x} = \mathbf{R}\mathbf{x}, \tag{2.12}$$

where $\mathbf{I}$ is the unit matrix. In this way, the equation becomes

$$\mathbf{q} = \mathbf{R}\mathbf{q}', \tag{2.13}$$

where

$$\mathbf{q}' = \mathbf{x} = \begin{bmatrix} \mathbf{q}_I & \mathbf{q}_B & \mathbf{q}_L & \mathbf{q}_{LB} \end{bmatrix}^T. \tag{2.14}$$

The equations for the one-dimensional case including damping are shown in Sec. 3.1.

In search for more efficient methods, Mace et al. [4] developed a condensation method for the WFEM. The dynamic stiffness matrix $\mathbf{D} = \mathbf{K} - \omega^2\mathbf{M}$ is partitioned as in equation 2.15 in order to reflect the influence of internal, left and right nodes on the wave propagation (no external forces are acting on the interior nodes):

$$\begin{bmatrix} \tilde{\mathbf{D}}_{II} & \tilde{\mathbf{D}}_{IL} & \tilde{\mathbf{D}}_{IR} \\ \tilde{\mathbf{D}}_{LI} & \tilde{\mathbf{D}}_{LL} & \tilde{\mathbf{D}}_{LR} \\ \tilde{\mathbf{D}}_{RI} & \tilde{\mathbf{D}}_{RL} & \tilde{\mathbf{D}}_{RR} \end{bmatrix} \begin{Bmatrix} \mathbf{q}_I \\ \mathbf{q}_L \\ \mathbf{q}_R \end{Bmatrix} = \begin{Bmatrix} \mathbf{0} \\ \mathbf{f}_L \\ \mathbf{f}_R \end{Bmatrix}. \tag{2.15}$$

After the condensation, equation 2.15 can be written as

$$\begin{bmatrix} \mathbf{D}_{LL} & \mathbf{D}_{LR} \\ \mathbf{D}_{RL} & \mathbf{D}_{RR} \end{bmatrix} \begin{Bmatrix} \mathbf{q}_L \\ \mathbf{q}_R \end{Bmatrix} = \begin{Bmatrix} \mathbf{f}_L \\ \mathbf{f}_R \end{Bmatrix}, \tag{2.16}$$

where

$$\begin{aligned} \mathbf{D}_{LL} &= \tilde{\mathbf{D}}_{LL} - \tilde{\mathbf{D}}_{LI}\tilde{\mathbf{D}}_{II}^{-1}\tilde{\mathbf{D}}_{IL}, \quad \mathbf{D}_{LR} = \tilde{\mathbf{D}}_{LR} - \tilde{\mathbf{D}}_{LI}\tilde{\mathbf{D}}_{II}^{-1}\tilde{\mathbf{D}}_{IR}, \\ \mathbf{D}_{RL} &= \tilde{\mathbf{D}}_{RL} - \tilde{\mathbf{D}}_{RI}\tilde{\mathbf{D}}_{II}^{-1}\tilde{\mathbf{D}}_{IL}, \quad \mathbf{D}_{RR} = \tilde{\mathbf{D}}_{RR} - \tilde{\mathbf{D}}_{RI}\tilde{\mathbf{D}}_{II}^{-1}\tilde{\mathbf{D}}_{IR}. \end{aligned} \tag{2.17}$$

Using a slightly different form of Floquet's theorem, the equation that relates the displacements on the two edges of the section is [5]:

$$\mathbf{q}_R = \lambda \mathbf{q}_L, \quad \mathbf{f}_R = -\lambda \mathbf{f}_L, \tag{2.18}$$

where $\lambda = e^{-ikL_x}$, with k being the wavenumber. Equation 2.16 is rearranged:

$$\lambda \begin{Bmatrix} \mathbf{q}_L \\ \mathbf{f}_L \end{Bmatrix} = \mathbf{T} \begin{Bmatrix} \mathbf{q}_L \\ \mathbf{f}_L \end{Bmatrix}, \tag{2.19}$$

where

$$\mathbf{T} = \begin{bmatrix} -\mathbf{D}_{LR}^{-1}\mathbf{D}_{LL} & \mathbf{D}_{LR}^{-1} \\ -\mathbf{D}_{RL} + \mathbf{D}_{RR}\mathbf{D}_{LR}^{-1}\mathbf{D}_{LL} & -\mathbf{D}_{RR}\mathbf{D}_{LR}^{-1} \end{bmatrix} \tag{2.20}$$

is the TM. The transfer matrix $\mathbf{T}$ depends only on the dynamic stiffness of the section. In [4, 59] the eigenvalues of $\mathbf{T}$ were calculated and the wave propagation curves were derived. The two-dimensional equations are shown in Sec. 3.1.1.

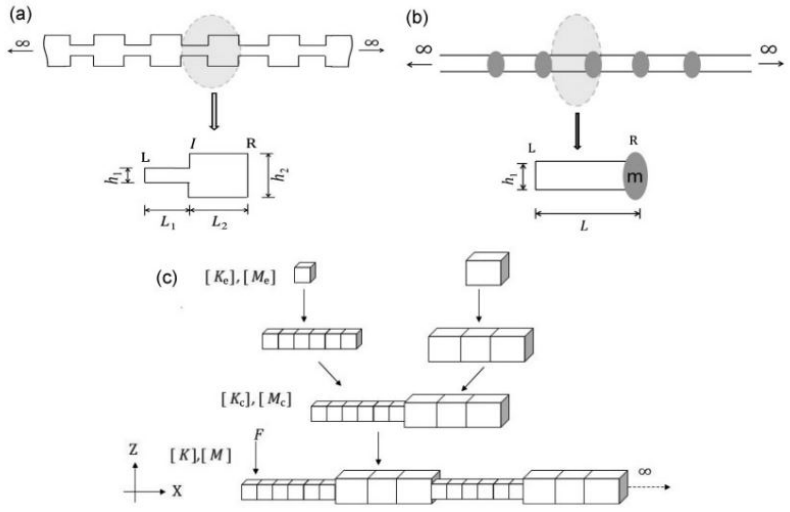


Figure 2.5: Schematic representation of the examined beams in [5]. The procedure of building the unit cell model is depicted.

WFEM has been found quite useful by researchers as it is presented in the following sentences, since, as mentioned above, it allows to examine the vibroacoustic behaviour of a periodic structure by analysing only a small part of it. Besides its use for periodic structures, which can be found in existing literature in engineering applications (airplane's fuselage, space rockets, ship

etc.), the method can also be applied for the examination of different materials' acoustic behaviour. Mead used WFEM in several applications and theoretical examinations of wave propagation, the majority of which were summarised in [60]. WFEM has also been used recently in one-dimension [5] and two-dimension analyses [61] offering a quick and reliable method to examine wave propagation. Using FE for the structure's modelling has given researchers the ability to broaden the potentials of the method, calculating loss factors [62] with the help of existing theories like the modal energy strain method [63]. In addition to that, Manconi et al. [64] calculated the effect of the pre-stress on the loss factor and wavenumbers of structures using two dimensional WFEM. Chronopoulos et al. [65] used wave dispersion results of WFEM to calculate a dynamic stiffness matrix for a honeycomb orthotropic sandwich panel, the results of which were validated experimentally. Additionally, the same authors in [66] and [67] using WFEM and SEA computed the broadband vibroacoustic response of composite shells and thick layered panels. Another use of WFEM is the examination of the potential band gaps in periodic structures, as described in detail in the next section. Domadiya et al. [5] used WFEM to model two different periodic beams to examine the band gaps and had their results validated against actual experiments. Additional work on band gaps is described in Sec. 2.3. Since the development of the method, researchers have also focused on the improvement of the mathematical tools that are used to acquire the wave dispersion curves. Droz et al. [68] proposed a mathematically improved version of the WFEM and calculated the wave propagation and band gaps in a periodically stiffened plate, while Waki et al. [69] examined numerical issues of the method.

2.2 Damping enhancement methods

Composite structures offer high stiffness to weight ratios which makes them ideal choice for lightweight structures, but not for their vibroacoustic performance. Nevertheless, they exhibit superior damping behaviour compared

to metals, due to their various energy dissipation sources: viscoelastic nature of the matrix, interphase damping mechanism, damping due to damage (matrix cracks, fibres broken etc.), viscoplastic damping and thermoplastic damping [70]. Another advantage is that they can offer far more design versatility as damping capacity, along with other specific properties, can be tailored to meet specific structural requirements [71, 72]. Jaber et al. [73] exploited this property and examined the vibrational energy flow in carbon fibre composite structures. More specifically, a car roof was examined with different material case studies: steel and different carbon fibre layups. It was shown that the damping performance, and hence the vibrational energy flow, was affected by the layup of the composite structure and the boundary conditions.

If this is not enough, though, additional measures have to be taken to reach the required damping levels. As mentioned in Chapter 1, one of the major methods to do this, is the use of damping layers. Some of the areas of applications of damping layers on metallic structures are in the aerospace [74] and automotive industry [75] where research focuses on the effective minimal application of the layer [76]. Assarar et al. [77] examined the potential of using the damping layer as interleaf into the carbon fibre laminates. The laminates that were produced demonstrated improved damping performance with high variability depending on frequency. In [78], Duvigneau et al. examined the solution of granular materials as damping enhancement. More specifically, the damping behaviour of sand caused by collisions and frictions between the individual particles was examined as a noise reduction treatment on an internal combustion engine's oil pan. The original oil pan was modified so that sand could be added in a floor compartment and the new solution was tested in vibrations using both electrodynamic shaker and impact hammer. The results were compared with the original oil pan design, and they showed promising vibration damping behaviour between 500-2000 Hz. It was stated that the damping might be enhanced with design optimisation of the lower compartment, which was kept flat for the experiment purposes.

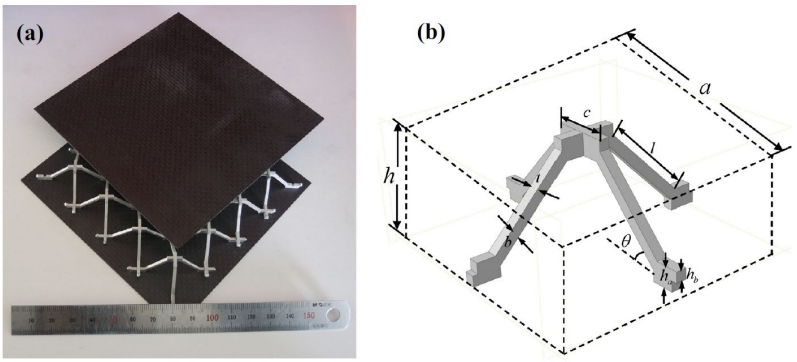


Figure 2.6: Hybrid composite pyramidal truss sandwich panel (and its unit cell) examined in [6], presenting enhanced damping capacity.

Researchers have been also looking for innovative ways of enhancing damping. In [79], Syam et al. shifted the eigenfrequency of a structure using strut-based lattice formations. The design was manufactured using the AM method and was tested to prove that shifting the eigenfrequency is a method to avoid vibrations. Nevertheless, the design had a negative effect in the static integrity of the structure. In [18], Salari-Sharif et al. presented a novel damping mechanism exhibited by 3D woven lattice materials. In this work the writers focused on the high-frequency excitations, examining a 3D woven lattice which offered structural stiffness along with enhanced damping performance in the high-frequency range. The material presented demonstrated impressive behaviour in the high-frequency range, where damping was enhanced in large level, where traditional damping materials offer low damping capacity as frequency gets higher. Additionally, a significant disadvantage of the specific material was the challenging manufacturing method and the complex geometry which made manufacturing quite cumbersome. In [6, 80, 81], Yang et al. developed hybrid composite pyramidal truss sandwich panels and examined their performance using multiple damping configurations (see Fig. 2.6). Both theoretical and experimental examinations were completed with the development of numerical models helping with the first part. It was proven that the specific structure offers increased damping performance with the potential of providing stiffness to the assembly.

All the above solutions were proved to enhance the damping of the struc-

ture but with added complexity or cost, whether this is actual manufacturing cost or additional mass.

2.3 Periodic structures and band gap engineering

As mentioned above, periodic formations can be found in numerous structures, such as airplanes fuselage, train, buildings etc. Hence engineers started quite early to examine the possibility to take advantage of the periodicity and develop efficient methods to examine the vibroacoustic performance of them. The first work done on a one-dimensional lattice was that of Newton [82], where a formula for the velocity of the sound was sought. Therefore a simple lattice consisting of equal masses spaced equally along the direction of propagation was used to represent homogenous material, as depicted in Fig. 2.7. In this way, Newton assumed that the masses were the particles of a continuous medium and the springs were their bonds, since there was gap in knowledge of the continuous body mechanics and partial differential equations at that time in history. Mathematical tools continued to be the main issue research focused on in 18^{th} and 19^{th} centuries, with scientists like John Bernoulli and his son Daniel, Taylor and Euler working on offering solutions to them. In the 19^{th} century, one of the most important studies was Floquet's mathematical work [83], in which the one-dimensional Mathieu's equations were studied as part of the theory of differential equations with periodic coefficients. Floquet's work was followed by that of Rayleigh [84], who developed a similar form to Floquet's theorem, which transforms the periodic system to a linear system with constant, real coefficients. As periodic structures examination got deeper, it was discovered and demonstrated that judiciously designed periodic structures can enhance the vibration attenuation through the mechanisms of band gaps. In the 20^{th} century, Leon Brillouin examined thoroughly in his book [37] the band gap of elastic waves, providing explanations of mathematical and practical importance, where PST was first introduced. Some years later

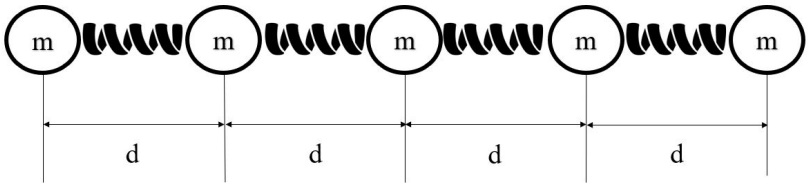


Figure 2.7: One-dimensional periodic model examined by Newton representing the mechanics of the particles of a continuous body.

Mead [60, 85, 86] introduced the WFEM which is based on PST, as mentioned before. Thanks to these methods, along with the vast improvement of computer capacity over the last decades, researchers have nowadays the ability to predict the vibroacoustic and dynamic performance of several applications in relatively short times. This enabled the increase of the number of researcher examining the application of banded structures.

In Sec. 1, I referred to band gap categories according to the generating mechanism. In this paragraph, though, the relevant categories according to the application are presented. There are two major kinds of band gaps: the *photonic* band gaps which refers to electromagnetic application and their frequency band lies on that of the light waves, and the *phononic* band gaps which refers to the mechanical application and their frequency band lies in the acoustic frequencies. Structures and mechanisms that demonstrate photonic band gaps, usually called photonic crystals, are used in controlling the propagation of light waves. This characteristic of theirs is of utmost importance in fields such as optics and laser technology, and this is why extensive research is focusing on their development. Most of the research described in this thesis is on phononic band gaps, which is the topic of the presented investigation. In addition to the aforementioned categories another kind of gap has been introduced, the *phoxonic* band gap, which is the simultaneous existence of photonic and phononic band gaps, a characteristic that has lots of potentials in vibration absorption. This kind of structures have been studied in [87, 88, 89, 90].

In the following paragraphs, more examples of phononic band gap works

are added to the ones presented in Sec. 1, along with some representative examples of research on photonic band gaps. In [91], Khelif et al. exam-

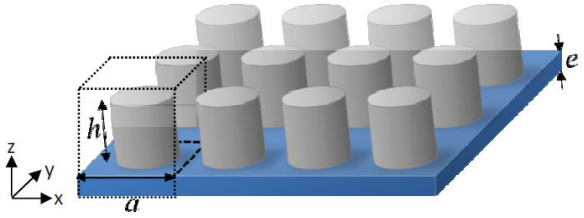


Figure 2.8: A schematic representation of a phononic crystal, made of a square lattice of finite cylinders deposited on a homogeneous plate. All the dimensions are less than 1 mm. [7]

ined the potentials of the two-dimensional phononic crystal with tuneable banded behaviour, while in [92] the same author studied the effect of localised defect modes in a full acoustic band gap in a two-dimensional lattice of steel cylinders immersed in water. A snowflake-like structure was examined, and the authors highlighted its potential application in developing planar circuits for interacting optical and acoustic waves. In [93], both theoretical and experimental studies of guiding and bending acoustic waves in highly confined waveguides forms were presented. Moreover, a binary two-dimensional phononic crystal constituted by a square array of circular parallel steel cylinders in water was examined. In [94] and [95], Benchabane et al. and Khelif et al., respectively, examined phononic crystals which exhibited elastic band gaps. In the latter work a parametric analysis was also completed examining the influence of the physical characteristics of the crystal on the banded behaviour. In [96], Bresco et al. designed, fabricated and measured a one-dimensional optomechanical crystal exhibiting both photonic and phononic band gap in high frequency. This kind of structures can be used in the field of cavity optomechanics which focuses on the interaction between electromagnetic radiation and mechanical vibrations of matter. In [97], square and hexagonal (honeycomb) lattice phononic crystals were shown to produce band gaps, while in [98] a square-lattice phononic crystal slab consisting of a single layer of spherical steel beads in a solid epoxy ma-

trix was studied, focusing on the propagation of the acoustic waves through it. In [99] experimental measurements of acoustic transmission through a solid-solid two-dimensional binary composite media were completed, while the same researchers examined in [100] the propagation of acoustic waves in two different types of two-dimensional composite medium. In [7] the theoretical study of the band structure of a phononic crystal (Fig. 2.8) consisting of a periodic array of cylindrical dots deposited on a thin plate of a homogeneous material was presented. In [101], the tuneability of two-dimensional square lattice sonic crystals was examined so that the potential of controlling the band gaps was studied.

Several review reports have been produced on the banded structures research. Troia et al. [102] reported the latest technology on photonic crystals with applications in healthcare, defence and security to name a few. In [103], Pennec et al. recorded and analysed the existing research on two-dimensional phononic crystals up until the year the report was written. A comprehensive report was also produced by Hussein et al. [22] on phononic materials and structures recording their historic origins and the research and applications of them. Lu et al. [104] wrote a short report on phononic crystals and acoustic metamaterials, where a short description of the history of the research on metamaterials was presented. In [105] Armenise et al. reported in short existing modelling methods and applications of photonic and phononic band gap structures. Ma et al. [106] produced a comprehensive report on the latest technology of the acoustic metamaterials and their applications.

In this thesis, the focus is limited to low and mid-frequency phononic band gaps demonstrated mostly by load-bearing structures. As part of the work presented in this thesis takes advantage of the geometrical liberty provided by AM technology, it seems proper to write some words on the use of AM in band gap research. In the next section the importance and wide use of this technology in banded structures research is described.

2.4 Band gap and additive manufacturing

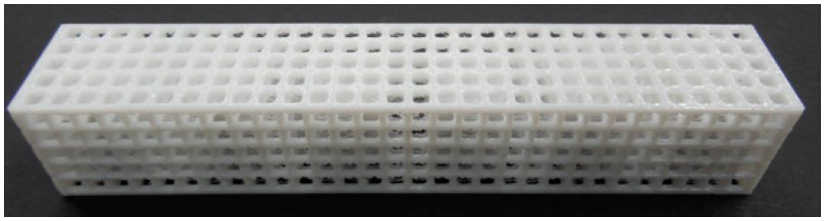


Figure 2.9: 3D printed band gap structure as examined in [8].

Structures that exhibit band gap behaviour tend to be of significantly complex geometry and cannot be realised using conventional manufacturing techniques. Therefore, AM technologies attract an increasing number of researchers. AM eliminates several design limitations and is currently in extensive use in research and industry for small-scale production with a wide variety of manufacturing operations. AM researchers take advantage of the freedom in design that can be attained with relatively low cost by avoiding the manufacturing cost of additional tools. Matlack et al. [8] (see Fig. 2.9) examined the broadband vibration absorption of AM metastructures exhibiting local resonance, while Qureshi et al. [107] modelled and manufactured a cantilever-in-mass metamaterial to achieve wave attenuation. Claeys et al. [108] examined, both numerically and experimentally, several versions of a vibroacoustic metamaterial with local resonances and compared the two sets of results, while Warmuth et al. [109] used AM methods to manufacture a 3D single phase phononic band gap material with cellular design exhibiting a wide stop band at high frequencies. Bilal et al. [110] experimentally observed the trampoline phenomenon on the band gap behaviour of AM metamaterial plates. The trampoline phenomenon is observed when the effective stiffness of the plate supporting the pillars of the metamaterial is reduced and the effect of it is broadening the band gap. The wide variety of designs that can be produced using AM methods has led to the opportunity for researchers to examine 3D band gaps in complex structures [9, 111]. This wide use of AM led researchers to examine the effect of the property variability of AM on the experimental

results [112, 113], where a better agreement was obtained between analysis and experimental results by considering uncertainties in the resonators and the host structure. In [114] and [115], Jensen and Kook focused on the band gaps of coupled acoustical-mechanical systems, producing experimental results using 3D printing to evaluate their analytical models. Reynolds et al. [116] also used 3D printing to reproduce and validate their simulation model. The specimen consisted of an acoustic metamaterial with hollow spheres which act as local resonators.

2.5 Band gap optimisation



(a) Shape variables (b) Design (c) Repeated

Figure 2.10: A representative result of the phononic band gap optimization is shown as examined in [9].

Having developed efficient tools to examine the banded behaviour of the structures and having great design freedom thanks to AM technology, as seen in the previous section, researchers applied optimisation schemes on their band gap designs. Efficient and accurate optimisation schemes are essential when determining design solutions and researchers use several methods. The optimal design of an Euler-Bernoulli simple band gap beam, made of linearly elastic material, has been recently examined [117], where the author used a bound optimisation method which optimised the gap between natural frequencies. Hussein et al. [23, 118, 119] optimised the band gap behaviour of periodic layered structures, where methods to achieve band gap behaviour within specific frequencies were developed. More specifically, Hussein et al. employed a multi-objective genetic algorithm that generates

a population of possible solutions and searches for the optimum one. This method was tailored so that several objectives were examined, such as the percentage of the band gaps in specific frequencies, low frequency band gaps and control of the speed of energy propagation in the structure. Jensen and Sigmund [120] optimised the band gap behaviour of phononic structures using topology methods. Langley et al. [121] used a quasi-Newton algorithm with 30 random-start runs to obtain the optimal vibration absorption of the structure, while Wormser et al. [9] optimised the phononic band gap behaviour of cellular structure using gradient based methods. To the authors' knowledge and by the time this thesis is written, all the optimisation methods for phononic band gap behaviour focus solely on tailoring the band gap.

2.6 Sandwich structures

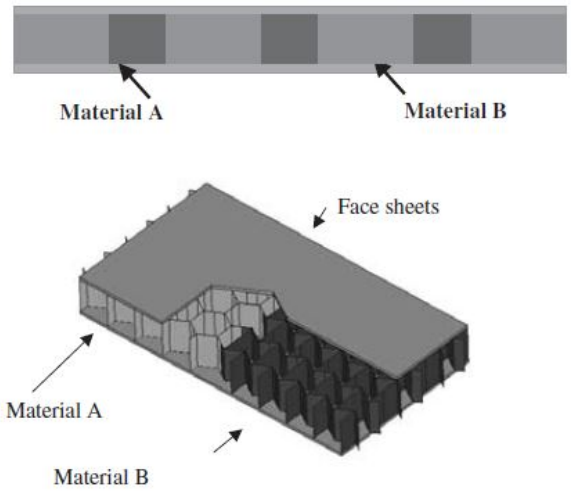


Figure 2.11: Sandwich beam with periodic honeycomb core and unit cell, as examined in [10].

Significant part of this research consists of sandwich structures where band gap schemes are examined, including both structural and non-structural solutions. Hence, it seems proper to dedicate a section of this thesis' literature review on sandwich structures and band gaps. A sandwich structure

is formed when two thin facings or skins are bonded on a lighter core that is used to keep them together and apart. This formation offers increased bending and torsional stiffness with minimal added mass as lightweight core materials are used in most of these cases (e.g. aluminium or aramid honeycomb, balsa wood or foam) [122]. The first application of lightweight structural sandwich parts was first seen in aircrafts in the 1940s since they reduced the weight and increased the payload and flight distance [123]. Since then sandwich structures have been a major part of load bearing structures and applications can be found in many industries such as civil transportation [124, 125, 126] and architecture [127]. Nowadays research has focused on examining the static behaviour of innovative solutions of sandwich formations, like a cylinder with orthogonal corrugated trusses [128], with orthogonal grids [129] or with beams with rapid prototyping cylinders as core [130]. Research also focused on corrugated cores [131, 132, 133].

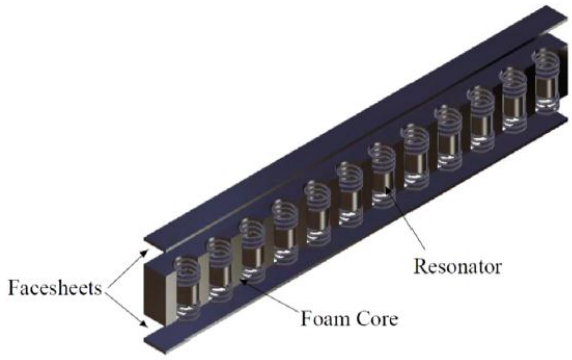


Figure 2.12: Graphic representation of a sandwich beam with internal resonators [11].

Taking advantage of the band gap mechanisms, researchers examined the possibility of having sandwich structures exhibiting stop bands. Ruzzene et al. [10, 134] (see Fig. 2.11) examined theoretically the behaviour and control of sandwich beams and plates with auxetic core. It has been proven that photonic band gaps could be attained with a periodic lattice core [135] and in [136, 137] high-frequency band gaps were exhibited by sandwich phononic crystal plates. Local resonance mechanisms have also been ex-

amined as band gap generators in sandwich structures [11] (Fig. 2.12), where Sharma et al. focused on the interaction and control of the band gap and how to tune the characteristics to achieve specific stop bands. In [138] Jiang et al. examined theoretically and experimentally a phononic crystal of periodic circular cavity sandwich plates attaining low-frequency stop bands, and in [139] Badran et al. developed a lighter model to simulate the dynamic behaviour of sandwich structures. Guo et al. [140] examined theoretically the banded behaviour of a sandwich structure using two periodically alternating viscoelastic materials as core achieving low-frequency stop bands. Also, the effect of damping on the band gap was examined and in [141] Sheng et al. manufactured the same structure to examine it experimentally. In [142, 143] the effect of the banded behaviour of a sandwich plate with locally resonant structure on the transmission of the sound was examined proving that a band gap offers significantly enhanced sound transmission loss. A thorough review of the current research on sandwich structures was produced by Birman and Kardomatea [144].

For all the aformentioned cases the band gap is achieved with a cost in complexity or additional mass.

2.7 Conclusion

In this chapter a brief overview of the existing literature on research methodologies of wave propagation of periodic structures and band gap engineering is provided. The presented work covers several areas of research so this chapter includes representative examples of studies on the specific areas. First, some of the existing mathematical tools and how researchers developed these methods are presented. Then recent work on damping methods is described, with some studies on the properties of composite materials and others on innovative methods of damping enhancement. After that, the state of the art in the periodic structures and band gap engineering is described, which is the main part of this work. The next part focuses on band gap engineering and how AM technology boosted the limits of engi-

neers in periodic structures. Additionally, several examples of band gap optimisation studies are presented. Finally, a brief account of research on sandwich structures with banded behaviour is developed.

During this literature examination, it was noticed that no work has been completed on band gap schemes able to be part of load-bearing structures. Furthermore, the majority of the designs that are produced are of complex geometry, which makes the industrialisation of the designs quite costly. In addition to this, it is only in the last years that researchers validate the theoretical calculations of the band gap phenomena with experimental results, an area that AM technology has helped a lot to develop. Hence the main focus of this work is to develop a multi-disciplinary optimisation algorithm which produces the optimal solution concerning band gap and static stiffness performance and which is also easy-to-manufacture. Additionally, developing an experimental setup and validating the vibroacoustic performance is also an essential part of this work.

Chapter 3: Methodology

In this chapter the methodology that is used during this work is presented in detail. The first part presents the PST and the equations that calculate the wave dispersion curves along with the loss factor. Then the SEA model and how the energy analysis quantities are derived is shown. After that the structure of the MATLAB script produced in this research is presented, followed by the optimisation scheme. Finally, the experimental method for measuring vibrations is described.

3.1 Periodic structure theory

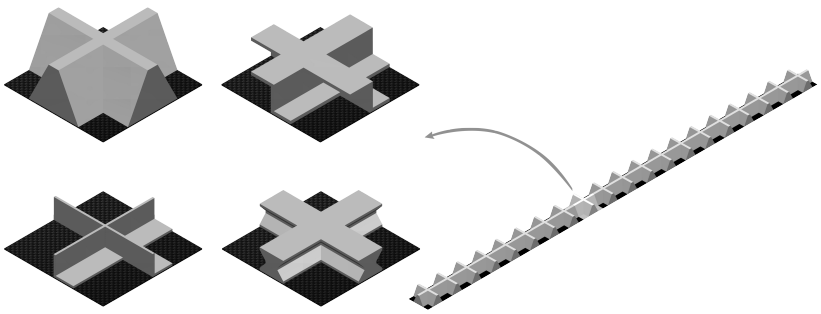


Figure 3.1: Several schemes of periodic structures.

The PST used in this work is presented in detail elsewhere [54]. A generic structure with 1D periodicity is considered. A unit cell is extracted from the structure (see Fig. 3.1) and its behaviour modelled with the FE method. A steady-state free harmonic vibration of frequency ω is considered in what follows and all response quantities are represented by complex amplitudes, so that

$$\mathbf{q}(t) = \mathbf{q}\mathrm{e}^{\mathrm{i}\omega t}, \tag{3.1}$$

where t is time and the degrees of freedom $\mathbf{q}$ can be partitioned into interior (I), left (L) and right (R) (see Fig. 3.2). According to Floquet's theorem, the equation that relates the displacements on the sides of the modelled

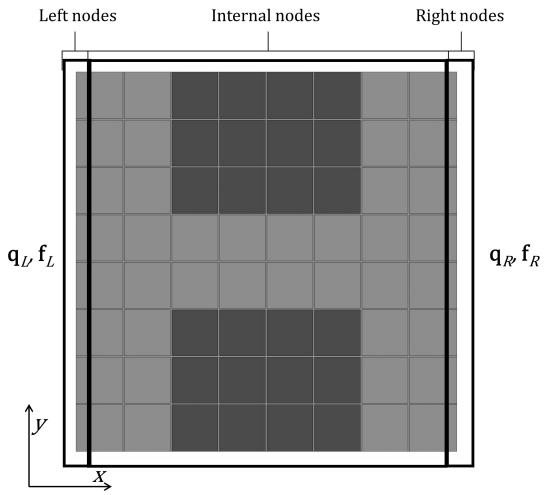


Figure 3.2: The employed FE model for investigation of 1D wave propagation.

unit cell is the following [58]:

$$\mathbf{q}_R = \mathrm{e}^{-\mathrm{i}\varepsilon_x}\mathbf{q}_L, \tag{3.2}$$

where the term $\varepsilon_x = k_x L_x$ is referred to as 'phase constant', L_x is the periodic element's length in the x direction and k_x is the wavenumber. The complete vector of the local degrees of freedom can be ordered as follows

$$\mathbf{q} = \begin{bmatrix} \mathbf{q}_I^T & \mathbf{q}_L^T & \mathbf{q}_R^T \end{bmatrix}^T. \tag{3.3}$$

The equation of motion for the cell including damping [145] is given by

$$\left[\mathbf{K} + \mathrm{i}\omega\mathbf{C} - \omega^2\mathbf{M}\right]\mathbf{q} = \mathbf{f}, \tag{3.4}$$

where $\mathbf{K}$, $\mathbf{M}$ and $\mathbf{C}$ are the stiffness, mass and damping matrices respectively and $\mathbf{f}$ is the vector of the nodal forces. Eq. (3.4) can be used when proportional damping is available [146], where damping is expressed as a linear combination of the mass and stiffness matrices, that is,

$$\mathbf{C} = \alpha_1\mathbf{M} + \alpha_2\mathbf{K}, \tag{3.5}$$

where α_1 and α_2 are real scalars. In the case of structural damping [62, 145], the equation of motion becomes

$$\left[\mathbf{K} + \mathrm{i}\mathbf{C} - \omega^2\mathbf{M}\right]\mathbf{q} = \mathbf{f}, \tag{3.6}$$

and the structural damping matrix $\mathbf{C}$ is given by

$$\mathbf{C} = \sum_{i=1}^{n_e} \mathbf{K}_i \eta_i, \tag{3.7}$$

where n_e is the number of the FEs of the unit cell, $\mathbf{K}_i$ is the stiffness matrix of the i_{th} element and η_i is the loss factor of the corresponding element. Eq. (3.6) can be written as

$$\left[\mathbf{K}(1 + \mathrm{i}\eta) - \omega^2 \mathbf{M}\right] \mathbf{q} = \mathbf{f}. \tag{3.8}$$

In this work (more specifically in Chapter 5 and 6 where damping is included in the calculations), the focus is not on the accuracy of the model of damping, since the main aim of the wave propagation analysis is to examine the existence of the band gap. In order to write the propagation relation in Eq. (3.1) in matrix form, a transformation matrix $\mathbf{R}$ is considered, which is given in the following equation:

$$\mathbf{q} = \begin{bmatrix} \mathbf{I} & \mathbf{0} \\ \mathbf{0} & \mathbf{I} \\ \mathbf{0} & \mathbf{I}\mathrm{e}^{-\mathrm{i}\varepsilon_x} \end{bmatrix} \mathbf{x} = \mathbf{R}\mathbf{x}. \tag{3.9}$$

In this way, the equation becomes

$$\mathbf{q} = \mathbf{R}\mathbf{q}', \tag{3.10}$$

where

$$\mathbf{q}' = \mathbf{x} = \begin{bmatrix} \mathbf{q}_I & \mathbf{q}_L \end{bmatrix}^T. \tag{3.11}$$

In the absence of external forces (free wave propagation), it is written:

$$\mathbf{R}^H \mathbf{f} = \mathbf{0}, \tag{3.12}$$

where $\mathbf{R}^H$ denotes the complex conjugate (Hermitian) transpose of $\mathbf{R}$. The resulting homogenous equations in the reduced set of degrees of freedom are then given by

$$\left[\mathbf{K}' + \mathrm{i}\omega\mathbf{C}' - \omega^2\mathbf{M}'\right] \mathbf{q}' = \mathbf{0}, \tag{3.13}$$

and

$$\left[\mathbf{K}'(1 + \mathrm{i}\eta) - \omega^2\mathbf{M}'\right] \mathbf{q}' = \mathbf{0}, \tag{3.14}$$

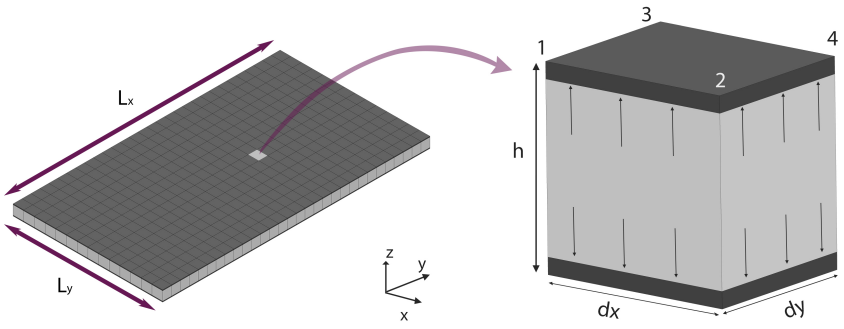


Figure 3.3: Representation of the modelled internally pressurised periodic segment with its edges 1, 2, 3 and 4

where

$$\mathbf{K}' = \mathbf{R}^H(\varepsilon_x)\mathbf{K}\mathbf{R}(\varepsilon_x), \quad \mathbf{M}' = \mathbf{R}^H(\varepsilon_x)\mathbf{M}\mathbf{R}(\varepsilon_x), \quad \mathbf{C}' = \mathbf{R}^H(\varepsilon_x)\mathbf{C}\mathbf{R}(\varepsilon_x). \tag{3.15}$$

When a set of phase constants ε_x is specified, a quadratic eigenvalue problem is formed for Eq. (3.13), the solution method of which is described elsewhere [147]. Eq. (3.14) gives a standard eigenvalue problem with eigenvalues $\lambda = \omega^2$ indicating the frequencies at which a wave can propagate in the structure when a given phase is specified between the edges of the cell. It is noted that in Chapter 5 and 6, only the real part of the eigenvalues is examined since the target of the examination is the band gap behaviour.

3.1.1 The two dimensional WFEM

A laminate of $L_{l,x}$ length and $L_{l,y}$ width is considered and a FE model of a small segment of the laminate is considered. This segment's length is dx, while its width is dy (Fig. 3.3). The segment is meshed using commercially available FE software. The vector of the DOFs $\mathbf{q}$ of the segment is given in terms of DOFs by [61]

$$\mathbf{q} = \begin{bmatrix} \mathbf{q}_1^T & \mathbf{q}_2^T & \mathbf{q}_3^T & \mathbf{q}_4^T \end{bmatrix}^T, \tag{3.16}$$

where T denotes the transpose and $\mathbf{q}_n$ is the vector of nodal DOFs of all the element nodes which lie on the nth corner of the element [61]. Following the same logic, the vector of nodal force is given by

$$\mathbf{f} = \begin{bmatrix} \mathbf{f}_1^T & \mathbf{f}_2^T & \mathbf{f}_3^T & \mathbf{f}_4^T \end{bmatrix}^T. \tag{3.17}$$

Conventional FE methods is then used to get the $\mathbf{M}$ and $\mathbf{K}$ matrices of the segment. Assuming time-harmonic behaviour and neglecting damping the equation is

$$[\mathbf{K} - \omega^2\mathbf{M}]\mathbf{q} = \mathbf{f}. \tag{3.18}$$

Using Floquet theorem for a rectangular segment and taking edge 1 as reference the equation becomes

$$\mathbf{q}_2 = \lambda_x\mathbf{q}_1, \quad \mathbf{q}_3 = \lambda_y\mathbf{q}_1, \quad \mathbf{q}_4 = \lambda_x\lambda_y\mathbf{q}_1, \tag{3.19}$$

where

$$\lambda_x = e^{-ik_x\,\mathrm{d}x}, \quad \lambda_y = e^{-ik_y\,\mathrm{d}y}, \tag{3.20}$$

with λ_x and λ_y being the phase constants and k_x and k_y being the wavenumbers. Thus

$$\mathbf{q} = \mathbf{\Lambda}_R\mathbf{q}_1, \quad \mathbf{\Lambda}_R = \begin{Bmatrix} \mathbf{I} \\ \lambda_x\mathbf{I} \\ \lambda_y\mathbf{I} \\ \lambda_x\lambda_y\mathbf{I}, \end{Bmatrix} \tag{3.21}$$

with $\mathbf{I}$ being the identity matrix. Assuming no external excitation, equilibrium at node 1 should give zero sum of nodal forces,

$$\mathbf{\Lambda}_L \begin{Bmatrix} \mathbf{f}_1 \\ \mathbf{f}_2 \\ \mathbf{f}_3 \\ \mathbf{f}_4 \end{Bmatrix} = 0, \quad \mathbf{\Lambda}_L = \begin{bmatrix} \mathbf{I} & \lambda_x^{-1}\mathbf{I} & \lambda_y^{-1}\mathbf{I} & \lambda_x^{-1}\lambda_y^{-1}\mathbf{I} \end{bmatrix}. \tag{3.22}$$

Dynamic stiffness $\mathbf{D}$ is introduced, which is

$$\mathbf{D} = \mathbf{K} - \omega^2\mathbf{M}. \tag{3.23}$$

In case of damping, viscous or structural damping can be taken into account by the addition of viscous or structural damping matrices $\mathbf{C}$ or $\mathbf{K}_I$. Then, the dynamic stiffness matrix is given by the following equations:

$$\mathbf{D} = \mathbf{K} + i\omega\mathbf{C} - \omega^2\mathbf{M}, \quad \textit{and} \quad \mathbf{D} = \mathbf{K} + i\mathbf{K}_I - \omega^2\mathbf{M}. \tag{3.24}$$

Following the analysis in [61] and substituting Eq.(3.21) and Eq.(3.22) in Eq.(3.18) the equation becomes

$$\mathbf{D}(\omega, \lambda_x, \lambda_y)\mathbf{q}_1 = 0. \tag{3.25}$$

If the segment dynamic stiffness matrix is partitioned to

$$\mathbf{D} = \begin{bmatrix} \mathbf{D}_{11} & \mathbf{D}_{12} & \mathbf{D}_{13} & \mathbf{D}_{14} \\ \mathbf{D}_{21} & \mathbf{D}_{22} & \mathbf{D}_{23} & \mathbf{D}_{24} \\ \mathbf{D}_{31} & \mathbf{D}_{32} & \mathbf{D}_{33} & \mathbf{D}_{34} \\ \mathbf{D}_{41} & \mathbf{D}_{42} & \mathbf{D}_{43} & \mathbf{D}_{44} \end{bmatrix}, \tag{3.26}$$

then the eigenproblem of Eq.(3.25) can be written in the following form

$$\begin{aligned} [(\mathbf{D}_{11} + \mathbf{D}_{22} + \mathbf{D}_{33} + \mathbf{D}_{44}) + (\mathbf{D}_{12} + \mathbf{D}_{34})\lambda_x + (\mathbf{D}_{21} + \mathbf{D}_{43})\lambda_x^{-1} \\ + (\mathbf{D}_{13} + \mathbf{D}_{24})\lambda_y + (\mathbf{D}_{31} + \mathbf{D}_{42})\lambda_y^{-1} + \mathbf{D}_{14}\lambda_x\lambda_y + \mathbf{D}_{41}\lambda_x^{-1}\lambda_y^{-1} \\ + \mathbf{D}_{32}\lambda_x\lambda_y^{-1} + \mathbf{D}_{23}\lambda_x^{-1}\lambda_y]\mathbf{q}_1 = 0. \end{aligned} \tag{3.27}$$

In [54] and [61] different methods were presented for solving the eigenproblem of Eq.(3.27). In this work the method used in [67] is preferred being faster and easier to implement in calculation tools. In [67] the frequency and the wavenumber towards the y direction are kept fixed and for each set of ω, k_y the k_x values are calculated. In addition to this, by interpolating the known results, values for intermediate ω, k_x and k_y can be found. For a set of fixed ω, k_y the non-linear eigenproblem of Eq.(3.27) is reduced to

$$(\mathbf{A}_2\lambda_x^2 + \mathbf{A}_1\lambda_x + \mathbf{A}_0)\mathbf{q}_1 = 0, \tag{3.28}$$

where

$$\mathbf{A}_i = \begin{cases} \mathbf{D}_{14}\lambda_y^2 + (\mathbf{D}_{12} + \mathbf{D}_{34})\lambda_y + \mathbf{D}_{32}, & i = 2 \\ (\mathbf{D}_{13} + \mathbf{D}_{24})\lambda_y^2 + (\mathbf{D}_{11} + \mathbf{D}_{22} + \mathbf{D}_{33} + \mathbf{D}_{44})\lambda_y + \mathbf{D}_{31} + \mathbf{D}_{42}, & i = 1 \\ \mathbf{D}_{23}\lambda_y^2 + (\mathbf{D}_{21} + \mathbf{D}_{43})\lambda_y + \mathbf{D}_{41}, & i = 0. \end{cases} \tag{3.29}$$

This quadratic eigenproblem can be converted [67] into an ordinary linear generalized eigenproblem, by introducing a new vector $\mathbf{z} = \lambda_x\mathbf{q}_1$

$$\begin{bmatrix} -\mathbf{A}_0 & 0 \\ 0 & \mathbf{I} \end{bmatrix} \begin{Bmatrix} \mathbf{q}_1 \\ \mathbf{z} \end{Bmatrix} = \lambda_x \begin{bmatrix} \mathbf{A}_1 & \mathbf{A}_2 \\ \mathbf{I} & 0 \end{bmatrix} \begin{Bmatrix} \mathbf{q}_1 \\ \mathbf{z} \end{Bmatrix}. \tag{3.30}$$

Then the wavenumbers are calculated as follows:

$$k_x = \frac{log(\lambda_x)}{-i\,\mathrm{d}x} \quad \text{and} \quad k_y = \frac{log(\lambda_y)}{-i\,\mathrm{d}y}. \tag{3.31}$$

Stress stiffening

In this work two different scenarios of pre-stressed structure are examined, as described in detail in Chapter 4 and 5. In these cases, a pre-stress stiffness matrix $\mathbf{K}_s$ is calculated. Considering that a static analysis has been solved, the updated stiffness matrix $\mathbf{K}$ is calculated [148]:

$$\mathbf{K} = \mathbf{K}_0 + \mathbf{K}_s, \tag{3.32}$$

where $\mathbf{K}_0$ is the original element stiffness matrix and:

$$\mathbf{K}_s = \iiint \mathbf{G}^T \tau \mathbf{G} \, \mathrm{d}x \, \mathrm{d}y \, \mathrm{d}z, \tag{3.33}$$

where $\mathbf{G}$ is a matrix of shape function derivatives and τ is a matrix of the current Cauchy (true) stresses σ in the global Cartesian system.

The updated matrix $\mathbf{K}$ is then used in WFEM to get the wavenumbers and eigenvectors of the pre-stressed structure.

3.1.2 Loss factor

As it is written in Sec. 3.1.1 damping can be included in the dynamic stiffness matrix $\mathbf{D}$ in WFEM. In Chapter 4 of this work, though, our attention is focused on the real part of the propagating waves, which are not affected by the damping of the material. The behaviour of loss factor under different scenarios is examined, which is a measure of the damping performance of a structure.

A physical interpretation of the loss factor is expressed as follows [149]:

$$\eta = \frac{1}{2\pi}\frac{W_d}{U_m} = \frac{1}{2\pi}\frac{\text{energy dissipated per cycle}}{\text{maximum strain energy}}. \tag{3.34}$$

Following the analysis in [62], the loss factor η_j as a function of the frequency is calculated:

$$\eta_j(\omega, T, \phi) = \frac{\mathbf{V}_j^* \mathbf{K}^{"}_{\omega,T} \mathbf{V}_j}{\mathbf{V}_j^* \mathbf{K}^{'}_{\omega,T} \mathbf{V}_j}, \tag{3.35}$$

where $*$ stands for the Hermitian transpose, T for the temperature, $\mathbf{K}^{"}_{\omega,T}$ and $\mathbf{K}^{'}_{\omega,T}$ for the imaginary and real part of the stiffness matrix, respectively, $\mathbf{V}_j$ is the displacement vector associated with the jth propagating wave

and is obtained from the wave mode $\mathbf{q}_{1j}$ [61] and the components of the wavenumber k_{xj} and k_{yj}, that is:

$$\mathbf{V}_j = \left[\mathbf{q}_{1j}^T \quad e^{-ik_{xj}L_x}\mathbf{q}_{1j}^T \quad e^{-ik_{yj}L_y}\mathbf{q}_{1j}^T \quad e^{-ik_{xj}L_x}e^{-ik_{yj}L_y}\mathbf{q}_{1j}^T\right]^T. \tag{3.36}$$

In our case temperature is not accounted for. So

$$\eta_j(\omega,\phi) = \frac{\mathbf{V}_j^*\mathbf{K}_\omega^{"}\mathbf{V}_j}{\mathbf{V}_j^*\mathbf{K}_\omega^{'}\mathbf{V}_j}. \tag{3.37}$$

Also, it is used, along with $\mathbf{K}_s$ to calculate the loss factor $\eta_{s(j)}$ of the pre-stressed structure [64]:

$$\eta_{s(j)}(\omega,\phi) = \frac{\mathbf{V}_j^*\mathbf{K}_\omega^{"}\mathbf{V}_j}{\mathbf{V}_j^*(\mathbf{K}_\omega + \mathbf{K}_{s(\omega)})\mathbf{V}_j}. \tag{3.38}$$

3.2 Computation of the energy analysis quantities

3.2.1 Calculation of the modal density

Modal density is defined as the average number of modes per unit frequency. Using a formula that has been used elsewhere [56, 150], an equation is produced which expresses the modal density of each propagating wave type w for each angle ϕ as a function of the propagating wavenumber and its corresponding group velocity c_g

$$n_w(\omega,\phi) = \frac{Ak_w(\omega,\phi)}{2\pi^2|c_{g,w}(\omega,\phi)|}, \tag{3.39}$$

where A is the area of the examined panel and the group velocity is expressed as

$$c_g(\omega,\phi) = \frac{\mathrm{d}\omega}{\mathrm{d}k(\omega,\phi)}. \tag{3.40}$$

Then, the modal density after having been angularly averaged is given as a function of frequency:

$$n_w(\omega) = \int_0^\pi n_w(\omega,\phi)\,\mathrm{d}\phi. \tag{3.41}$$

3.2.2 Calculation of the radiation efficiency

In order to calculate the radiation efficiency $\sigma(k(\omega))$ the set of asymptotic formulas given in [40] is used. Mode shapes of sinusoidal form can be assumed for continuous structures so that any FE discretization errors to be avoided. Working in a SEA context, energy equipartition amongst the resonant modes is assumed so that:

$$\sigma_{rad(\omega)} = \frac{1}{n(\omega)} \int_0^{\pi} \sigma(\kappa(\omega, \phi)) n(\omega, \phi) \, \mathrm{d}\phi. \tag{3.42}$$

For a periodic discontinuous structure the assumption of sinusoidal mode shapes is no longer valid, which means that the radiation efficiency should be calculated from the WFEM derived wave mode shapes. Therefore, the radiation efficiency expression given in [54] can be used. In the next section the equations used to calculate the STL, modal density and radiation efficiency are presented.

3.2.3 Calculation of the STL of a panel by an SEA approach

The STL (or TL) is considered to be a property of great importance which is crucial to examine and quantify the characterisation of the vibroacoustic performance of a structure. The theoretical system examined in this work consists of two reverberant chambers separated by the modelled panel which is attached to a rigid baffle. Any flanking transmission is neglected in the SEA model. In Fig. 3.4 a graphical representation of the model is depicted, along with the energy balance of the subsystems of the SEA approach [51], where E_1 and E_3 are the acoustic energy of the source room and the receiving room respectively and E_2 is the vibrational energy of the panel. P_{in} is the injected power in the source room, P_{1d}, P_{2d} and P_{3d} are the power dissipated by each sub-system and P_{13} is the non-resonant transmitted power between the rooms. Considering each wave type $w = a, b, c...n$ propagating within

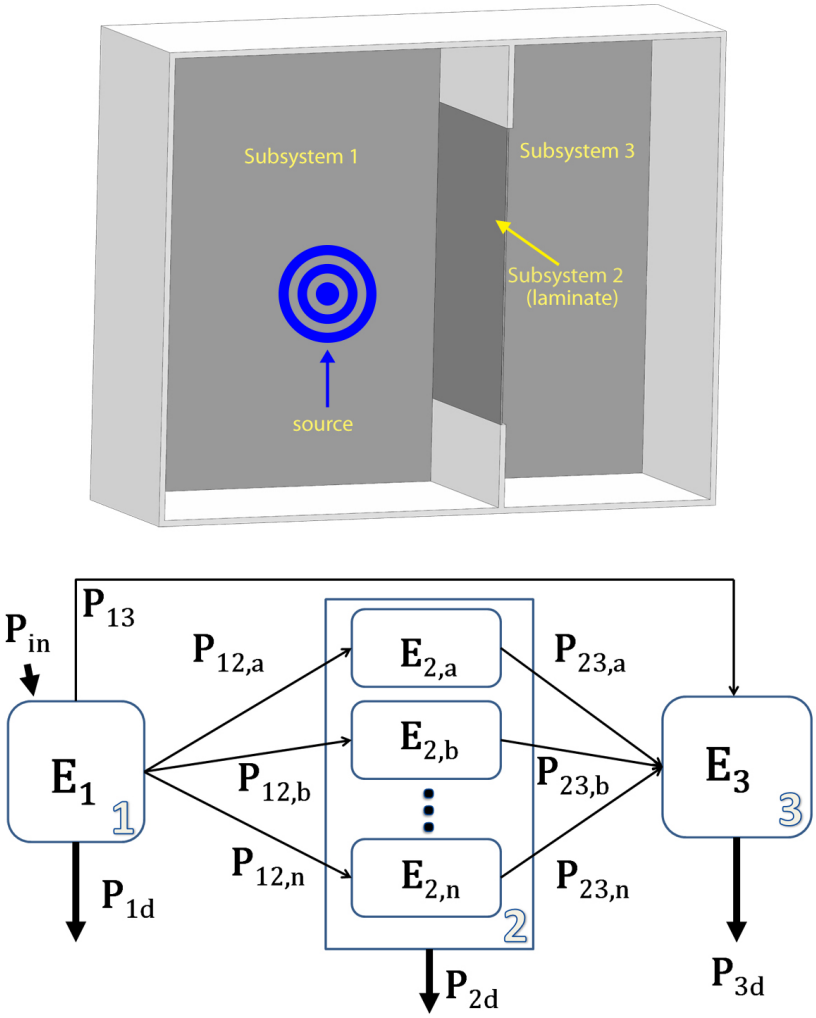


Figure 3.4: Representation of the considered SEA model and all the energy and power exchanges between the systemts of the model.

the panel as a separate SEA subsystem:

$$\begin{aligned} P_{12} &= \sum_{w=a}^{n} P_{12,w} \\ P_{23} &= \sum_{w=a}^{n} P_{23,w} \end{aligned}, \tag{3.43}$$

where P_{12} and P_{23} stand for the power flow between the rooms and the panel. The STL is then calculated by the equation:

$$STL = 10 \log_{10} \left(\frac{1}{\tau} \right), \tag{3.44}$$

where τ is the transmission coefficient which represents the ratio between the transmitted and the incident sound powers. τ can be written as the sum of the resonant and the non-resonant transmission coefficient

$$\tau = \frac{P_{23} + P_{13}}{P_{inc}} = \sum_{w=a}^{n} \frac{P_{23,w}}{P_{inc}} + \frac{P_{13}}{P_{inc}}, \tag{3.45}$$

where P_{inc} is the acoustic power incident on the panel, which for a reverberant sound field can be expressed as:

$$P_{inc} = \frac{\langle p_1^2 \rangle A}{4 \rho c}, \tag{3.46}$$

where $\langle p_1^2 \rangle$ is the mean-square sound pressure. Using the calculations made in [67] the resonant coefficient for each wave type w is examined. Assuming no energy exchanges between different wave types within the panel, the energy balance of a structural wave subsystem can be expressed as:

$$P_{12,w} = P_{2d,w} + P_{23,w}. \tag{3.47}$$

The power dissipated is:

$$P_{2d,w} = E_{2,w} \omega \eta_{2,w}, \tag{3.48}$$

with $\eta_{2,w}$ being the structural loss factor of the wave type w. The loss factor is a known property of most isotropic materials and can be calculated in layered structures if each layer's loss factor is known [151]. In this work, as shown in Sec. 3.1.2 the loss factor is calculated as a function of frequency for both non-stressed and pre-stressed analyses. The vibrational energy of the panel due to wave type w was written as:

$$E_{2,w} = \rho_s A \langle v_w^2 \rangle, \tag{3.49}$$

where ρ_s is the mass per unit area, A is the total area of the panel and $\langle v_w^2 \rangle$ is the mean-square panel vibration velocity due to wave type w. The power flow $P_{12,w}$ can be written using the SEA reciprocity rule as:

$$P_{12,w} = \omega \eta_{12,\omega} n_1 \left(\frac{E_1}{n_1} - \frac{E_{2,w}}{n_{2,w}} \right) = \omega \eta_{21,w} n_{2,w} \left(\frac{E_1}{n_1} - \frac{E_{2,w}}{n_{2,w}} \right), \tag{3.50}$$

where n_1 and $n_{2,w}$ are the modal density of the source room and of the wave type w respectively and $\eta_{21,w}$ is the coupling loss factor between the receiving room and the wave type w which is written as:

$$\eta_{21,w} = \eta_{23,w} = \frac{\rho c \sigma_{rad,w}}{\rho_s \omega}, \tag{3.51}$$

where ρ is the acoustic medium density of the room. The total acoustic energy of the source room is:

$$E_1 = \frac{\langle p_1^2 \rangle V}{\rho c^2}, \tag{3.52}$$

where V is the volume of the room. Following the analysis in [67], the total transmission coefficient of the panel t is expressed as:

$$\tau = \sum_{\omega=a}^{n} \tau_\omega + \frac{P_{13}}{P_{inc}}, \tag{3.53}$$

where

$$\tau_w = \frac{8 \rho^2 c^4 \pi \sigma_{rad,w}^2 n_{2,w}}{\rho_s \omega^2 A (\rho_s \omega n_{2,w} + 2 \rho c \sigma_{rad,w})}. \tag{3.54}$$

The non-resonant transmission coefficient $\tau_{nr} = P_{13}/P_{inc}$ for a diffused acoustic field is written as:

$$\frac{P_{13}}{P_{inc}} = \frac{\int_0^{2pi} \int_0^{\theta_{max}} \frac{4 Z_0^2 \sigma(\theta,\phi,\omega) sin\theta cos^2\theta}{|i\omega\rho_s + 2Z_0|^2} \, \mathrm{d}\theta \, \mathrm{d}\phi}{\pi (1 - cos^2\theta_{max})}, \tag{3.55}$$

in which θ and ϕ are the incidence angle and the direction angle of the acoustic wave respectively, and $Z_0 = \rho c / cos\theta$ is the acoustic impedance of the medium. The term θ_{max} is the maximum incidence angle, accounting for the diffuseness of the incident field. In this work $\theta_{max} = \pi/2$ is considered. The term $\sigma(\theta, \phi, \omega)$ is the corrected radiation efficiency term, which is used to account for the finite dimensions of the panel by accounting for the radiation of the mass controlled non-resonant modes, and it is calculated

using a spatial windowing correction technique presented in [152], where the equations after the relevant variables changes are:

$$Z = j\rho\omega L_y \int_0^2 \int_0^2 (2-u)(2-u_t)K(u,u_t)F_n(u,u_t)dudu_t, \tag{3.56}$$

where

$$K(u,u_t) = \frac{e^{-j\frac{\omega L_{l,x}}{2c}\sqrt{u^2+\frac{u^2}{r^2}}}}{\sqrt{u^2+\frac{u^2}{r^2}}} \tag{3.57}$$

and

$$F_n(u,u_t) = e^{-j\frac{\omega L_{l,x}}{2c}(ucos(\phi)+\frac{u_t}{r}sin(\phi))} \tag{3.58}$$

In Eq.(3.53) the total transmission coefficient of the panel is expressed merely as a function of its SEA quantities and independently of the room dimensions and modal energies. In the following chapter the script that transfers all the equations mentioned so far to MATLAB and ANSYS is presented.

3.3 Script's structure

The methodology described in the previous sections is transferred in MATLAB and ANSYS environments through a master script generated specifically for this purpose which combines newly developed scripts with embedded existing tools [153]. The master script takes as input the geometry of the unit cell of the examined structure as produced in the FE software and gives as output the wave propagation characteristics of the periodic structure (Figure 3.5). The steps are described in detail below:

- The geometry of the unit cell of the examined structure is produced in .txt file of ANSYS script language. This file also includes the material properties of the structure and these properties are assigned to each element of the cell to represent the actual structure.

- A simple and quick modal analysis is solved using ANSYS through the script so that mass, damping and stiffness matrices can be calculated. Using FE software to retrieve mass and stiffness matrices allows the user to simulate complex geometries.

- The matrices are retrieved by the script and moved to the folder-in-use.
- Then the matrices need to be converted to form MATLAB sparse matrices. For this step a freeware converter script is incorporated in the script [153] in order to convert the ANSYS matrices format (Harwell Boeing, HB) to MATLAB format.
- After having the matrices in MATLAB format, the mathematical script of the PST equations is run. This script can solve both one- and two-dimensional case studies.
- Finally, the wave propagation curve is calculated and plotted. In this step additional post-processing scripts can be implemented, such as the one that is used in Chapter 4 to calculate the acoustic performance of periodic structures.

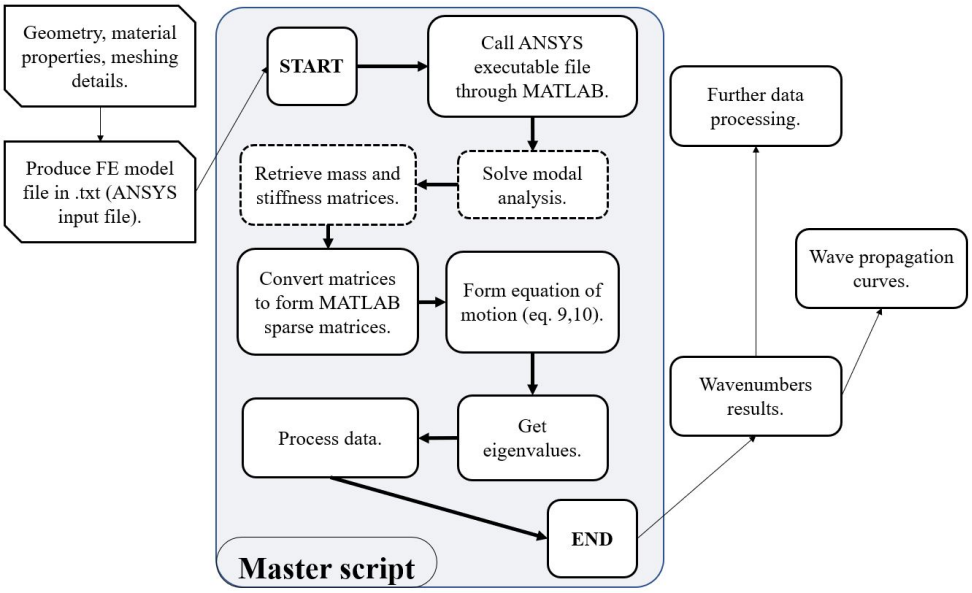


Figure 3.5: Flow diagram of the master script used to acquire wave propagation characteristics of the examined structures. The text boxes with dashed lines are ANSYS processes while the rest of them are MATLAB ones.

The script offers the chance to examine different structures quickly, since the only thing that the user needs to produce is the geometry and the material

properties file as all the rest is automated and included in the master script. A process that normally takes more than five minutes if done manually and includes the risk of human errors, with this script is completed in at least one tenth of the time. In addition to this, its automated nature allows the user to implement it in optimisation algorithms along with post-processing scripts, such as band gap calculation as presented in the following section.

3.4 Optimisation

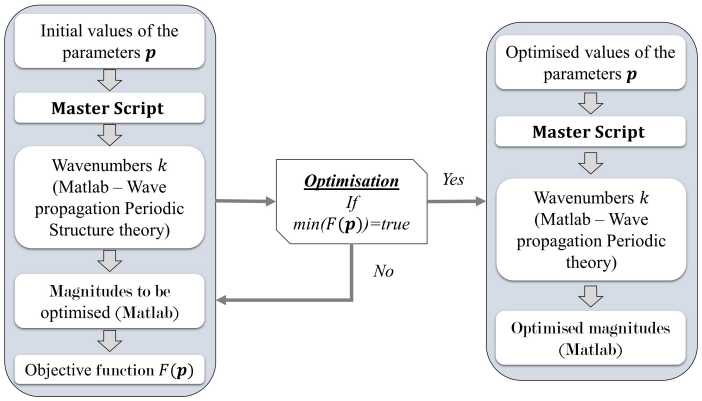


Figure 3.6: Flow chart of the optimisation method. The method takes advantage of the fast calculation of wave propagation thanks to the master script and finds the optimal solution quicker than the full method when the whole model has to be solved.

The optimisation method (see Fig. 3.6) that is employed to calculate the optimal structure design is described below. The set of parameters can be expressed as

$$\mathbf{p} = \{\beta_1, \beta_2, \ldots, \beta_n\}, \tag{3.59}$$

where n is the number of parameters examined. The design values may be considered to be constrained (e.g. $\beta_i \in [\beta_{i,\min}, \beta_{i,\max}]$). The considered variables are the mass m, the bending stiffness b_s, the band gap's width b_g and the mid-point frequency of the band gap $b_g_{m_f}$ (aiming for band gaps at frequencies as low as possible) of the stiffened plate. Examples of parameters β_i would be any geometrical characteristic of the stiffener or the plate itself,

such as thickness, that affects the considered variables. In order to have faster convergence and avoid the generation of multiple solutions, gradient based optimisation is preferred with optimising an objective function. The objective function for the specific structure is

$$\begin{aligned} F(\mathbf{p}) =& a_3 \times m^3 + a_2 \times m^2 + a_1 \times m + a_0 + b_3 \times b_s^3 + b_2 \times b_s^2 + b_1 \times b_s + b_0 \\ &+ c_3 \times b_g^3 + c_2 \times b_g^2 + c_1 \times b_g + c_0 + d_3 \times b_g_{m_f}^3 + d_2 \times b_g_{m_f}^2 + \\ &d_1 \times b_g_{m_f} + d_0, \end{aligned} \tag{3.60}$$

where a_i, b_i, c_i and d_i are the coefficients given by the design cost functions (for example see Fig. 6.2 in Chapter 6). Adjusting these coefficients the designers are given the ability to apply polynomial curves to available cost data forming the cost functions of the optimisation, as can be seen in Chapter 6 (see Fig. 6.2). Additionally, this type of objective function renders its differentiability and the calculation of its partial gradients efficient. Higher order polynomial or exponential fitting functions may be applied without loss of accuracy. The gradient of $F(\mathbf{p})$ can, therefore, be computed as

$$\nabla F(\mathbf{p}) = \left\{ \frac{\partial F(\mathbf{p})}{\partial \beta_i} \right\}^T. \tag{3.61}$$

By definition: $b_g = f_2 - f_1$, $b_g_{m_f} = \frac{f_1+f_2}{2}$ and $f_i = \frac{\omega_i}{2\pi}$, $\lambda_i = \omega_i^2$, where f_1 and f_2 are the frequencies at the lower and upper bound of the band gap. Thus,

$$\frac{\partial b_g}{\partial \beta_i} = \frac{\partial f_2}{\partial \beta_i} - \frac{\partial f_1}{\partial \beta_i} = \frac{1}{2\pi}\frac{\partial \omega_2}{\partial \beta_i} - \frac{1}{2\pi}\frac{\partial \omega_1}{\partial \beta_i} = \frac{1}{2\pi}\left(\frac{\partial \sqrt{\lambda_2}}{\partial \beta_i} - \frac{\partial \sqrt{\lambda_1}}{\partial \beta_i}\right), \tag{3.62}$$

$$\frac{\partial b_g_{m_f}}{\partial \beta_i} = \frac{1}{2}\left(\frac{\partial f_1}{\partial \beta_i} + \frac{\partial f_2}{\partial \beta_i}\right) = \frac{1}{4\pi}\left(\frac{\partial \omega_1}{\partial \beta_i} + \frac{\partial \omega_2}{\partial \beta_i}\right) = \frac{1}{4\pi}\left(\frac{\partial \sqrt{\lambda_1}}{\partial \beta_i} + \frac{\partial \sqrt{\lambda_2}}{\partial \beta_i}\right). \tag{3.63}$$

Taking advantage of the chain rule of differentiation, the following equations are formed:

$$\frac{\partial \sqrt{\lambda_i}}{\partial \beta_i} = \frac{\partial \sqrt{\lambda_i}}{\partial \lambda_i}\frac{\partial \lambda_i}{\partial \beta_i} = \frac{1}{2\sqrt{\lambda_i}}\frac{\partial \lambda_i}{\partial \beta_i}, \tag{3.64}$$

where the partial derivatives of the eigenvalues are calculated based on the

following techniques, given elsewhere [154, 155]:

$$\frac{\partial \lambda_i}{\partial \beta_i} = \frac{-\mathbf{x}^T \left(\lambda_i^2 \frac{\partial \mathbf{M}}{\partial \beta_i} + \lambda_i \frac{\partial \mathbf{C}}{\partial \beta_i} + \frac{\partial \mathbf{K}}{\partial \beta_i} \right) \mathbf{x}}{\mathbf{x}^T (2\lambda_i \mathbf{M} + \mathbf{C}) \mathbf{x}}, \tag{3.65}$$

where $\mathbf{x} = \mathbf{q}' = \begin{bmatrix} \mathbf{q}_I & \mathbf{q}_L \end{bmatrix}^T$ is the eigenvector. In this work, the partial derivatives of $\mathbf{K}$, $\mathbf{M}$ and $\mathbf{C}$ are calculated considering a perturbation of 0.1% of the examined parameter β_i, a percentage that was the result of a convergence analysis. Thus:

$$\frac{\partial \mathbf{K}}{\partial \beta_i} = \frac{\mathbf{K}_p - \mathbf{K}_0}{\beta_{i,p} - \beta_{i,0}}, \qquad \frac{\partial \mathbf{M}}{\partial \beta_i} = \frac{\mathbf{M}_p - \mathbf{M}_0}{\beta_{i,p} - \beta_{i,0}}, \qquad \frac{\partial \mathbf{C}}{\partial \beta_i} = \frac{\mathbf{C}_p - \mathbf{C}_0}{\beta_{i,p} - \beta_{i,0}}, \tag{3.66}$$

where $\mathbf{K}_p$, $\mathbf{M}_p$ and $\mathbf{C}_p$ are the perturbed stiffness, mass and damping matrices, $\beta_{i,p}$ is the perturbed considered parameter and $\beta_{i,0}$ the unperturbed parameter. The mass, stiffness and damping matrices $\mathbf{M}$, $\mathbf{K}$ and $\mathbf{C}$ of the unit cell can also be formed by assembling the local mass, stiffness and damping matrices of individual FEs, which can be calculated analytically [156]. It is, therefore, evident that when the expressions of the partial derivatives for every local mass, stiffness and damping matrix $\frac{\partial \mathbf{m}}{\partial \beta_i}$, $\frac{\partial \mathbf{k}}{\partial \beta_i}$ and $\frac{\partial \mathbf{c}}{\partial \beta_i}$ are known, then the expressions for the global matrices $\frac{\partial \mathbf{M}}{\partial \beta_i}$, $\frac{\partial \mathbf{K}}{\partial \beta_i}$ and $\frac{\partial \mathbf{C}}{\partial \beta_i}$ can be derived simply by assembling the expressions of the local matrices together. Therefore:

$$\frac{\partial \lambda_i}{\partial \beta_i} = \frac{-\mathbf{x}^T \left(\lambda_i^2 \mathbf{R}^H \frac{\partial \mathbf{M}}{\partial \beta_i} \mathbf{R} + \lambda_i \mathbf{R}^H \frac{\partial \mathbf{C}}{\partial \beta_i} \mathbf{R} + \mathbf{R}^H \frac{\partial \mathbf{K}}{\partial \beta_i} \mathbf{R} \right) \mathbf{x}}{\mathbf{x}^T (2\lambda_i \mathbf{R}^H \mathbf{M} \mathbf{R} + \mathbf{R}^H \mathbf{C} \mathbf{R}) \mathbf{x}}. \tag{3.67}$$

The calculation of $\frac{\partial b_s}{\partial \beta_i}$, $\frac{\partial m}{\partial \beta_i}$ depends on the geometric and material properties of the case study for which the optimisation method is applied. A constrained nonlinear interior point optimisation algorithm using Newton's method [157] is employed to compute the optimal parameter vector $\mathbf{p}$ that minimises $F(\mathbf{p})$. It should be noted that the optimisation used in this work leads to results in significantly shorter times compared to those that examine the whole finite periodic structure, since it only needs the unit cell's wave propagation characteristics. Furthermore, the adaptability of the optimisation method allows the examination of any type of band gap mechanism (Bragg scattering, local resonance, inertial amplification and/or

combination of them). On the other hand, when boundary conditions are applied to the structure PST fails to include their effects on the dynamic and stop band behaviour. In the following section the experimental setup that is used to validate the numerical and FE calculations is presented.

3.5 Experimental setup

To validate the dynamic behaviour of the examined structures, a vibration experimental setup is designed and developed. After the necessary market research, an electrodynamic shaker (TBS K2007E1) is used to excite the specimen with the signal produced and analysed by a Polytec VIB-E-400 Junction Box using a fast Fourier transform (FFT) capacity. A single point laser vibrometer (Polytec PDV-100) is used to measure the displacement at several points on the specimen. An impedance head (PCB 288D01) is mounted on one edge of the specimen and provides the measurement of the input force on the mounting point of the specimen. The impedance head is then bolted on to the moving head of the shaker.

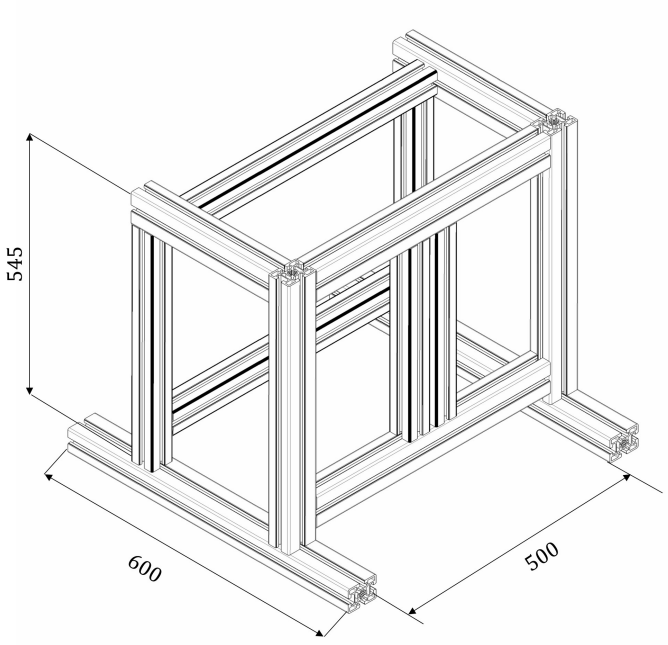


Figure 3.7: The design of the vibration experiment rig with key dimensions (in mm).

Having decided on the equipment, a rig had to be designed to accommodate the shaker. This rig had to be of considerable weight to avoid resonances in the frequency bands of interest and portable at the same time. The rig is designed so that the shaker can be mounted on all sides of it in order to accommodate the different sizes and shapes of the specimens and allow to excite the specimens without obstructing the use of the laser vibrometer. The main mounting points are situated on the two vertical beams in the middle of the rig, which offer adjustability along the vertical axis and stiff mounting points to accommodate the vibrational loading. Besides that, the shaker can be mounted on every side of the rig, since the grooves allow the fixing of specifically acquired nuts. The final design of the rig is shown in Fig. 3.7, with its weight being 15.3 kg. The laser vibrometer and the electrodynamic shaker can be seen in Fig. 3.8 and 3.9 respectively and the final setup in Fig. 3.10. In Fig. 3.11 the process of the experiment is described in detail. The experimental setup allows to examine specimens smaller than 600 mm in frequency range from 0 Hz to 9 kHz.



Figure 3.8: Polytec PDV-100 single point laser vibrometer.



Figure 3.9: TBS K2007E1 electrodynamic shaker with internal amplifier, along with the impedance head (PCB 288D01).

Having presented the development of the mathematical and numerical tools along with the experimental setup, the main work of this study is presented. In the next chapter the first application of the tools is described, where the vibroacoustic performance of pre-stressed composite structures is presented.

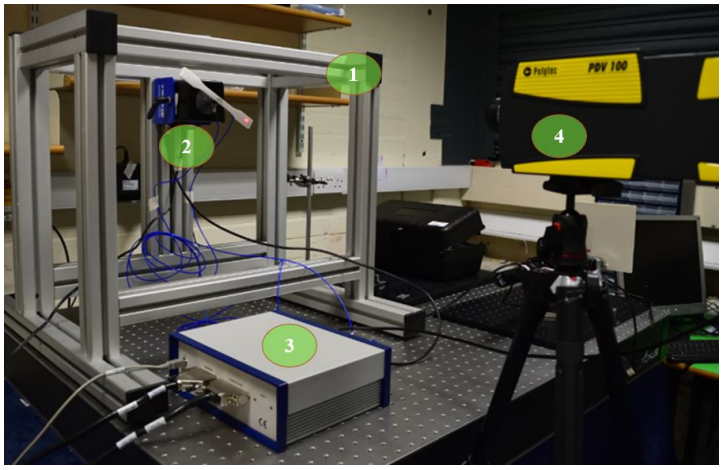


Figure 3.10: View of the vibration setup, including: 1) the rig made of aluminium profiles, 2) the TBS K2007E1 electrodynamic shaker along with the impedance head (PCB 288D01) , 3) the Polytec VIB-E-400 Junction Box and 4) the Polytec PDV-100 single point laser vibrometer.

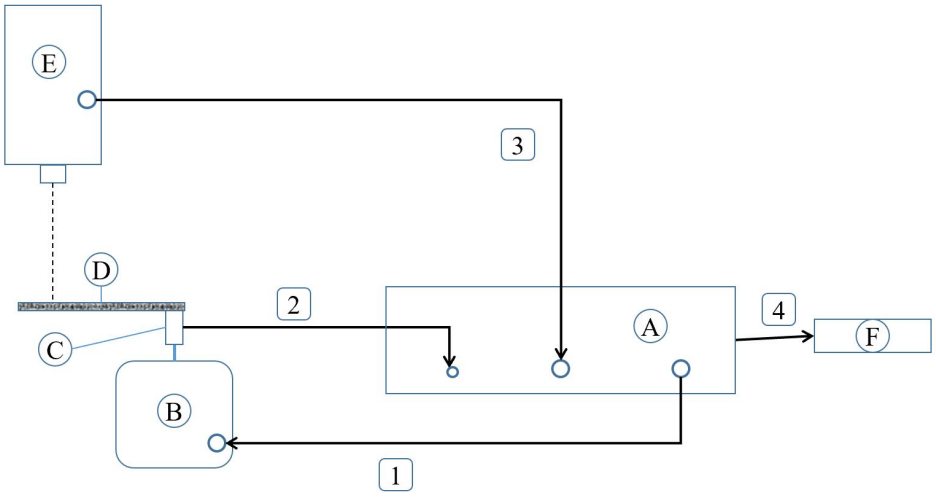


Figure 3.11: Graph of the vibration experiment process: 1) The Junction Box (A) generates the signal to excite the shaker (B). 2) The impedance head (C) gives as output the force acted on the specimen. 3) The laser vibrometer (E) measures the velocity, hence the acceleration of the specimen (D). 4) The desktop PC (F) handles the data and generates the relevant graphs as seen in the next sections.

Chapter 4: Acoustic transmission properties of pressurised and pre-stressed composite structures

4.1 Introduction

Pre-stress is the state where a constant load causes internal stresses to develop in the structure. This phenomenon is observed on an aircraft's wing, where there are several constant loads applied on it during a flight, such as the engine and its own weight and the lift force. Additionally, another common pre-stress scenario is the one observed in pressure vessels, where the internal pressure that is acted from the enclosed fluid on the vessel's walls causes strain on the walls. Therefore, it is important to examine the effect of the pre-stress on the acoustic and damping performance of the structure.

The first part of the work presented in this thesis consists of the examination of the effect of pre-stress, namely tension and pressure, on the wave propagation and acoustic and damping behaviour of composite monolithic and sandwich laminates. Using the core equations presented in 3.1.1, 3.1.2 and 3.2 and developing the initial version of the master script presented in 3.3 the crucial scenarios of pre-stress and pressurised structures are examined thoroughly.

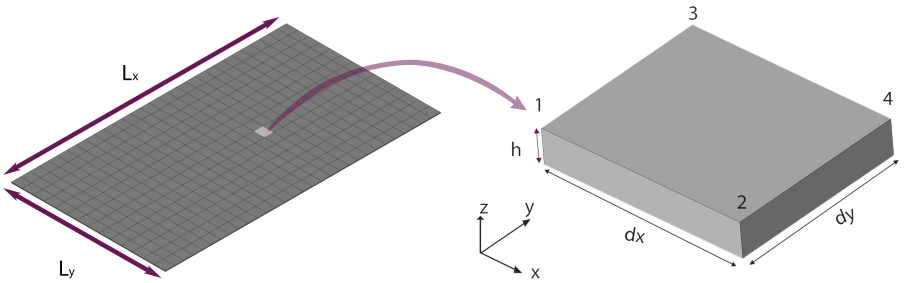


Figure 4.1: The examined laminate with a periodic cell of it, where its nodes and dimensions' symbols can be seen.

4.2 Numerical results

Two different representative composite laminates, a monolithic and a sandwich, are examined. These choices cover the majority of composite structures where sandwich is used to increase bending stiffness while monolithic one is used for its high tensile properties. Both are simulated under a scenario in which the plates are tensioned and compressed. The sandwich laminate is additionally examined in a different case where internal pressure is applied in its core, as it is shown in Fig. 4.13. The mechanical characteristics of each material used in the models are listed in Table 4.1, where E_i is the modulus of elasticity in direction i, v_{ij} is the Poisson's ratio for i and j being the directions of extension and contraction, respectively, ρ is the density and G_{ij} is the shear modulus of elasticity in direction j on the plane whose normal is in direction i. ANSYS 14.0 is used during the FE modelling. Linear 8-node ANSYS SOLID45 solid elements are chosen for the segment's meshing, which comprises of a 3D displacement field and three degrees of freedom per node (translations in the x, y, and z directions) [148]. This choice is dictated by the orthotropic nature of the materials. The maximum element size is kept below one tenth of the length of the minimum structural wave propagating in the frequency range of the analysis so that any interpolation errors are avoided.

Table 4.1: Material properties

Material I	Material II	Material III
$\rho = 1\ 870\ \text{kg/m}^3$	$\rho = 1\ 550\ \text{kg/m}^3$	$\rho = 110\ \text{kg/m}^3$
$E_x = 60e9$ Pa	$E_x = 48e9$ Pa	$E_x = 145e6$ Pa
$E_y = 60e9$ Pa	$E_y = 48e9$ Pa	$E_y = 145e6$ Pa
$E_z = 40e9$ Pa	$E_z = 48e9$ Pa	$E_z = 145e6$ Pa
$\nu_{xy} = 0.25$	$\nu_{xy} = 0.3$	$\nu_{xy} = 0.45$
$\nu_{yz} = 0.4$	$\nu_{yz} = 0.3$	$\nu_{yz} = 0.45$
$\nu_{xz} = 0.4$	$\nu_{xz} = 0.3$	$\nu_{xz} = 0.45$
$G_{xy} = 3.6e9$ Pa	$G_{xy} = 2.8e9$ Pa	$G_{xy} = 50e6$ Pa
$G_{yz} = 1.2e9$ Pa	$G_{yz} = 1.0e9$ Pa	$G_{yz} = 50e6$ Pa
$G_{xz} = 1.2e9$ Pa	$G_{xz} = 1.0e9$ Pa	$G_{xz} = 50e6$ Pa

4.2.1 Monolithic laminate - Tensioned and Compressed

In this part three different scenarios of the monolithic laminate are examined: the first one consists of the laminate with no force applied on it, the second one with $T = 100$ N tensile force applied in x direction and the third one with $T = -100$ N compressive force in x direction. The force represents a constant load acting on the laminate which could be a weight of a part of a structure. Its dimensions are $L_{l,x} = 2.5$ m, $L_{l,y} = 1.5$ m its length and width, and $h = 0.002$ m its thickness (Fig. 4.1). Material I (Table 4.1) is used in the analysis which represents a fibrous material with high mechanical properties. The flexural wavenumbers in x direction of all three scenarios are presented in Fig. 4.2. It can be seen that tension decreases the magnitude of the wavenumber, while compression increases it. This essentially means that a larger number of waves per unit distance are observed in the compressive load scenario where the structure is weakened and a smaller number of waves in the tensile load where the structure is stiffened, compared with the one that is not pre-stressed. This is explained by the weakening and stiffening which make the wave propagation easier and harder, respectively. The same trend is noticed in the loss factor be-

haviour in Fig. 4.3. This can be explained by the fact that in the first case the structure is stiffened, with the strain energy associated with the tension increased (in comparison with the bending one) resulting in decreasing of the loss factor (see Eq.(3.34)). Eq. (3.38) also explains this behaviour since $\mathbf{K}_s$ consists of real positive numbers when the laminate is tensioned (thus stiffened) and real negative numbers when the laminate is compressed (thus softened). In Manconi's work [64] on loss-factors of pre-stressed structures, results of the same nature were acquired examining pre-stressed beams and cylinders. It should be noted that these differences are normalized as frequency gets higher, with ~ 1 kHz being the frequency where the values tend to become equal. This can be explained by the fact that as the frequency gets higher the mass term dominates and the effect of the pre-stress gets lower. The same behaviour is noticed in most of the rest of the graphs. In Fig. 4.4 the modal densities of the three scenarios are depicted. It can be seen that, although both pre-stressed cases exhibit different behaviour than the non-stressed one, their results are identical in tensioned and compressed laminate. On the other hand, in Fig. 4.5 it is seen that in tensioned case the radiation efficiency is higher than in non-stressed case, while in compressed case the opposite is obvious, with radiation efficiency having lower values. This behaviour below the incidence can be explained by the relationship between the radiation efficiency and the wavenumber [40] where as the wavenumber gets higher the radiation efficiency gets lower. As mentioned before, these differences are normalized as frequency gets higher. In Fig. 4.6 the TL of the three scenarios are shown. Again, in tensioning case the TL is lower that the non-stressed in low frequencies. In compressive case, though, there is no significant difference compared to the non-stressed.

4.2.2 Sandwich laminate

A sandwich laminate with the same dimensions as the monolithic one (length $L_{l,x} = 2.5$ m, width $L_{l,y} = 1.5$ m) is modelled. Material II is used for the skin and Material III for the core. The core's thickness is $h_c = 0.0127$ m and the skins' one is $h_s = 0.0012$ m (Fig. 4.7).

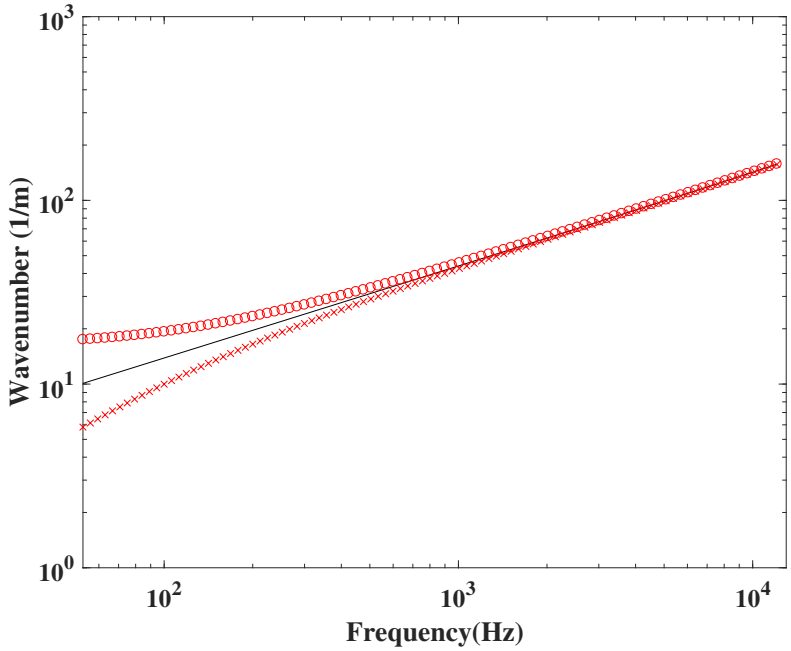


Figure 4.2: Comparison of the bending wavenumber (x-direction) of the monolithic laminate: (-) non-stressed, (x) pre-stressed, tensile force $T = 100$ N in x direction, (o) pre-stressed, compressive force $T = -100$ N in x direction

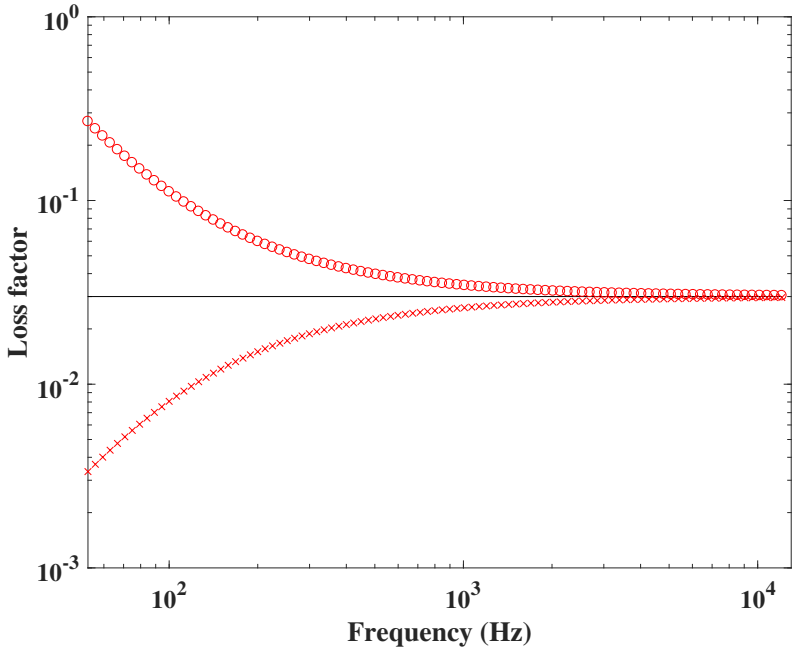


Figure 4.3: Comparison of the loss factor of the monolithic laminate: (-) non-stressed, (x) pre-stressed, tensile force $T = 100$ N in x direction, (o) pre-stressed, compressive force $T = -100$ N in x direction

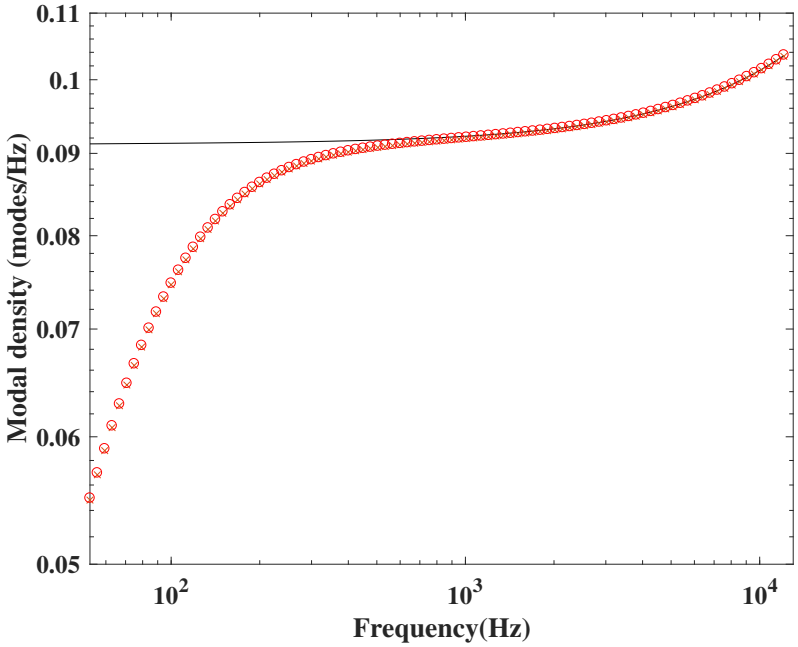


Figure 4.4: Comparison of the modal density of the monolithic laminate: (-) non-stressed, (x) pre-stressed, tensile force $T = 100$ N in x direction, (o) pre-stressed, compressive force $T = -100$ N in x direction

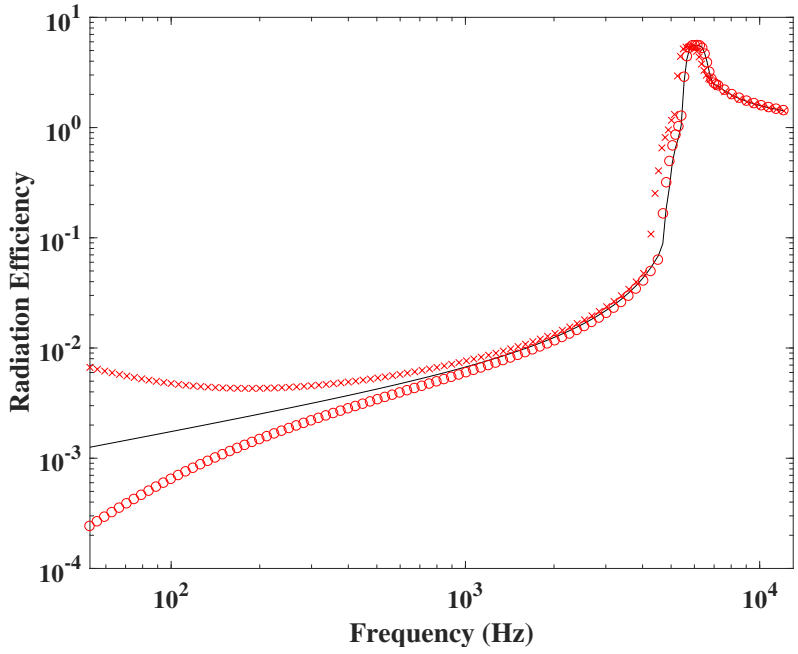


Figure 4.5: Comparison of the radiation efficiency of the monolithic laminate: (-) non-stressed, (x) pre-stressed, tensile force $T = 100$ N in x direction, (o) pre-stressed, compressive force $T = -100$ N in x direction

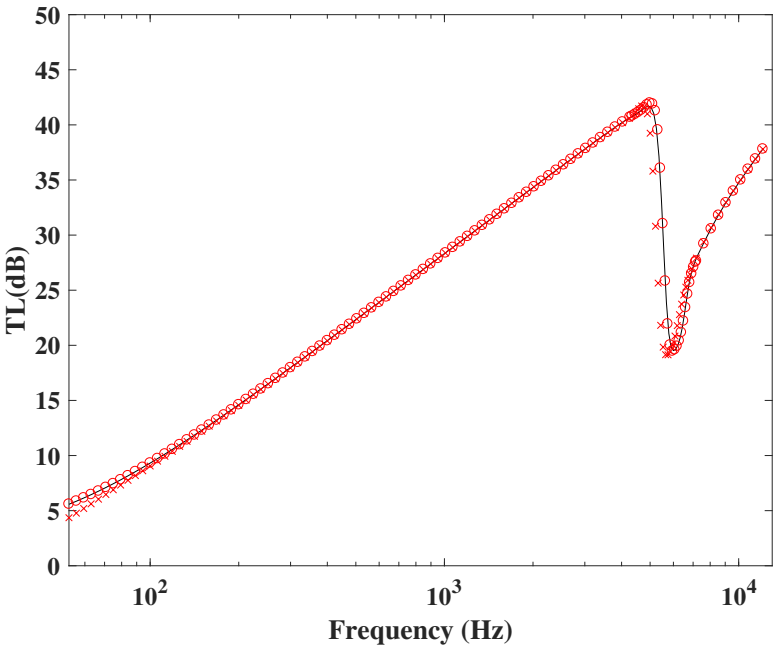


Figure 4.6: Comparison of the transmission loss of the monolithic laminate: (-) non-stressed, (x) pre-stressed, tensile force $T = 100$ N in x direction, (o) pre-stressed, compressive force $T = -100$ N in x direction

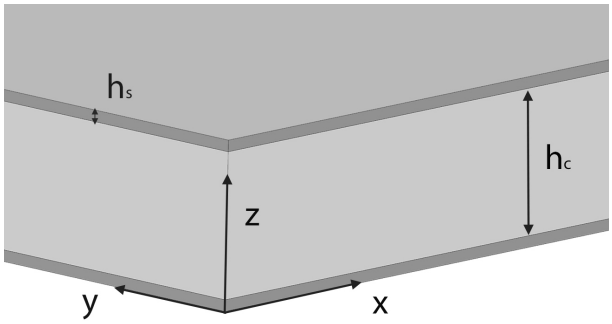


Figure 4.7: Representation of the sandwich laminate under consideration and its dimensions' symbols.

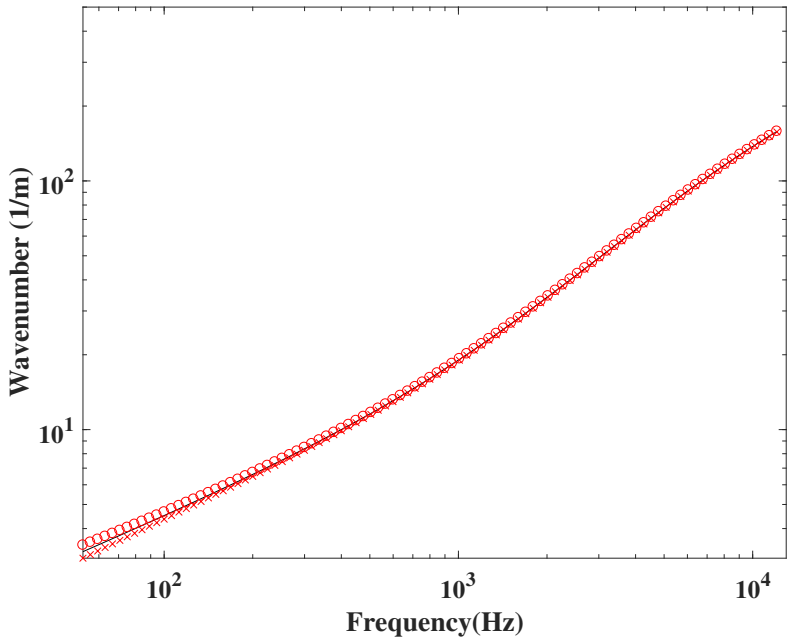


Figure 4.8: Comparison of the bending wavenumber (x-direction) of the sandwich plate: (-) non-stressed, (x) pre-stressed, tensile force $T = 100$ N in x direction, (o) pre-stressed, compressive force $T = -100$ N in x direction

Tensioned-Compressed

As in Sec. 4.2.1 three different scenarios are examined, with no force applied on the sandwich laminate and both tension and compression, $T = \pm 100$ N. In Fig. 4.8 the wavenumbers are depicted. In this case the same behaviour as in Fig. 4.2 is noticed, but the differences are of smaller scale due to the increased bending stiffness of the sandwich scheme. In Fig. 4.9 the loss factors are depicted. Again it is shown that the same behaviour as in Fig. 4.3 is noticed in sandwich laminate occasion. As it is written in 4.2.1, this is explained by the change in strain energy of the laminate. In Fig. 4.10, 4.11 and 4.12 the modal density, radiation efficiency and TL distributions are shown. In these cases the differences between the three scenarios are quite insignificant, which is attributed to the smaller scale of wavenumber change than the monolithic one. Also, it should be noted that all three of them are characterised by smoother curves than the monolithic laminate ones.

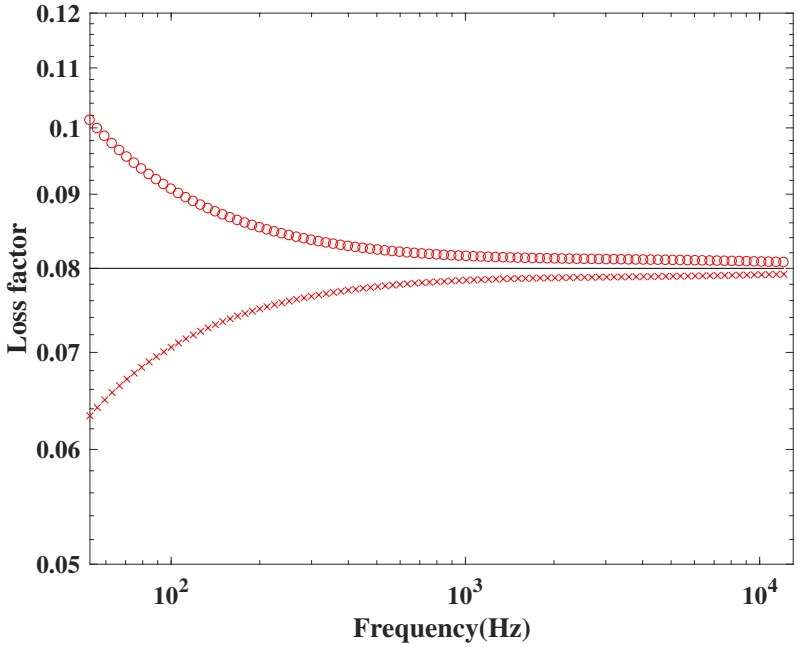


Figure 4.9: Comparison of the loss factor of the sandwich plate: (-) non-stressed, (x) pre-stressed, tensile force $T = 100$ N in x direction, (o) pre-stressed, compressive force $T = -100$ N in x direction

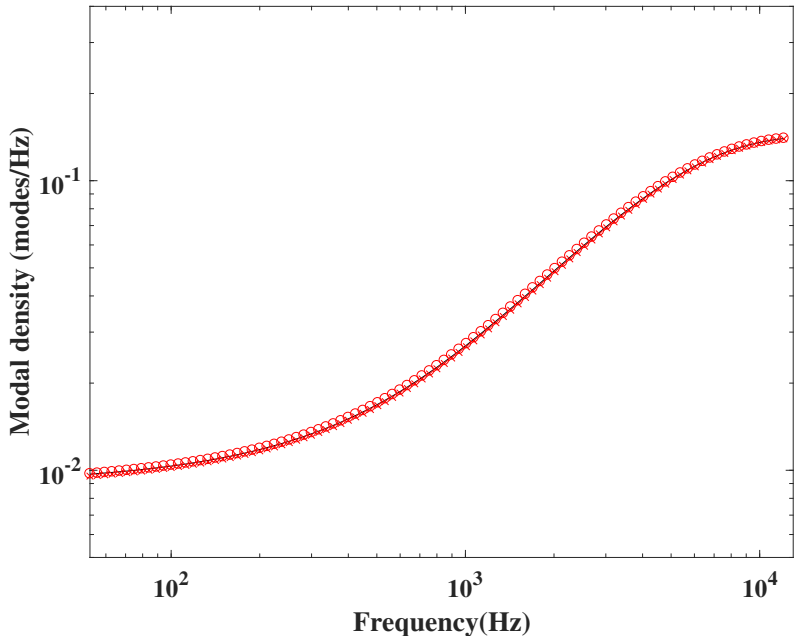


Figure 4.10: Comparison of the modal density of the sandwich plate: (-) non-stressed, (x) pre-stressed, tensile force $T = 100$ N in x direction, (o) pre-stressed, compressive force $T = -100$ N in x direction

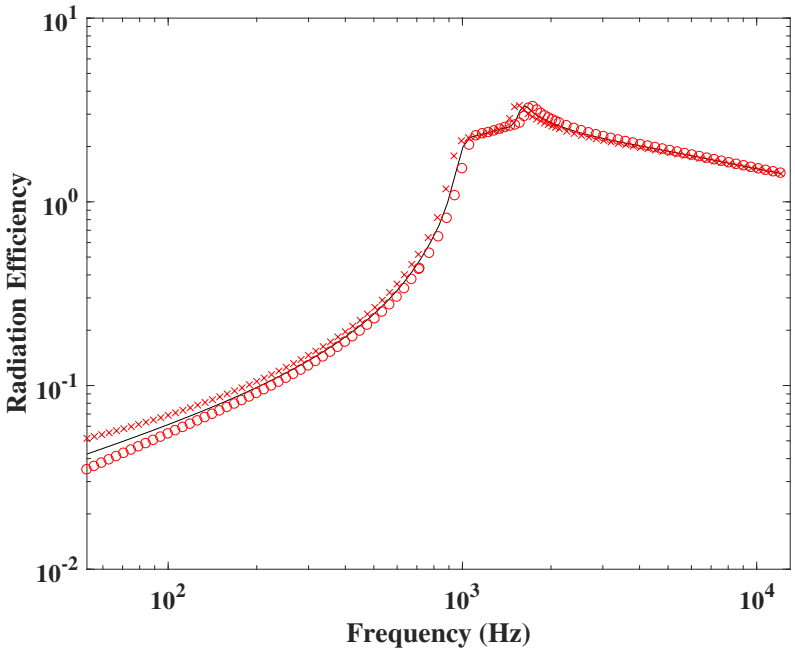


Figure 4.11: Comparison of the radiation efficiency of the sandwich plate: (-) non-stressed, (x) pre-stressed, tensile force $T = 100$ N in x direction, (o) pre-stressed, compressive force $T = -100$ N in x direction

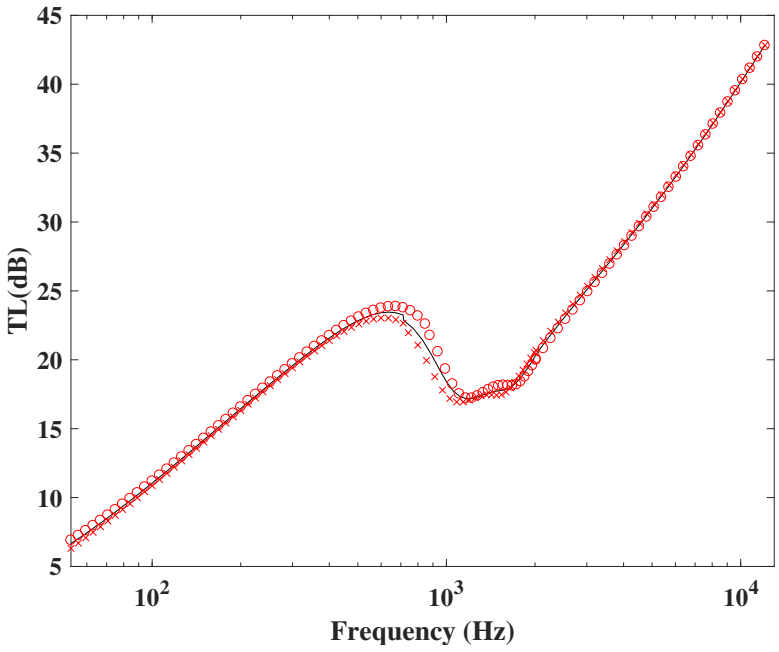


Figure 4.12: Comparison of the transmission loss of the sandwich plate: (-) non-stressed, (x) pre-stressed, tensile force $T = 100$ N in x direction, (o) pre-stressed, compressive force $T = -100$ N in x direction

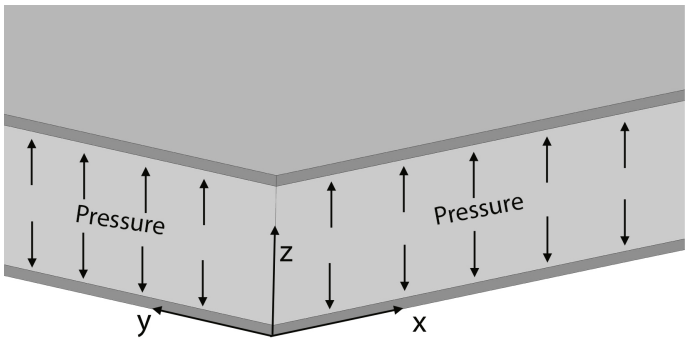


Figure 4.13: Representation of the internally pressurised sandwich laminate. As it is shown, the pressure is asked on the skins of the sandwich.

Internally pressurised

The second case of the sandwich laminate consists of internal pressure in the core, as it is shown in Fig. 4.13. Two different pressures, $p = 1$ MPa and $p = 10$ MPa are applied. It is noted that this load case is theoretical. In all the curves it can be seen that the first pressure scenario's results are quite close to the non-pressurised one's, as opposed to the second pressure scenario's ones. More specifically, in Fig. 4.14 the wavenumbers of the three scenarios are depicted. In this case, in low frequencies the wavenumbers of the high pressurised sandwich are significantly different than the low pressurised and the non-pressurised. The same behaviour is noticed in Fig. 4.15. Having Eq.(3.34) in mind, this behaviour can be explained, since when internal pressure is applied to the sandwich laminate's core, its strain energy is increased, thus the loss factor is decreased. Also, the pressure in the second pressure scenario is significantly higher, and so is the strain increase which leads to even lower loss factor. Another behaviour that is noticed is that in the higher-pressure scenario the loss factor remains lower than the non-pressurised all over the frequency range, with the difference diminishing as the frequency gets higher, though. In Fig. 4.16, 4.17 and 4.18, the same behaviour is noticed in modal density, radiation efficiency and TL dispersion curves. In these results it should also be noted that the higher pressure depicts different numerical results from the non-pressurised and the low-pressure scenario through almost the whole frequency range

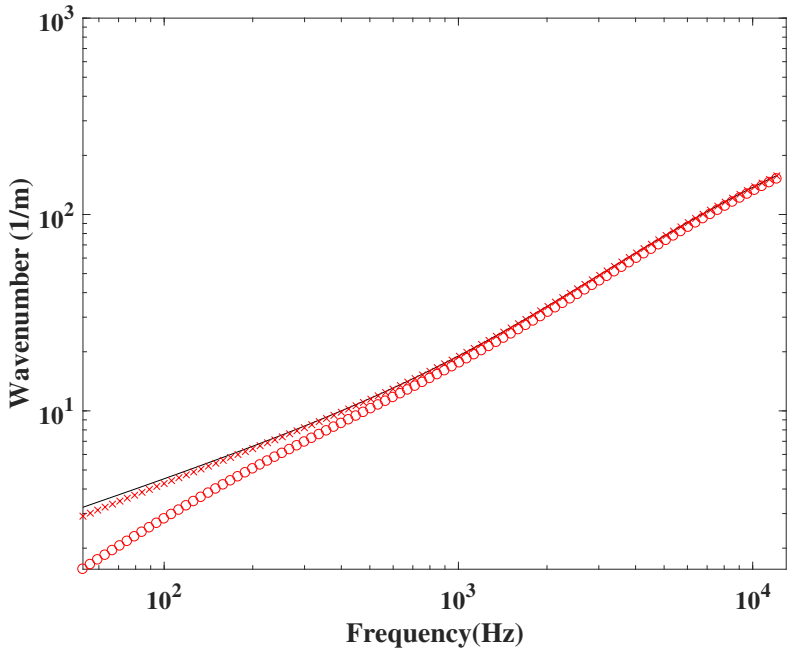


Figure 4.14: Comparison of the bending wavenumber (x-direction) of the sandwich plate: (-) non-pressurised, (x) pre-stressed, internal pressure $p =$ 1 MPa, (o) pre-stressed, internal pressure $p = 10$ MPa

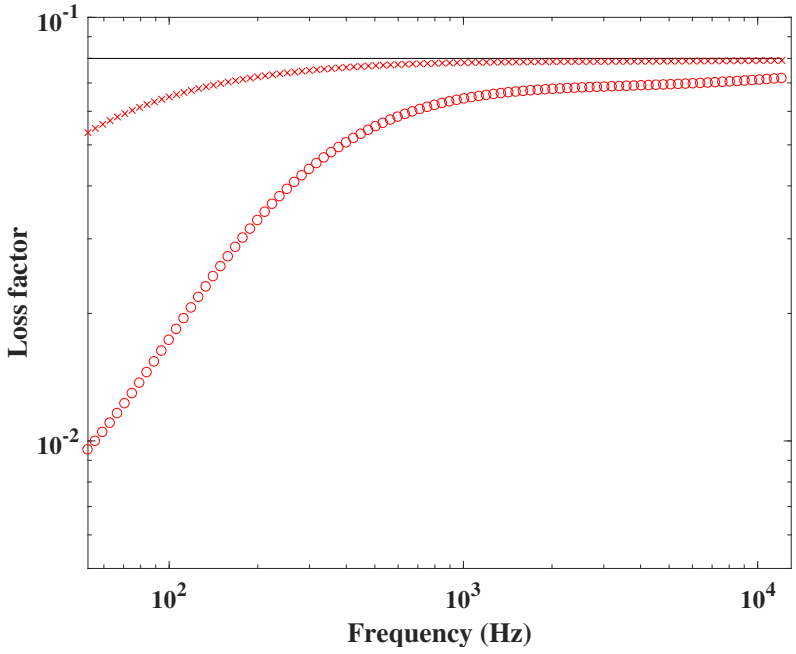


Figure 4.15: Comparison of the loss factor of the sandwich plate: (-) non-pressurised, (x) pre-stressed, internal pressure $p = 1$ MPa, (o) pre-stressed, internal pressure $p = 10$ MPa

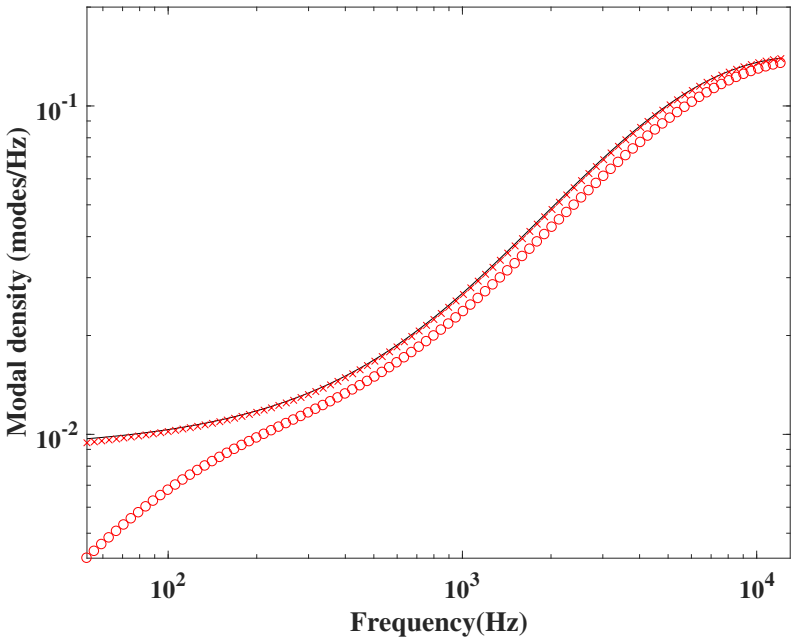


Figure 4.16: Comparison of the modal density of the sandwich plate: (-) non-pressurised, (x) pre-stressed, internal pressure $p = 1$ MPa, (o) pre-stressed, internal pressure $p = 10$ MPa

that is examined. This can be explained by the fact that the pressure seems to be quite high and the geometrical characteristics of the architecture are changed. It is noted that this load case is purely theoretical and no structural limitations are considered. Finally, in Fig. 4.19 and 4.20 the tensioned and pressurised results of the sandwich plate are compared. It can be seen that $p = 1$ MPa pressure and 100 N tensile force have almost identical effect on the loss factor and TL of the plate. More particularly, both scenarios' maximum TL reduction is ~ 2.8 dB (15%) and at the same frequency (~ 950 Hz), while pressurised sandwich's loss factor reduction is ~ 0.03 (33 %) and the tensioned one's is ~ 0.02 (21 %) at low frequencies. On the other hand, $p = 10$ MPa pressure affects largely both magnitudes. Concerning TL, the maximum decrease is ~ 10 dB (43 %) and it should be noted that it is observed at different frequency (~ 650 Hz) than the other two scenarios. As for the loss factor, the decrease is quite large, with ~ 0.07 (88%) being the largest one at low frequencies. This behaviour of the pressurised and tensioned sandwich laminates raises some concerns about

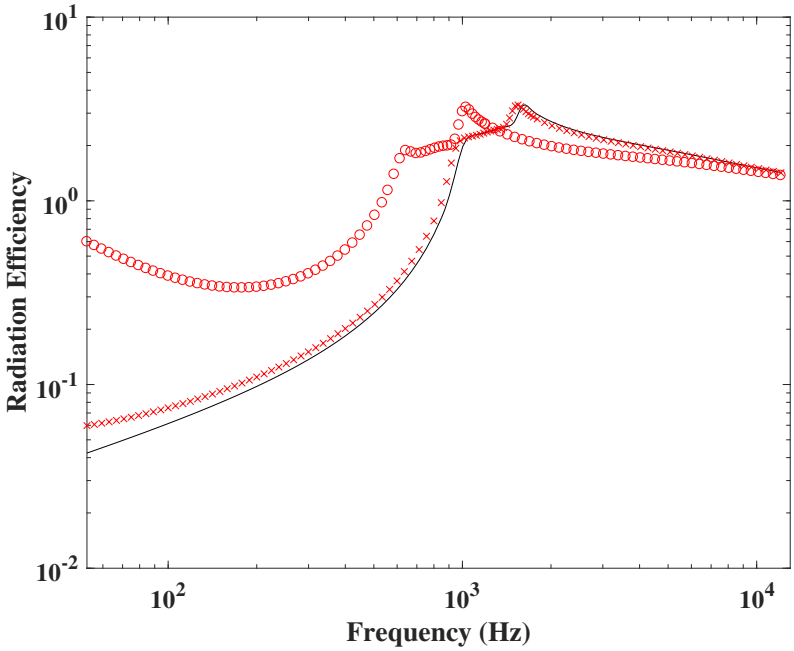


Figure 4.17: Comparison of the radiation efficiency of the sandwich plate: (-) non-pressurised, (x) pre-stressed, internal pressure $p = 1$ MPa, (o) pre-stressed, internal pressure $p = 10$ MPa

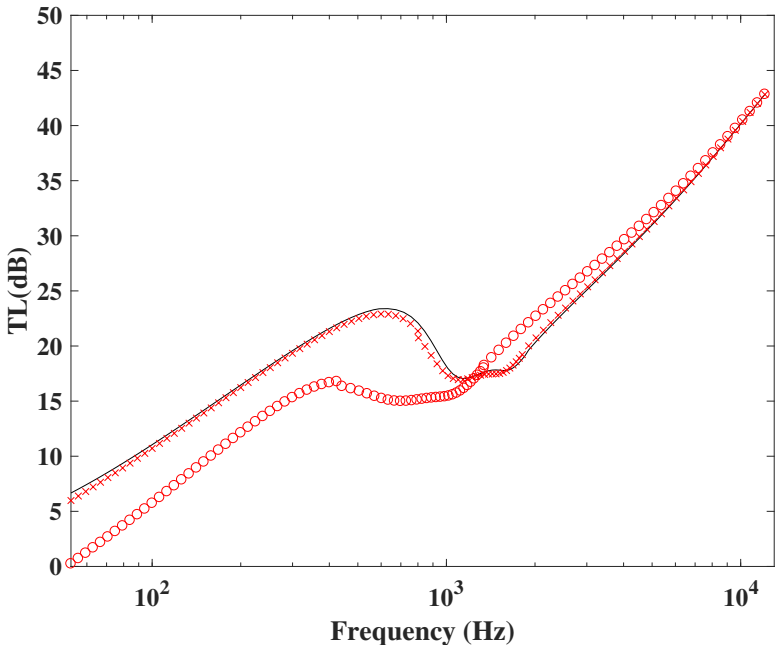


Figure 4.18: Comparison of the transmission loss of the sandwich plate: (-) non-pressurised, (x) pre-stressed, internal pressure $p = 1$ MPa, (o) pre-stressed, internal pressure $p = 10$ MPa

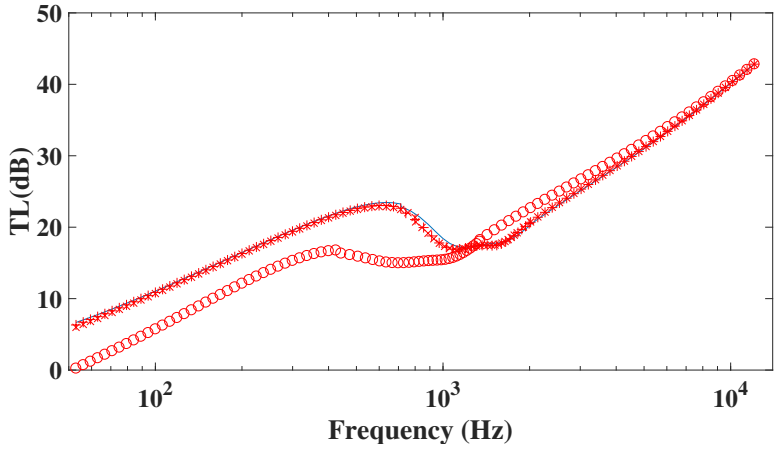


Figure 4.19: Comparison of the transmission loss of the sandwich plate: (-) non-stressed, (x) pre-stressed, internal pressure $p = 1$ MPa, (o) pre-stressed, internal pressure $p = 10$ MPa, (+) pre-stressed, tensile force T=100N

the vibroacoustic performance of pre-stressed structures which has not been widely examined. Another aspect that draws the attention is the fact that the high-pressure scenario demonstrates altered TL behaviour, where the coincidence controlled zone seems to have been moved.

4.3 Concluding remarks

The effect of pre-stress on the wave propagation and acoustic transmission properties of pressurised and pre-stressed composite structures is examined in this chapter. The monolithic laminate is examined in both tension and compression, while the sandwich laminate is examined in internal (core) pressure scenarios, too, along with the tension and compression ones. The loss factor and important SEA quantities are calculated, namely the modal density, the TL and the radiation efficiency of the panels following the calculation of their dispersion characteristics.

It is noticed that pre-stress affects the loss factor and the wave dispersion curves, which results in the alteration of the modal density, radiation efficiency and TL behaviour. The main conclusions that are drawn are listed below:

- It is shown that the tension and compression of the laminates alter the

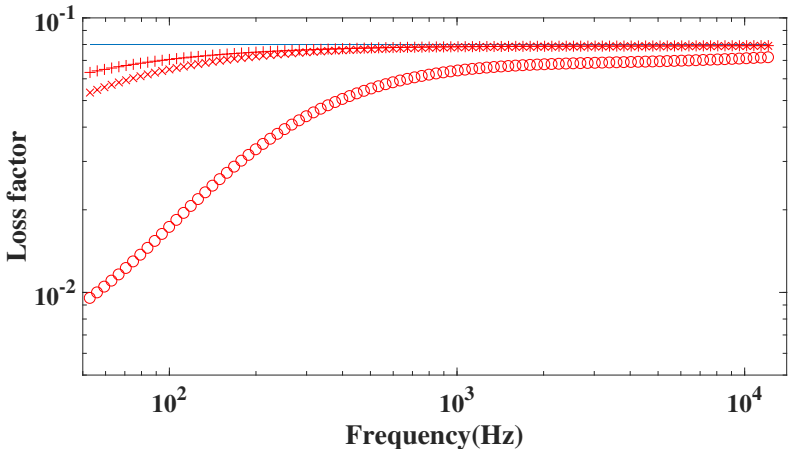


Figure 4.20: Comparison of the transmission loss of the sandwich plate: (-) non-stressed, (x) pre-stressed, internal pressure $p = 1$ MPa, (o) pre-stressed, internal pressure $p = 10$ MPa, (+) pre-stressed, tensile force $T = 100$ N

wave dispersion and loss factor in low frequencies, with the monolithic laminate case depicting more significant alterations in the results.

- In the internal core pressure of the sandwich, it is shown that if the pressure is high enough, quite significant alteration in vibroacoustic behaviour can be achieved, potentially in a wide range of frequencies.

These observations lead to the conclusion that it is of fundamental importance to take into consideration the effect of pre-stress during the design of a structure in order to achieve the vibration behaviour targets. This also means that the design can actually exploit this effect to enhance damping performance without any additional countermeasures. Additionally, pre-stress can consist of a way to actively control vibration performance using a loading electronic device [158].

Having developed the initial tools for the study of wave propagation in periodic structures, the focus of this work turned to band gap case studies. In the following chapter the band gap behaviour of non-structural and structural sandwich beams is examined.

Chapter 5: Banded behaviour of one-dimensional composite sandwich structures

5.1 Introduction

Sandwich structures are widely used today as a mean to achieve high stiffness to weight ratio. This useful characteristic renders the acoustic and vibration performance of these structure poor and unfavourable [45]. One way to overcome this poor performance is to take advantage of the band gap phenomenon. As it is known by the existing literature [23, 24] a change in the impedance of the structure is the cause of band gap behaviour, due to the wave reflection and cancellation of the propagating waves by the reflecting ones. This change, also called impedance mismatch, can be a stiffness or mass local inconsistency, where in case of periodic structure leads to vibration absorption and band gap behaviour. Having this in mind, in this chapter two case studies of sandwich beams which demonstrate band gap behaviour due to impedance mismatches are presented. For both case studies examined simple low-cost designs are under consideration, offering lightweight easy-to-manufacture solutions which can be incorporated in high-volume products.

5.2 Case study 1: Non-structural composite sandwich beams

The first case that is examined in this chapter consists of an infinite composite sandwich beam with periodically hollow core as shown in Fig. 5.1. The proposed core architecture consists of a non-structural solution, a prop-

erty that limits the range of its potential applications. Nevertheless, it consists of a very simple low-cost method to attenuate vibration in parts like interior vehicle trims with no extra cost, whether this is about mass or money. The mechanical characteristics of each material used in the models are listed in Table 5.1. In Fig. 5.2 z axis is depicted. ANSYS 14.0 is used during the FE modelling. Linear 8-node ANSYS SOLID45 solid element is chosen for the segment's meshing, which comprises of a 3D displacement field and three DOFs per node (translations in the x, y, and z directions) [148]. All three models have the same core thickness ($h_c = 10$ mm) and skin thickness ($h_s = 1$ mm) and four different ratios are tested ($Ratio = (hollow\ core\ length)/(cell\ length) = L_h/L_{b,x}$), along with homogenous core one ($Ratio = 0$) . The sandwich cell is $L_{b,x} = 16$ cm long and each element is $L_e = 1$ cm. The beam's width is 2 cm. The scenario of pressure on the skins of the structure in the hollow part of the core is also examined, as a continuity of the work with previous chapter.

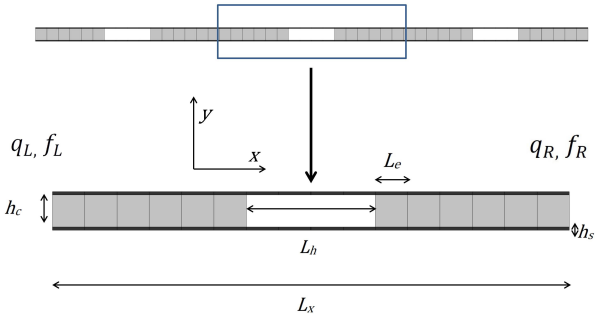


Figure 5.1: Infinite beam with periodic cell.

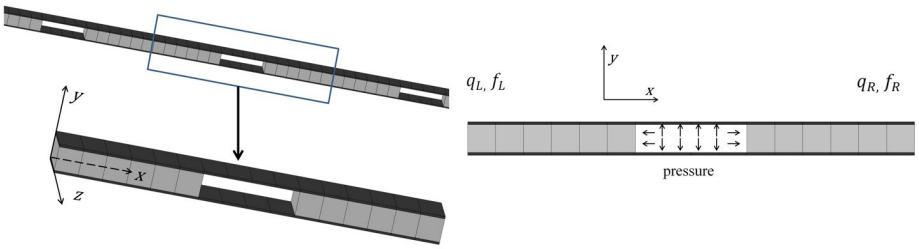


Figure 5.2: Left: Geometry of infinite beam. Right: Pressure applied in the hollow part of the core.

Table 5.1: Material properties

Material I	Material II
$\rho = 1\ 870\ \text{kg/m}^3$	$\rho = 110\ \text{kg/m}^3$
$E_x = 60e9$ Pa	$E_x = 145e6$ Pa
$E_y = 40e9$ Pa	$E_y = 145e6$ Pa
$E_z = 60e9$ Pa	$E_z = 145e6$ Pa
$\nu_{xy} = 0.4$	$\nu_{xy} = 0.45$
$\nu_{yz} = 0.4$	$\nu_{yz} = 0.45$
$\nu_{xz} = 0.25$	$\nu_{xz} = 0.45$
$G_{xy} = 1.2e9$ Pa	$G_{xy} = 50e6$ Pa
$G_{yz} = 1.2e9$ Pa	$G_{yz} = 50e6$ Pa
$G_{xz} = 3.6e9$ Pa	$G_{xz} = 50e6$ Pa

5.2.1 Results

In Fig. 5.3 and 5.4 the wavenumbers of all the ratios without any pressure applied are depicted. As it is expected ([10], [27] and [28]), banded behaviour is noticed on the graphs of the periodically hollow core beams. This can be explained by the hollow core part of the beam which acts as source of impedance mismatch which is responsible for the creation of band gaps. For the same reason it can be seen that the band gap frequencies change significantly as the ratio changes, since the source of the impedance mismatch alters characteristics. As the cause of the banded behaviour is the reflected waves due to the impedance mismatch that cancel the propagating ones, as the length of the hollow core changes, so the wavelength of these waves changes. This results in changes of the band gap frequency. It is worth noting that the third band gap of $Ratio = 2/8$ is significantly smaller than the other cases examined. Additionally, another aspect worth mentioning is the second band gap of $Ratio = 3/8$ and $4/8$, whose type seems to be of local resonance. An explanation is that the part of the core acts as resonator and we have coupled Bragg-scattering and local resonance band gaps, but it is out of scope of the current research. In Table 5.2 the results of the pressurised beams are presented. It should be noted that

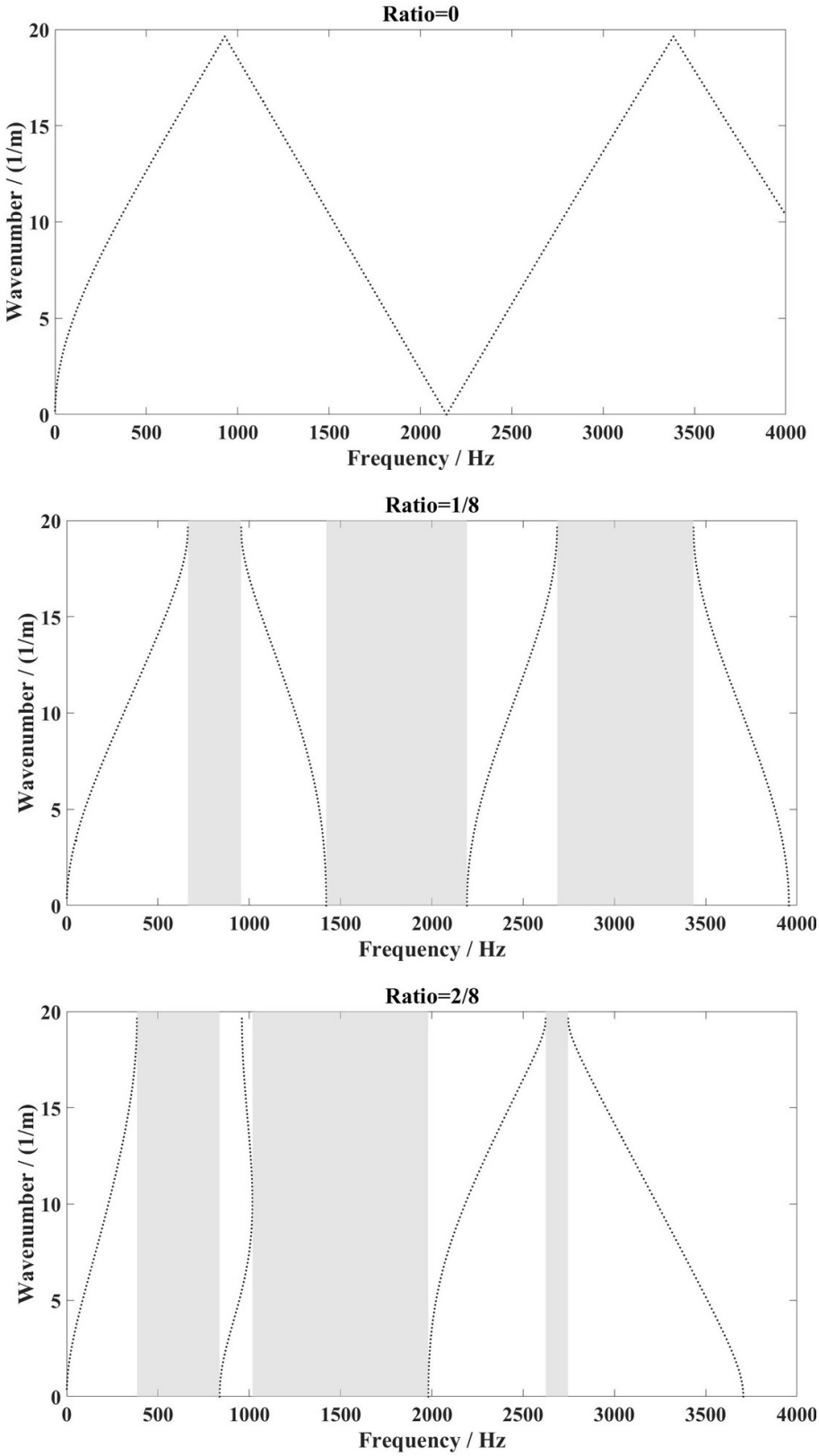


Figure 5.3: Graphs of the flexural waves of the first three *Ratios* with no pressure applied on the skins.

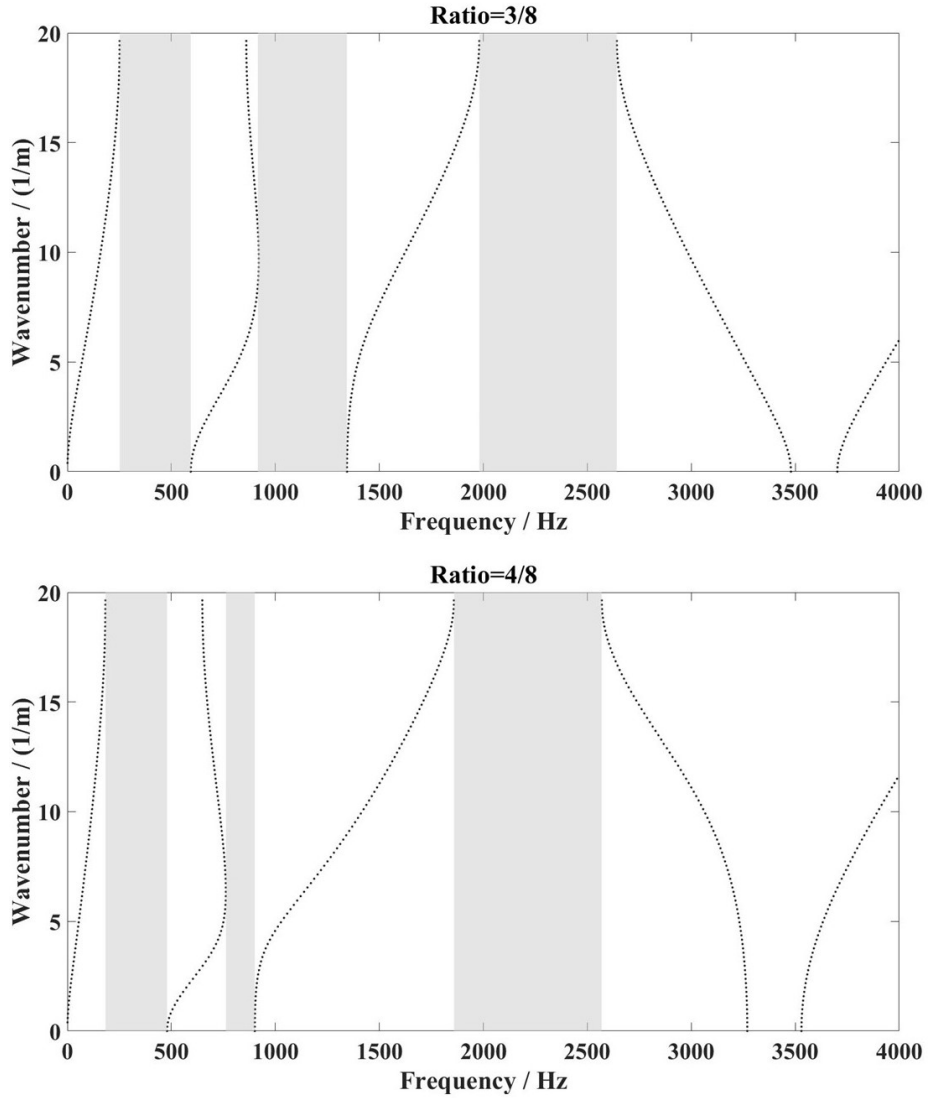


Figure 5.4: Graphs of the flexural waves of the last two *Ratios* with no pressure applied on the skins.

a structural integrity check is done using FE analysis for every examined situation so that to be sure that the beam can withstand the stress of the pressure applied on its skins. For this reason 1 MPa pressure is not examined for $Ratio = 1/2$ since it led to very high stress values. Going through the results it can be seen that pressure affects the band gap frequency in most of the cases, but it does not offer any significant control in the specific examined structure. Nevertheless, it is confirmed that pressure has effect on wave propagation as it is shown in Sec. 4, and on banded behaviour in this case, which might lead to practical applications in future research.

Additionally, further research might lead to stiffer and more durable materials which will increase the pressure capacity of the structure and hence potential band gap control.

Table 5.2: Band gaps frequencies, in Hz

	1^{st}	2^{nd}	3^{rd}
Ratio=1/8			
no pressure	$664.2 - 955.1$	$1422 - 2192$	$2687 - 3433$
$p = 10$ kPa	$664.2 - 955.1$	$1422 - 2192$	$2687 - 3433$
$p = 100$ kPa	$664.4 - 955.2$	$1422 - 2192$	$2687 - 3433$
$p = 1$ MPa	$665.6 - 956.2$	$1426 - 2194$	$2690 - 3436$
Ratio=1/4			
no pressure	$385.2 - 837$	$1018 - 1980$	$2624 - 2746$
$p = 10$ kPa	$385.2 - 837.2$	$1018 - 1980$	$2624 - 2746$
$p = 100$ kPa	$385.6 - 838.3$	$1018 - 1981$	$2624 - 2748$
$p = 1$ MPa	$388.5 - 849.7$	$1022 - 1987$	$2628 - 2759$
Ratio=3/8			
no pressure	$251.5 - 593.1$	$916.2 - 1344$	$1981 - 2642$
$p = 10$ kPa	$251.6 - 593.1$	$920.5 - 1344$	$1981 - 2642$
$p = 100$ kPa	$252.3 - 596.1$	$921.2 - 1346$	$1982 - 2643$
$p = 1$ MPa	$259 - 621.9$	$927.7 - 1358$	$1995 - 2652$
Ratio=1/2			
no pressure	$183.3 - 479.2$	$762.5 - 900.9$	$1859 - 2569$
$p = 10$ kPa	$184.8 - 481.9$	$763.8 - 902.6$	$1860 - 2572$
$p = 100$ kPa	$197.6 - 505.6$	$775.9 - 917.8$	$1871 - 2593$
$p = 1$ MPa	NA	NA	NA

5.2.2 Conclusion and further work

In this section a parametric study of frequency banded behaviour of an infinite periodic pressurised composite sandwich beam is examined. Both the length of the hollow part of the core and the pressure applied on its skins are considered as the parameters in the analyses. It is proven that the length of the hollow core plays a significant role in the wave propagation

and hence the frequencies of the band gaps. On the other hand, the pressurised beams do not have notable different banded behaviour concerning the flexural vibration that is the one examined in this work. Nevertheless, the behaviour pressurised beams exhibit allows the space for promising potentials as a method to actively control banded behaviour of structures and further research on the specific case is due.

The core-no core design demonstrated banded behaviour in all the different alternative designs that are modelled. Nevertheless, the examined beam cannot be considered as structural since there is no continuous part of the core to handle the shear loading of the two skins during bending. This observation leads to the next section, where two load-bearing composite sandwich beams are numerically and experimentally examined.

5.3 Case study 2: Mid-frequency band gap load-bearing composite sandwich structures with X-shaped and H-shaped cores

Having examined the core-no core solution, the potential of passive vibration cancellation through banded behaviour in sandwich structures is verified. Nevertheless, the under-study structure cannot be part of any load bearing mechanism, since the periodical absence of core does not offer consistent handling of the shear stresses between the two skins during any loading applied on the beam. Hence, the next step is to examine load bearing sandwich structure with banded behaviour. In this case study the two novel core schemes are examined, which demonstrate flexural band gap lower than 5 kHz, where the highest sensitivity of the human ear lies [159].

5.3.1 Proposed core architecture

The fundamental principle to save energy consumption and manufacturing cost is weight reduction. Additionally, the manufacturability of the structure must always be part of the design process in order to enable the

industrialisation of the design. Having these two principles in mind two one-dimensional cases are developed and numerically and experimentally examined in this section. Taking advantage of the unconventional geometry of the core, no additional mechanism is required avoiding extra mass. The work is based on lessons that were learnt in Sec. 5.2 where a simple design of a sandwich beam with periodically hollow core acting as band gap generator is employed. The core-no core design is simulated and parametrically examined, where it presented banded behaviour in all the different alternative designs that were modelled. Nevertheless, the examined beam could not be considered as structural since there is no continuous part of the core to handle the shear loading of the two skins during bending.

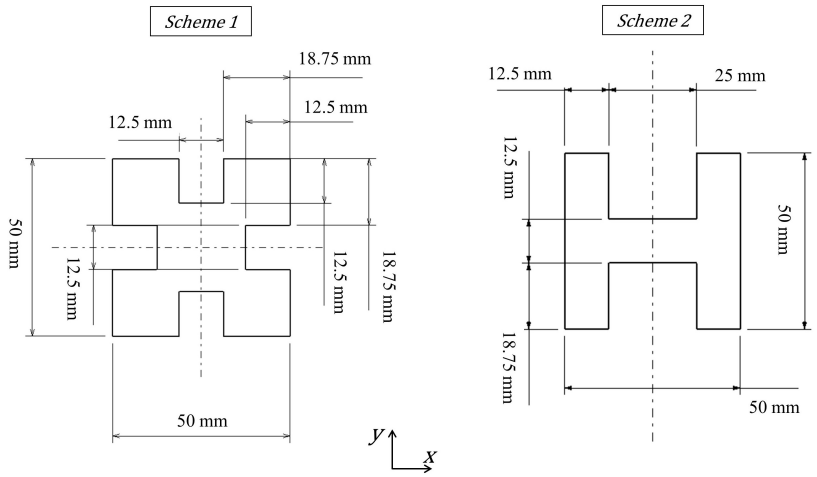


Figure 5.5: Geometry of the core of the scheme 1 and 2 unit cells.

Taking into consideration all the above, several alternatives are tested using the master script. All designs are conceived to combine core inconsistency in x-axis and structural integrity. Symmetry along both x- and y-axes is sought in line with manufacturability and the examined solutions follow the dimensions of the commercially available materials. The schemes that are presented here have part of their cores continuous along x axis, a characteristic which renders them load bearing elements of a structure. The load bearing part of the core in bending loads is shown in different shade in Figure 5.6. To compare the load bearing capacity of the two schemes with the respective solid core beams, a three-point-bending beam simulation is

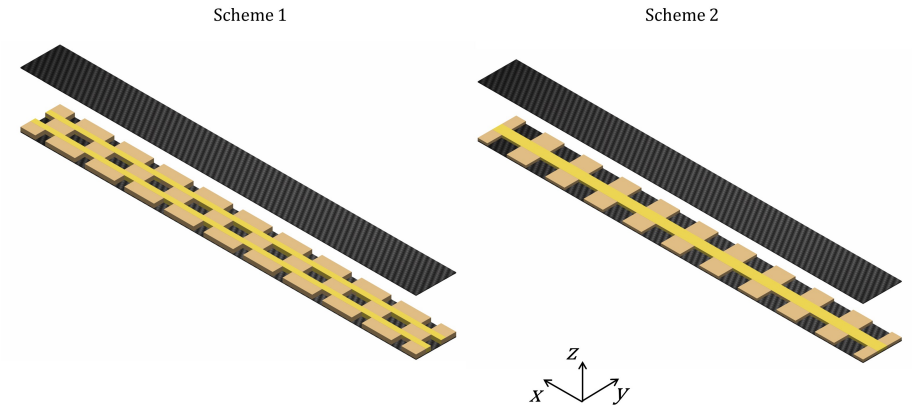


Figure 5.6: Skin and core of scheme 1 and 2 specimen.

Table 5.3: Material properties and Schemes characteristics.

Scheme 1	Scheme 2	Both Schemes
0.5 mm Skin, 5 mm Core	1 mm Skin, 3 mm Core	
Cured Carbon Fibre	Cured Carbon Fibre	PVC Foam
$\rho = 1\ 600\ \text{kg/m}^3$	$\rho = 1\ 420\ \text{kg/m}^3$	$\rho = 100\ \text{kg/m}^3$
$E_x = 50$ GPa	$E_x = 55$ GPa	$E = 75$ MPa
$E_y = 50$ GPa	$E_y = 50$ GPa	$G = 27.75$ MPa
$E_z = 20$ GPa	$E_z = 20$ GPa	$\eta = 4\%$
$\nu_{xy} = 0.4$	$\nu_{xy} = 0.4$	
$\nu_{yz} = 0.4$	$\nu_{yz} = 0.4$	
$\nu_{xz} = 0.25$	$\nu_{xz} = 0.25$	
$G_{xy} = 1.2$ GPa	$G_{xy} = 1.2$ GPa	
$G_{yz} = 1.2$ GPa	$G_{yz} = 1.2$ GPa	
$G_{xz} = 3.6$ GPa	$G_{xz} = 3.6$ GPa	
$\eta = 1\%$	$\eta = 1\%$	

considered using the FE models from Sec. 5.3.2. The setup can be seen in Fig. 5.7, where the beam is supported on both edges of one side and a force $F = 5$ N is applied on the opposite edge on the middle point. The bending

stiffness is then calculated using the equation:

$$k = F/\delta z, \tag{5.1}$$

where δz equals with the vertical displacement at the point of the force application. The results show that both schemes sacrifice a relatively small percentage of the original bending stiffness (see Table 5.4).

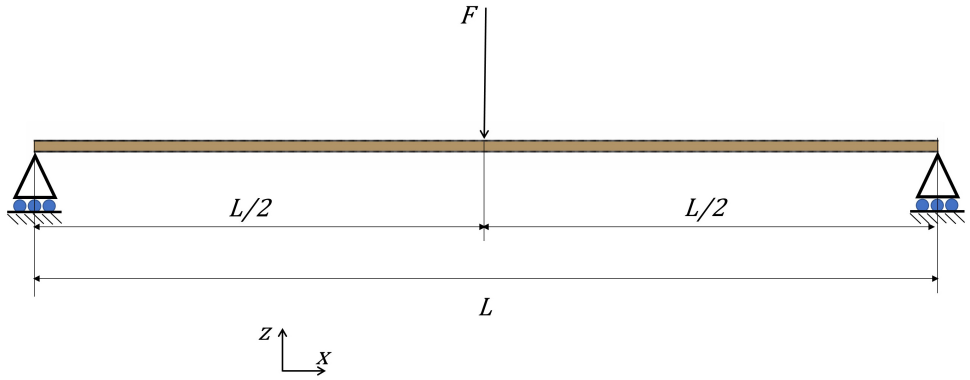


Figure 5.7: Schematic representation of the cantilever beam simulation used to compare bending stiffness.

Table 5.4: Bending stiffness.

	Scheme 1		Scheme 2	
	Proposed core	Solid core	Proposed core	Solid core
δz	0.479 mm	0.417 mm	0.335 mm	0.275 mm
Bending stiffness	10.44 kN/m	11.99 kN/m	14.93 kN/m	18.18 kN/m
Difference	12.94 %		17.91 %	

The core schemes can be easily manufactured using 2D automated cutting machine which puts no limitations to high-volume production. Both beams have carbon fibre as skin material and polyvinyl chloride (PVC) foam as core material with different geometrical characteristics in both skin and core, see Table 5.3. The geometry of both schemes' core architecture is depicted in Fig. 5.5. Both schemes' geometry is symmetrical along x and y axis and scheme 1 is along the diagonal, too. The two architectures can be used to incorporate internal resonators to enhance the vibration absorption

behaviour. Additionally, another aspect that could be examined is the active control of vibrations using the necessary smart elements in the hollow parts of the cores. Both concepts are out of the scope of this work and are considered part of the future work.

5.3.2 Experimental and numerical validation

Numerical analysis

A FE model of each unit cell is built for both schemes, and the results of the wave propagation analysis are compared with unit cells of continuous, solid core sandwich beams with the same material properties (Table 5.3). The model of scheme 1 unit cell is comprised of 176 elements, 48 of which are used to model the core, while the model of scheme 2 unit cell is comprised of 168 elements, 40 of which are used to model the core. In the case of the regular sandwich structure unit cell, the same number of elements are used for both of them (192 in total, 64 of which are used to model the core). In Fig. 5.8 and 5.9 the results of the wave propagation analysis are presented. As it can be seen in the graphs (shaded area), flexural band gap

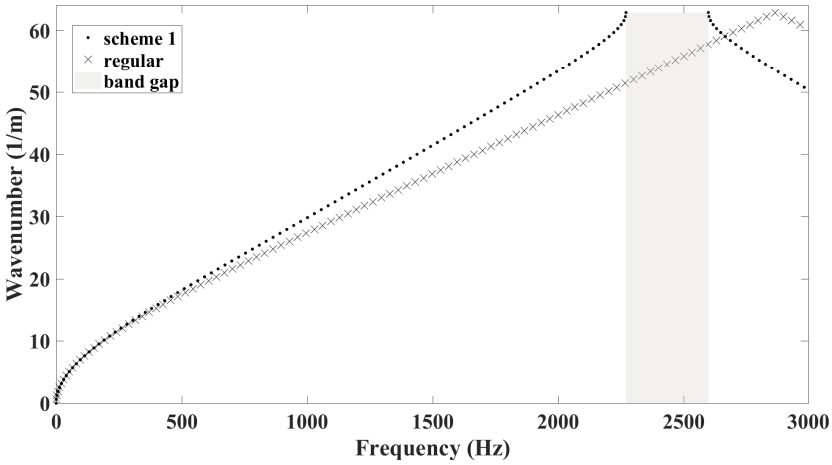


Figure 5.8: Flexural wave propagation of scheme 1 (.) and regular sandwich beam (x). The shaded area represents the bending band gap.

is observed at the frequency band 2 271 − 2 603 Hz for the scheme 1 and 1 701−2 299 Hz for the scheme 2. In order to examine the flexural behaviour

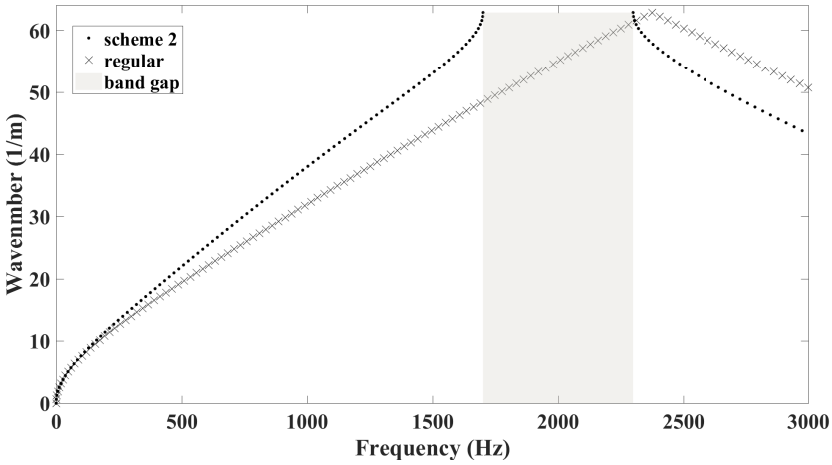


Figure 5.9: Flexural wave propagation of scheme 2 (.) and regular sandwich beam (x). The shaded area represents the bending band gap.

of both schemes 10-cell beams are tested using both FE method and a laser vibrometer and electrodynamic shaker setup to experimentally validate the FE analysis. The results are examined in the following paragraph.

FE and experimental results

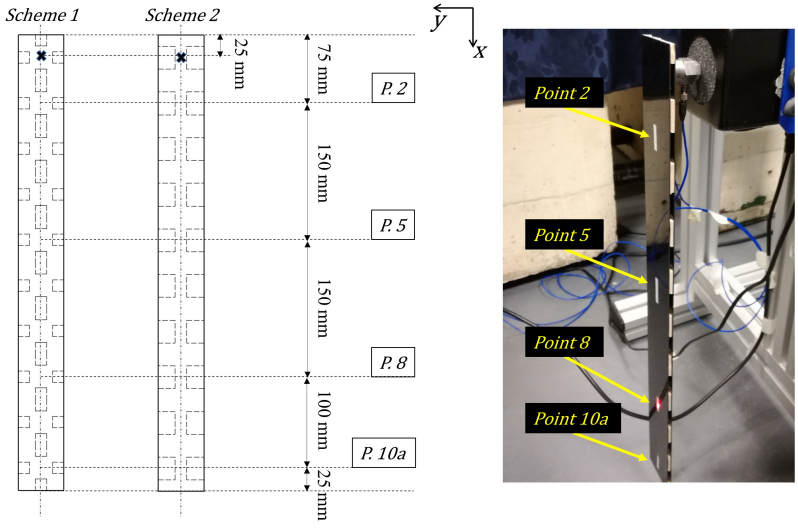


Figure 5.10: Left: The points that are examined in the experimental procedure and FE analyses. The point of excitation is marked as 'X'. Right: the points that are measured during the vibration experiment.

Following the same procedure as for the unit cells FE models, 10-cell FE models of both schemes and regular sandwich beams with the same materials are produced. The same number of elements per unit cell is used, so the model of scheme 1 beam is comprised of 1760 elements, 480 of which are used to model the core, while the model of scheme 2 beam is comprised of 1680 elements, 400 of which are used to model the core. In the case of the regular sandwich beam structures, the same number of elements are used for both of them (1920 in total, 640 of which are used to model the core).

The core schemes are manufactured using two PVC foam sheets which are cut in the specific geometries, as seen in Fig. 5.11. After shaping the core schemes, the carbon fibre stripes are cemented on both sides of them using a two-part epoxy adhesive (Permabond ET500). Concerning the experimental procedure the specimen is excited between 800 Hz and 3 000 Hz, since the experiment focused on the band gap region. The points where the acceleration is measured by the single point laser vibrometer can be seen in Fig. 5.10. The mounting point of the impedance head, hence the excitation point, is marked as 'X' in the same figure. The points' number is indicative of the unit cell's repetition.

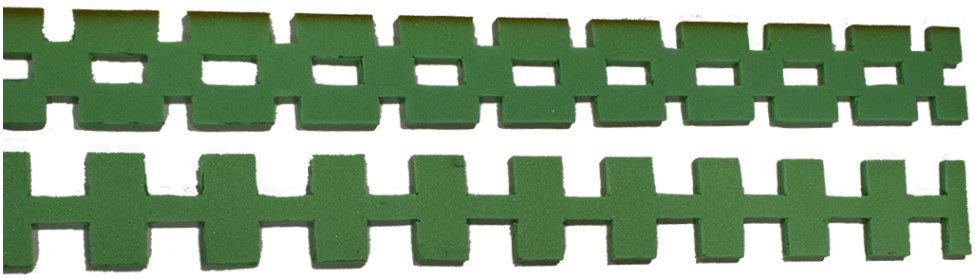


Figure 5.11: The two core schemes as manufactured. The cores are then cemented on cured carbon fibre sheets.

In Fig. 5.12 and 5.13 the FEA and experimental results of all the measured points of both schemes 1 and 2 are presented. Firstly and most importantly, it can be observed that in both cases experimental and FEA results correlate, with only some anomalies for the point 2 graphs which are explained by the fact that it is the closest to the excitation point. Figures 5.14 and

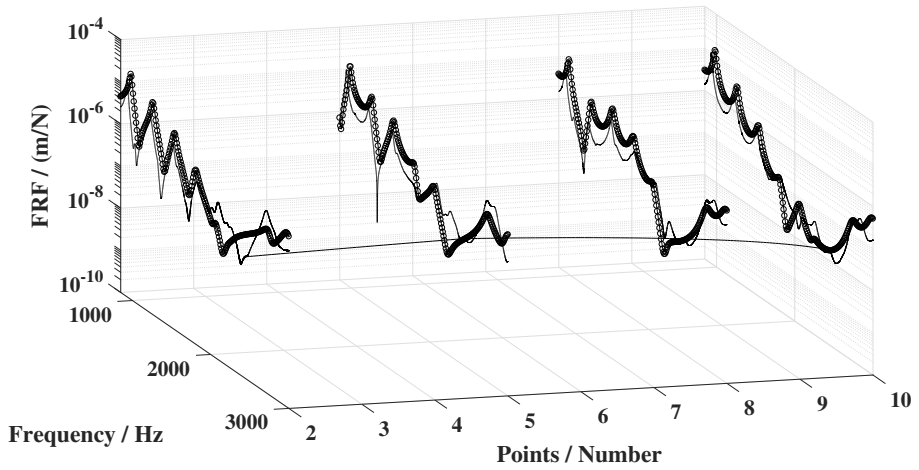


Figure 5.12: Frequency response function (FRF) of FEA (-o) and experimental results (–) of all the measured points of scheme 1. The points of the line connecting the FEA graphs consists of the middle value of the band gap.

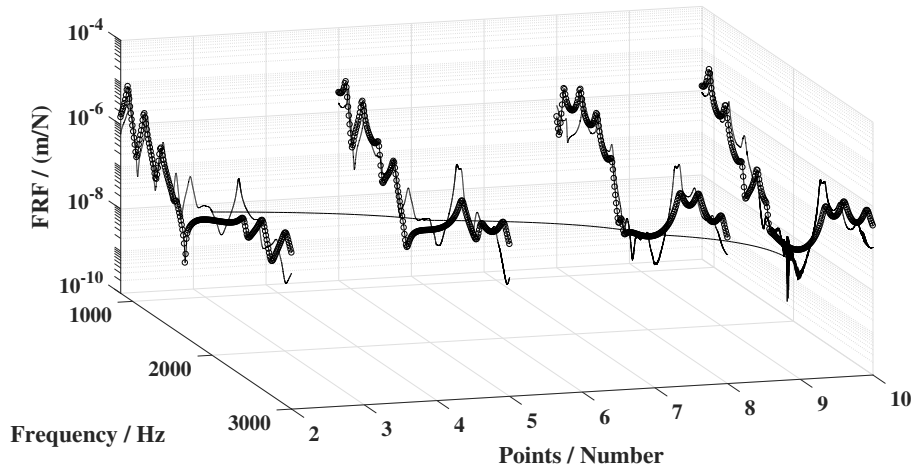


Figure 5.13: FRF of FEA (-o) and experimental results (–) of all the measured points of scheme 2. The points of the line connecting the FEA graphs consists of the middle value of the band gap.

5.15 exhibit the correlation of the experimental and FEA results, where the local divergence is less than 3 %. Secondly, both schemes 1 and 2 experiments demonstrate banded behaviour, as predicted in the numerical results in 5.3.2. The stop band is quite clear in the predicted frequency bands,

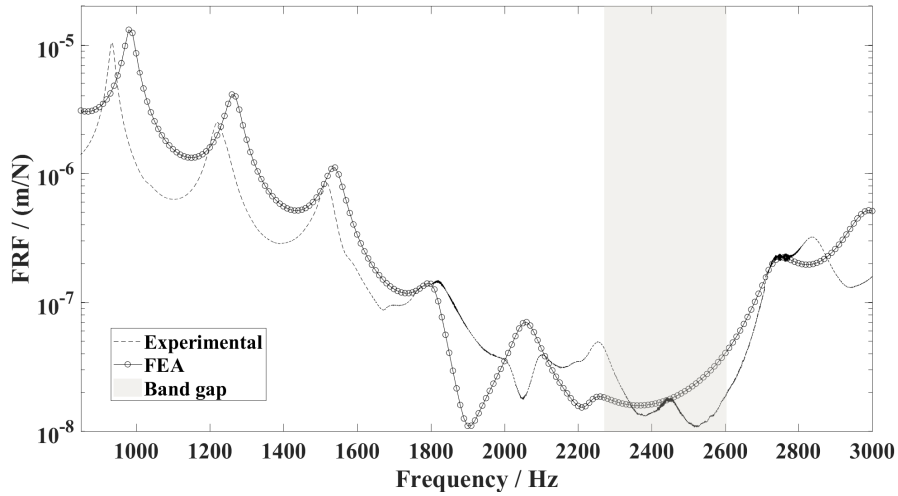


Figure 5.14: Scheme 1 experimental (–) and FEA (-o) results of point 10.

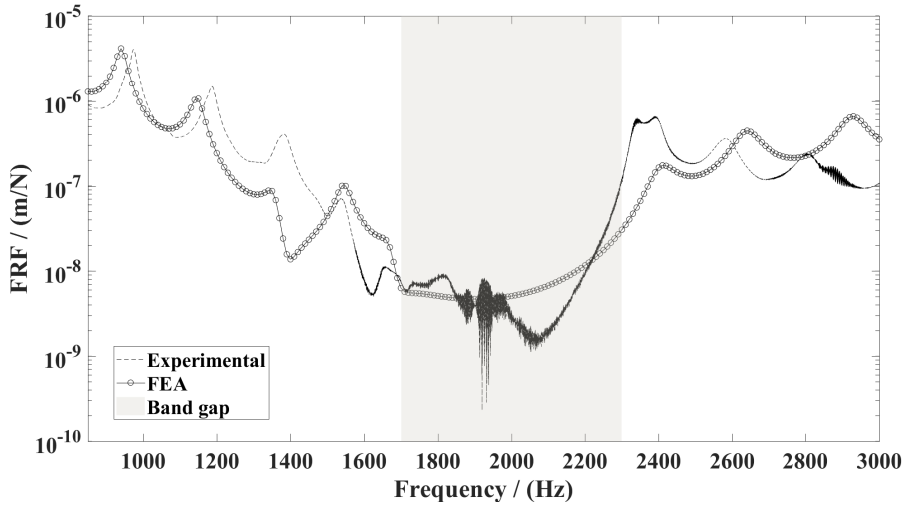


Figure 5.15: Scheme 2 experimental (–) and FEA (-o) results of point 10.

and the vibration absorption becomes more apparent as the point's number increase. This happens because as the wave propagates through the unit cells, it interacts with the reflective ones and weaken it. Therefore, the wave passes weakened through each unit cell and the amplitude loss adds up as it goes through the beam. Eventually it gets significantly weakened which is translated in absorption of the beam vibration. This observation coincides with the theory of band gap on periodic structures and it has been discussed in existing literature [2, 5]. It is noted that due to the large number of unit cells anti-node could not be avoided when measuring the response,

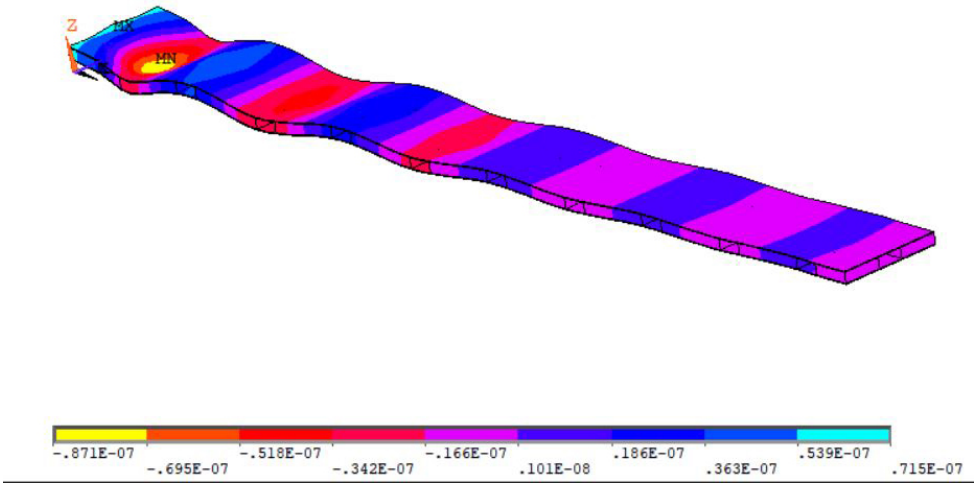


Figure 5.16: FEA of scheme 1 at 2430 Hz (displacements in meters).

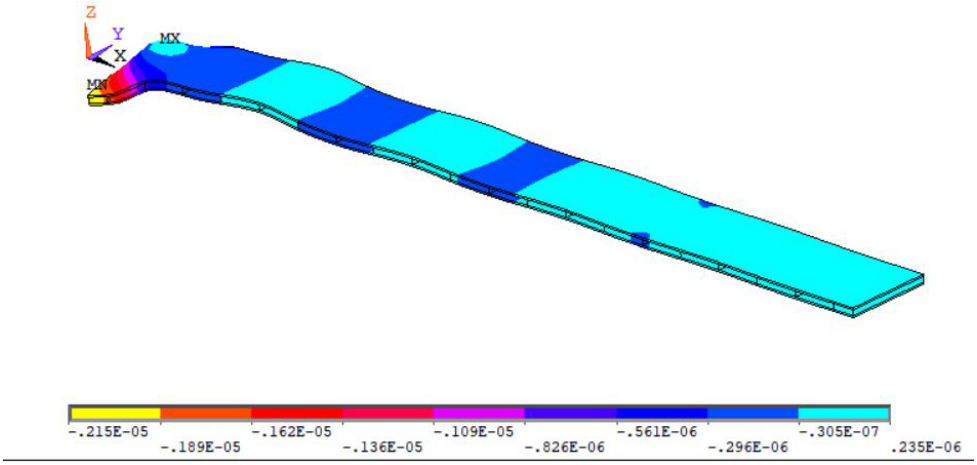


Figure 5.17: FEA of scheme 2 at 2000 Hz (displacements in meters).

as observed at $\sim$ 1.9 kHz and $\sim$ 1.4 kHz in Figures 5.14 and 5.15, respectively. In Fig. 5.16 and 5.17 the displacement profiles of schemes 1 and 2, respectively, are presented, where the aforementioned observation is graphically represented. This behaviour must be taken into consideration during the design of the application of the banded structure so that to achieve the optimum vibration isolation. Another issue that must be considered is the boundary conditions of the structure which will probably alter the banded behaviour. Furthermore, further work could concern the incorporation of local resonant structures in the parts of the core that are hollow, employing both band gap mechanisms.

5.4 Concluding remarks

In this section two novel core architectures able to induce wave stop bands while not being detrimental for structural bending stiffness are presented. The two designs are developed following weight reduction and manufacturability criteria to produce a low-cost and profitable solution. The main conclusions that are drawn are listed below:

- Firstly the numerical results of the wave propagation of the two core schemes demonstrate that both of the examined beams exhibit stop band of the flexural wave below 5 kHz. This low frequency stop band has not been observed in load-bearing structures without additional mass or significant compromise of structural integrity.

- Secondly, agreement is observed in the FE analysis and experimental results. This agreement validates the banded behaviour of the proposed core schemes.

The two schemes, hence, consist of a load bearing solution of passively annihilating vibrations in specific frequency bands.

In this part of the work the master script (see Sec. 3.3) is developed. This script allows the quick examination of the wave propagation of a periodic one- and two-dimensional structure. Having this script in function, the development of a multi-disciplinary optimisation algorithm is rendered possible. This algorithm and a case study examined using it is presented in the following chapter.

Chapter 6: Band gap behaviour of optimal one-dimensional composite structures with additive manufactured stiffener

6.1 Introduction

The script that is developed in the previous chapters offers the ability to examine the wave propagation of one- and two-dimensional structures time-efficiently. Nevertheless, in case the optimal solution is searched, the only way to acquire it is to examine as many cases as possible and compare the results of them. In Sec. (5.3) the geometry of the case study did not allow many alternatives, mainly because of the nature of the structure (constant core thickness allong x and y axis). Nevertheless, in case a more complex geometry is examined that method can be very time consuming and nearly non-feasible. This is why an automatic optimisation method needs to be used. This led to this chapter's work, where a gradient-based optimisation algorithm is developed and applied on the case study of a composite beam with AM stiffener.

The novelty of the work presented in this chapter is:

- An optimal design of a band gap structure is obtained, so that it serves both as a stiffener and band gap production mechanism, constituting a structural part.
- The optimal design of the structure is obtained by applying a developed computationally efficient unit cell based optimisation scheme.
- The developed multi-disciplinary design optimisation scheme uses scalar-

isation for simultaneous mass and vibration minimisation and static stiffness maximisation. Several starting points are used and parametric analysis is completed to evaluate the optimal solution.

More specifically, the multi-disciplinary optimisation of vibration attenuation through band gap and static structural performance of a one-dimensional composite structure with powder bed fusion of polyamide 12 (PA12) material additions is examined. As in the previous case studies, the structure is modelled using FE method and PST is used for predicting its wave propagation characteristics. A constrained non-linear optimisation method is used for the optimal geometric characteristics to be acquired. The optimal solution is realised using a powder bed fusion (laser sintering) method and is tested using the laser vibrometer and electrodynamic shaker setup to validate the FE model. The band gap behaviour of a thin composite beam

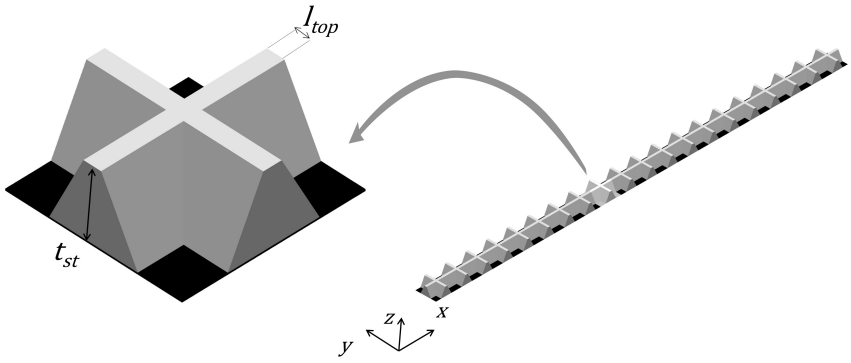


Figure 6.1: Schema of periodic beam and unit cell.

with AM stiffener is examined and optimised using the scheme described in Sec. 3.4. In this case, the Bragg scattering mechanism is targeted and the absolute band gap is examined. A thin plate of carbon fibre is used as a substrate structure and the stiffener is manufactured using the powder bed fusion method and PA12 material with an EOS Formiga P100 machine. The stiffener is cemented to the plate using a two-part epoxy adhesive (Permabond ET500). It is noted that the design under examination is used as a demonstration of the use of the methodology and it is not the only design

to exhibit band gap. The parameters that are examined are the thickness of the stiffener t_{st} and the length of the top of the wedge-like shape of the stiffener l_{top} (see Table 6.1 and Fig. 6.1). The mechanical properties of the materials are given in Table 6.2. Structural damping of both materials (loss factor η) is modelled. Since the host structure's characteristics are constant, only the stiffeners' design variables m and b_s are investigated.

Table 6.1: Case study optimisation variables and parameters.

Optimised variables	Parameters
Mass, m	Length of the top side, l_{top}
Bending stiffness, b_s	Thickness of the stiffener, t_{st}
Band gap's width, b_g	
Band gap's mid-point frequency, $b_g_{m_f}$	

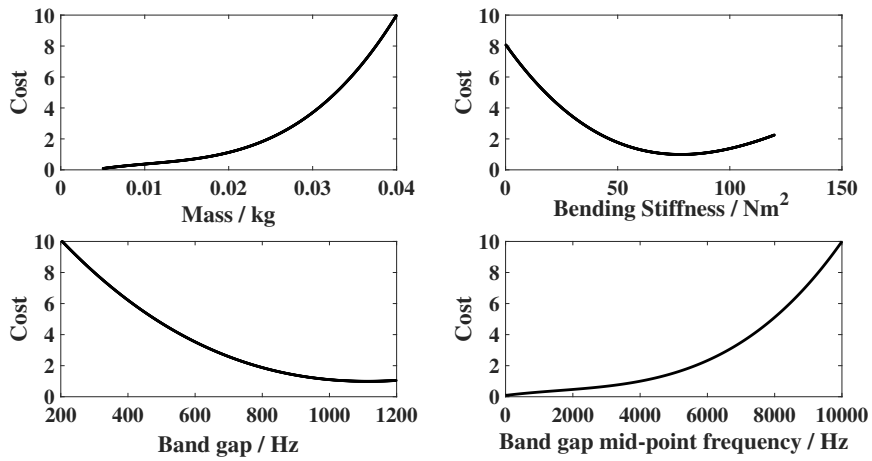


Figure 6.2: Cost functions used in the optimisation method.

6.2 Numerical results

The examined parameters are constrained such that $l_{top} \in [0.005\text{ m}, 0.025\text{ m}]$ and $t_{st} \in [0.005\text{ m}, 0.020\text{ m}]$. The calculations of $\frac{\partial b_s}{\partial \beta_i}$, $\frac{\partial m}{\partial \beta_i}$ need the equations that give b_s and m. For the calculation of the mass $m = m_{st}$ the formulas for volume calculation of a frustum of a pyramid and of a trapezoidal structure are used, so that $m_{st} = \rho_{PA12}(2V_{tr} - V_{fr})$, where $V_{tr} = L_x(l_{bot} + l_{top})\frac{t_{st}}{2}$

Table 6.2: Material properties

Cured Carbon Fibre	PA12
$\rho = 1\ 870$ kg/m^3	$\rho = 900$ kg/m^3
$E_x = 40$ GPa	$E = 1\ 600$ MPa
$E_y = 40$ GPa	$\nu = 0.3$
$E_z = 5$ GPa	$\eta = 4\%$
$\nu_{xy} = 0.4$	
$\nu_{yz} = 0.4$	
$\nu_{xz} = 0.25$	
$G_{xy} = 1.2$ GPa	
$G_{yz} = 1.2$ GPa	
$G_{xz} = 3.6$ GPa	
$\eta = 1\%$	

and $V_{fr} = \frac{t_{st}}{3}(B_1 + B_2 + \sqrt{B_1 B_2})$ (see Fig. 6.3 for labels, where B_1 and B_2 are the bottom and top areas of the frustum, respectively). The mass of the stiffener m_{st} and its partial derivatives in terms of the parameters, t_{st} and l_{top}, are calculated as follows:

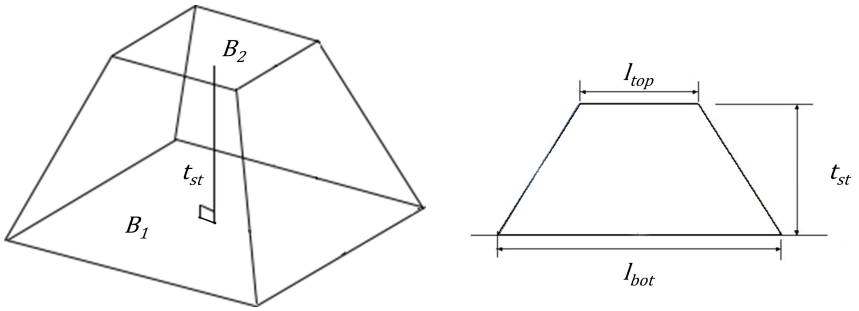


Figure 6.3: Pyramid frustum (left) and trapezoid (right).

$$m_{st} = t_{st}\rho_p[L_x(l_{top} + l_{bot}) - \frac{l_{bot}^2 + l_{top}^2 + l_{bot}l_{top}}{3}], \tag{6.1}$$

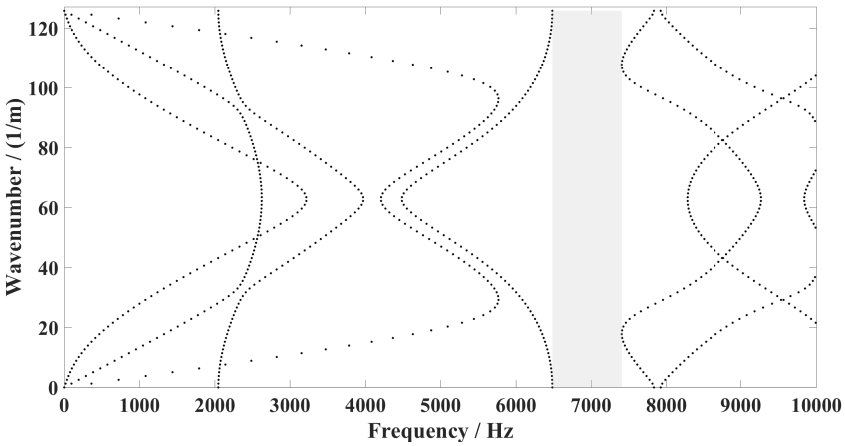


Figure 6.4: Wave numbers of the numerical analysis of the beam with geometric characteristics given by the optimal parameters. The shaded area represents the band gap.

$$\frac{\partial m_{st}}{\partial t_{st}} = \rho_p[L_x(l_{top} + l_{bot}) - \frac{l_{bot}^2 + l_{top}^2 + l_{bot}l_{top}}{3}], \tag{6.2}$$

$$\frac{\partial m_{st}}{\partial l_{top}} = \rho_p t_{st}[L_x - \frac{2l_{top} + l_{bot}}{3}]. \tag{6.3}$$

The bending stiffness of the stiffener b_s, along with its partial derivatives are given of the following equations:

$$b_s_{st} = E_p t_{st}^3 \frac{3l_{top} + l_{bot}}{12}, \tag{6.4}$$

$$\frac{\partial b_s}{\partial t_{st}} = E_p t_{st}^2 \frac{3l_{top} + l_{bot}}{4}, \quad \frac{\partial b_s}{\partial l_{top}} = \frac{E_p t_{st}^3}{4}. \tag{6.5}$$

The FE model of the unit cell consists of 468 8-node hexahedral elements (144 of which are used to model the carbon fibre strip and 324 the stiffener). The design cost functions employed to inform the relationship between $b_g, b_g_{m_f}, m$ and b_s and the induced design cost, are shown in Fig. 6.2. It is noted that the costs in these functions is a way to express the penalty of each outcome so that the objective function is generated according to these. The cost functions are based on the aim of a lightweight structural design with a wide band gap at low frequencies. The bending

stiffness cost curve is chosen bearing in mind that while large values of stiffness are desired, values that are too high may contradict the aims of the final design of the structure adding cost that can be avoided. Nevertheless, it should be noted that the main aim of this work is to provide an optimisation tool which can be adapted to different applications and the cost functions are arbitrarily chosen based on my experience. When the method is tailored for a specific application, the cost functions can be formulated by the designers accordingly. In this case, the cost functions chosen for the examined structure lead to the objective function (SI units are used during the optimisation):

$$\begin{aligned} F(\mathbf{p}) =& 3.167 \times 10^5 \times m^3 - 9.890 \times 10^3 \times m^2 + 1.503 \times 10^2 \times m - 0.4573 \\ & - 3.701 \times 10^{-6} \times b_s^3 + 1.743 \times 10^{-3} \times b_s^2 - 2.046 \times 10^{-1} \times b_s \\ & + 8.102 - 3.214 \times 10^{-9} \times b_g^3 + 1.870 \times 10^{-5} \times b_g^2 \\ & - 2.970 \times 10^{-2} \times b_g + 15.314 + 1.358 \times 10^{-11} \times b_g_{m_f}^3 \\ & - 6.296 \times 10^{-8} \times b_g_{m_f}^2 + 2.630 \times 10^{-4} \times b_g_{m_f} + 8.642 \times 10^{-2}, \end{aligned} \tag{6.6}$$

where the gradient of $F(\mathbf{p})$ is

$$\nabla F(\mathbf{p}) = \left\{ \frac{\partial F(\mathbf{p})}{\partial t_{st}} \frac{\partial F(\mathbf{p})}{\partial l_{top}} \right\}^T. \tag{6.7}$$

The optimisation is calculated using several starting points with steps of 2 mm and together with the parametric analysis results this is considered as the optimal design (see Fig. 6.6). The optimal values of the parameters are found to be: $l_{top} = 5$ mm and $t_{st} = 19.8$ mm, which gives: $b_g = 920$ Hz, $b_g_{m_f} = 6\ 950$ Hz, $m = 24.4$ g (of the unit cell of the stiffener) and $b_s = 44$ Nm^2 (of the stiffener). The propagating wave numbers for the optimal design are shown in Fig. 6.4, where the absolute band gap is observed.

6.3 Parametric analysis of the hybrid structure

A parametric analysis is performed to examine the effect of the two design

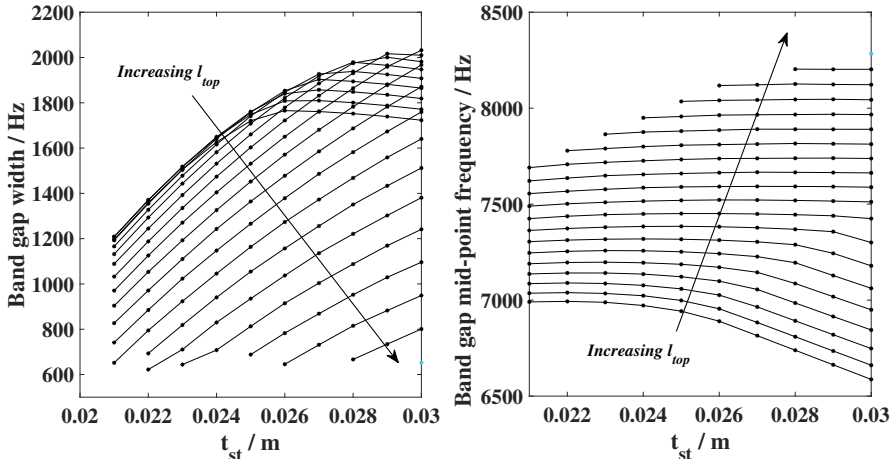


Figure 6.5: Parametric analysis results of further cases with t_{st} out of the optimisation limits, $t_{st} \in [0.021 \text{ m}, 0.030 \text{ m}]$ and $l_{top} \in [0.005 \text{ m}, 0.025 \text{ m}]$.

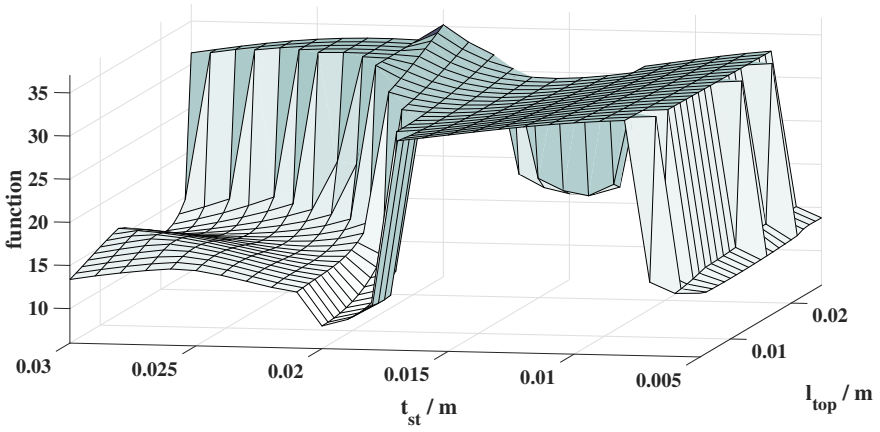


Figure 6.6: Objective function of the optimisation as calculated using the parametric analysis results ($t_{st} \in [0.005 \text{ m}, 0.030 \text{ m}]$ and $l_{top} \in [0.005 \text{ m}, 0.025 \text{ m}]$).

variables on the band gap behaviour of the structure. For this reason, several solutions are acquired between the optimisation procedure limits ($l_{top} \in [0.005 \text{ m}, 0.025 \text{ m}]$ and $t_{st} \in [0.005 \text{ m}, 0.020 \text{ m}]$), with a step of 0.001 m between the solutions. It is observed that between $t_{st} = 0.008$ m and $t_{st} = 0.017$ m, there is no significant band gap ($b_g < 200$ Hz). In view of this observation, a further parametric analysis is completed; this time examining design variables $t_{st} \in [0.021 \text{ m}, 0.030 \text{ m}]$ and $l_{top} \in [0.005 \text{ m}, 0.025 \text{ m}]$. In

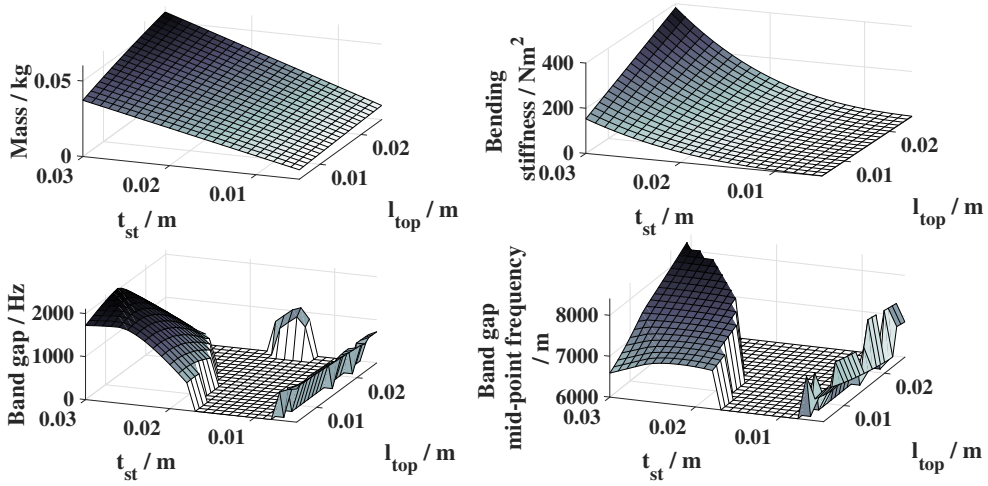


Figure 6.7: Relation of the optimised variables m, b_s, b_g and $b_g_{m_f}$ with regards to parameters t_{st} and l_{top} ($t_{st} \in [0.005 \text{ m}, 0.030 \text{ m}]$ and $l_{top} \in [0.005 \text{ m}, 0.025 \text{ m}]$).

Fig. 6.5, it is shown that for a given t_{st}, as l_{top} is increased, the band gap mid-point frequency is increased; however, the band gap width gets smaller. On the other hand, for a given l_{top}, it is seen that the band gap is increasing and its mid-point frequency is staying almost constant; but this behaviour changes after a specific value of t_{st} (which varies) and both band gap, and its mid-point frequency, decreases. Having acquired full solutions in parametric analysis, a graph of the cost function's values (Eq. (6.6)) is generated (see Fig. 6.6). It is observed that the result of the optimisation lies on the area that includes the global optimum. It is noted that the values of the objective functions that are larger than 20 are the cases for which a very narrow band gap is observed. This becomes apparent in Fig. 6.7, where the relations between the optimised variables m, b_s, b_g and $b_g_{m_f}$ with regards to parameters t_{st} and l_{top} are presented. In these graphs, it can also be observed that there are several combinations of t_{st} and l_{top} which lead to significantly wider band gaps at lower frequencies but with much higher mass, compromising the objective function outcome. This behaviour highlights the significance of the cost functions and the designers' input during the design of a structure which may aim for higher band gap without penalising the additional mass required. Furthermore,

additional options can be added to the methodology so that Pareto fronts are calculated, offering the designers numerous alternative solutions.

6.4 Finite element analysis and experimental results

FE harmonic analysis is undertaken using the same FE model as that for the unit cell of the wave propagation analysis and examining three different lengths of the hybrid beam. Previous research on bang gap behaviour of periodic structures has shown that the effect of the number of the unit cells must be considered. Jensen [2] showed analytically that the level of vibration attenuation depends on the number of unit cells; an effect that was also demonstrated experimentally elsewhere [5]. More specifically, it was shown that the band gap becomes more distinguishable (meaning the vibration attenuation is higher) as the number of unit cell repetitions increases. To check this behaviour in the specific case study, FE models with 468 8-node hexahedral elements per unit cell and for three different cases are examined: 5-cell, 10-cell and 15-cell beams. In Fig. 6.8, a representation of the simulation of the experiment for the 5-cell case is shown, where the excitation and response locations can be seen (no boundaries are applied). Similar conditions are used for the 10- and 15-cell case simulations, with the excitation force always applied on one edge of the carbon fibre strip and the response is measured on the top of the stiffener, on the other end. The results are shown in Fig. 6.9, where the effect of the number of the unit cells on the vibration attenuation of the band gap can be observed.

The geometry resulting from the optimisation process is manufactured and dynamically tested (Fig. 6.10) to validate the FE analysis results. A 5-cell beam is preferred, due to the limitation of the mass of the specimen that the shaker can excite and on the AM machine production size. It is noted that the experimental results do not include the band gap observation due to an insufficient number of the unit cells. The specimen is excited between 1 kHz and 8.5 kHz, using the experimental setup described in 3.5. The

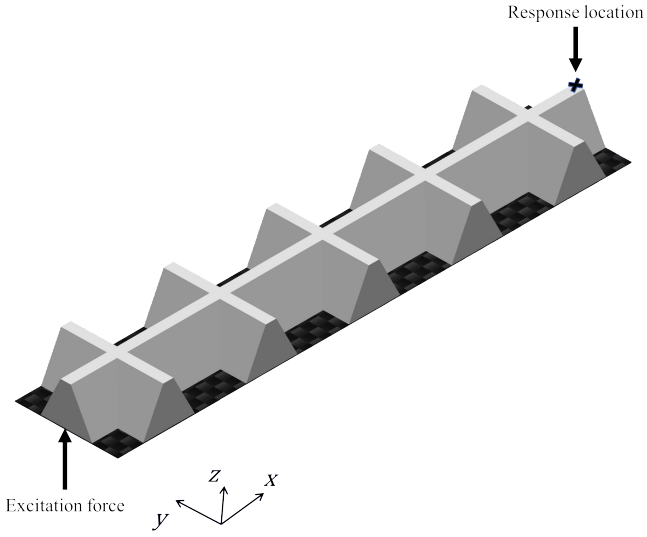


Figure 6.8: Representation of simulation of the experiment. The same logic is followed in all beam simulations, with the excitation force being asked always on the lowest, middle point of one edge and the response on the highest, middle point of the opposite edge.

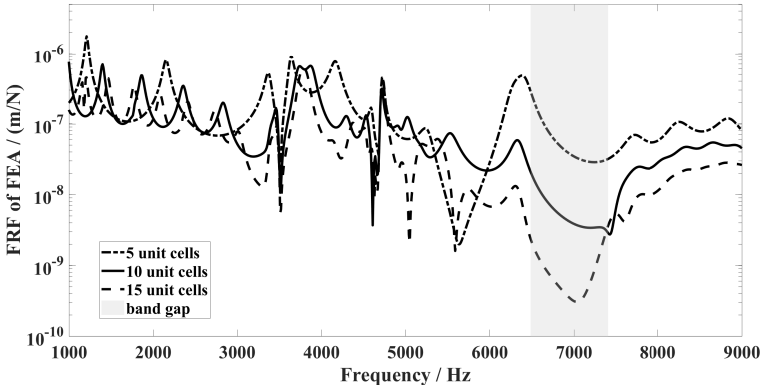


Figure 6.9: FRF of FEA of hybrid composite beam with: (-.) 5 unit cells, (–) 10 unit cells, (- -) 15 unit cells. The shaded area represents the numerically calculated band gap.

points where the single point laser vibrometer measured the response can be seen in Fig. 6.11. As can be seen in the same figure the points' number is indicative of the unit cell's repetition.

In Fig. 6.12 to Fig. 6.14, the results for several points along x-axis are shown. The FRF graphs of the experimental and FE results of the three

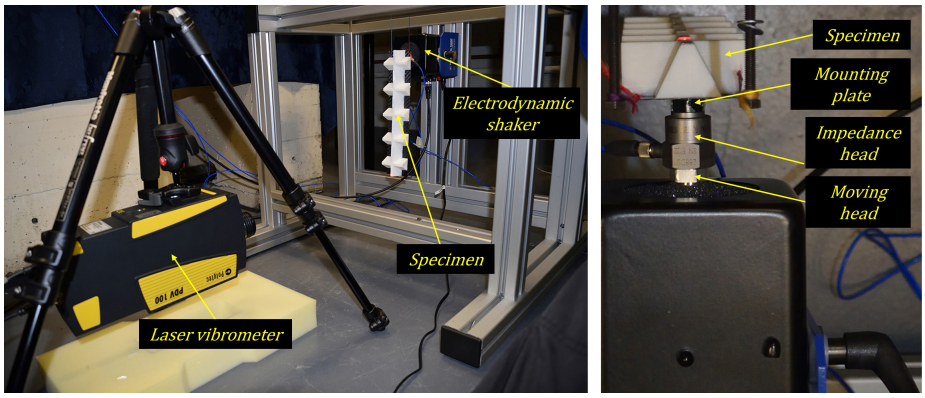


Figure 6.10: Experimental setup of the vibration testing. The setup is specifically designed and manufactured to accomodate small specimens for vibration testing.

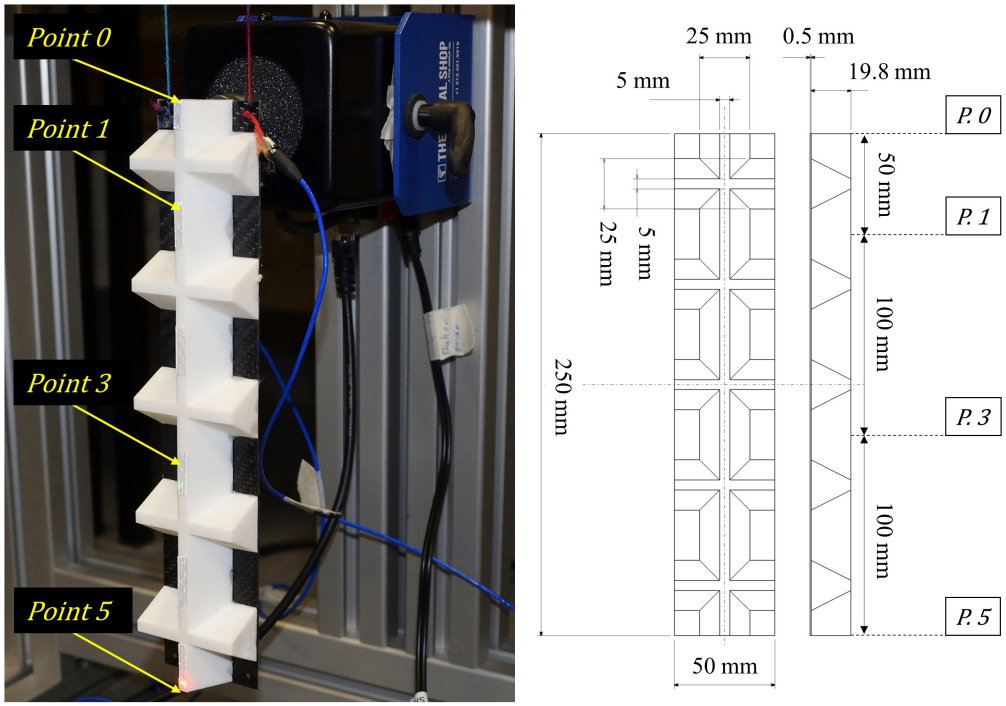


Figure 6.11: The points at which the FRF graphs are presented. Each point's number is indicative of the number of the unit cells.

points show convergence, with minor deviations in some high frequency resonant modes. Point 1 (Fig. 6.12) has the most significant deviations, while point 3 (Fig. 6.13) and point 5 (Fig. 6.14) exhibit better convergence with the FE results. The highlight of the experimental results is the absence of resonant modes in the calculated band gap area, as it is expected from a

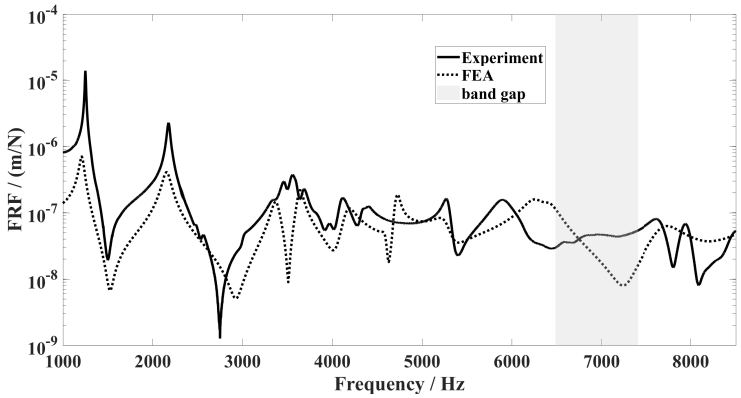


Figure 6.12: Experimental and FEA results of the FRF of point 1 where (–) is FRF of experimental results and (- -) is the FEA results.

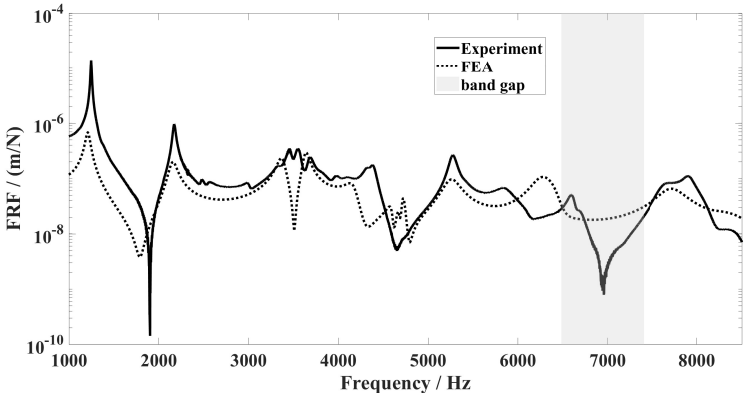


Figure 6.13: Experimental and FEA results of the FRF of point 3 where (–) is FRF of experimental results and (- -) is the FEA results.

band gap structure. Nevertheless, as discussed above, 5 cells are not enough to make the vibration attenuation distinguishable in this frequency band.

6.5 Concluding remarks

In this work, an efficient multi-objective scheme using scalarisation is presented for optimising the static, dynamic and mass characteristics of a one-dimensional composite structure having an additive manufactured stiffener. Additionally, an experimental evaluation of the FE model of the case study is presented. The presented computational scheme gives the ability to adapt the optimisation criteria to specific applications. Furthermore, a parametric

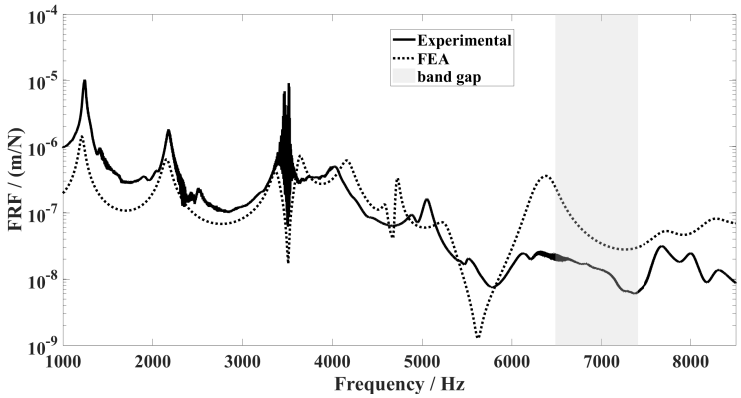


Figure 6.14: Experimental and FEA results of the FRF of point 5 where (–) is FRF of experimental results and (- -) is the FEA results..

analysis is completed offering a valuable insight of the stop band behaviour of the structure with regards to the parameters.

Chapter 7: Conclusions and Future Work

7.1 Conclusions

The main aim of this work is to examine the potential of band gap application on easy-to-manufacture load-bearing structures. In order to thoroughly examine this case, three main steps are taken with each one of them addressing slightly different subject. Nevertheless, each step consists of a continuation of the previous one, with all three of them contributing to the main aim. More details are presented below.

- In Chapter 4 the initial methodology tools are developed and used to calculate the effect of the pre-stress and pressure on the vibroacoustic behaviour of monolithic and sandwich composite structures. It is proven that pre-tension and pre-compression of both monolithic and sandwich laminates affect significantly the damping and acoustic behaviour, with the results being more obvious in the former occasion. The same is proven for the internally pressurised sandwich structure, too. All these conclusions are very useful since pressurised and pre-stressed structures are met in the most cases of structures (pressure vessel, aircraft wings etc.) and it is important to include these parameters during the design to achieve the targets. It is also shown that WFEM is a quick, reliable way to examine the vibroacoustic behaviour of pre-stressed structures.

- In Chapter 5 the banded behaviour of two different case studies of sandwich structures are examined. The first section consists of sandwich composite beams with periodically hollow cores, which demonstrates banded behaviour in low frequencies (below 1 kHz). It is shown that by designing sandwich with simply periodically hollow core can

produce banded behaviour without the need of additional mechanism. Nevertheless, this type of beam cannot be utilised in structural parts, a realisation which leads to the second section of the chapter.

- In the second section of the same chapter, two novel core architectures of load-bearing composite sandwich beams are examined. In this part of the work the experimental setup is designed, manufactured and used for the examination of the vibroacoustic response of the beams. It is proven, both numerically and experimentally, that the examined schemes consist of structural solutions with banded behaviour in frequencies less than 5 kHz, where the human ear sensitivity peaks. This is a significant conclusion, since passive vibration annihilation is achieved on a load-bearing composite beam without the use of any additional mechanism which increases the structure's mass and complexity. Additionally, the proposed core architecture can be easily manufactured using a two-dimensional automated cutting machine.

- In the same section the master script is developed (see 3.3) which allows the user to examine a complex periodic structure quickly using a unit-cell-based scheme. This automated algorithm is used to develop an optimisation algorithm used in the following chapter.

- Staying on the structural parts, in Chapter 6 a multi-disciplinary optimisation algorithm using scalarisation is developed. The algorithm obtains the optimal solution by using the computationally efficient unit-cell-based optimisation scheme and can optimise the dynamic, static and mass characteristics of a structure. In this work it is used on a composite beam with additive manufactured stiffener, the vibration behaviour of which is also experimentally verified. The main advantage of the algorithm is that it can be adapted to the needs of the design targets of any application, since the cost functions that dictate the optimisation procedure and results are easy to edit accordingly.

7.2 Contribution to knowledge and potential industrial applications

As a continuation of the previous section, the contributions to knowledge and potential industrial applications of the work of each chapter is presented here, along with their limitations.

- In Chapter 4 the work examines the vibroacoustic behaviour of pre-stressed structures, namely tension/compression and internal pressure. These scenarios are quite common in real life where pre-stressed structures or parts of structures are met, such as on an airplane or wind turbines. Hence it is important to predict the effect of the stresses on the vibroacoustic behaviour in order to achieve the optimum design concerning product life, mass and cost. The work is limited to two-dimensional case studies without the effect of boundary conditions, though, with further development of the method needed to capture more complicated geometries. Additionally, the work is purely theoretical with the existing material properties limiting the potential of application of internal pressure of that magnitude.

- In Chapter 5 the focus is shifted to sandwich structures with band gap behaviour. As mentioned in 2.6 sandwich architectures are used vastly in aerospace, automotive and civil engineering, whether they consist part of the load-bearing structure or just decorative function. This is why in the first part of this chapter the case study consists of non-structural architecture of sandwich with numerous stop bands, which can be very useful for applications where stiffness is not required, such as cover panels, floor panels etc. This limitation is not applicable in the second part of the chapter where structural schemes of sandwich structures with banded behaviour are examined. These solutions can be part of load-bearing frames where vibration isolation of bending loads is needed. Nevertheless, in order to use them in parts where vibration is handled there is the need of examination of the response

to fatigue loads and cycle life. Additionally, the same limitation with the first chapter concerning boundary conditions effect is met, along with the fact that here the work is limited to one dimension.

- Chapter 6 presents an optimisation method of banded behaviour of structural parts , where the existing work is non-existent. The industrial application of this methodology is not limited in specific sectors, as the engineers are given the freedom to apply their own requirements by forming the cost functions according to their wills. Additionally, for the same reason the methodology is not limited to specific frequency bands, band gap mechanisms or even materials/geometries. Nevertheless, there is one important limitation which is the one that holds the examined geometry to specific geometrical limits and does not provide several solutions and their optimal results, as mentioned in the next section. Additionally, as above, the work is limited to one dimension and free-free case study.

7.3 Future work

In each part of this study further work can be done so that to reach the next level of research.

- In Chapter 4 the finding that both pre-stress and pressure affect the vibroacoustic behaviour of composite structures is very significant. WFEM could be used in real-life case scenarios where periodic structures are met, like an airplane wing or a pressure vessel, to simulate the pre-stressed behaviour of the whole structure. This way pre-stress can be used as a mean to achieve the same damping target with less weight. Also, this effect of pressure and pre-stress can be used as active vibration control method. Additionally, high pressures seem to alter significantly the vibroacoustic behaviour which can be used in the future where stronger materials will be available.

- In Chapter 5, both case studies show that band gaps can be achieved

using unconventional core architectures. For both cases the obvious further work that can be done is to examine the potential of the same or similar solution in two-dimensional structures. In the first case study it is also shown that pressure slightly alters the frequency stop band, which means that with a different geometry or stronger materials pressure can be a means of control of banded behaviour. Furthermore, since in both case studies there are hollow core parts, these can be taken advantage to incorporate additional band gap mechanisms, e.g. internal resonators.

- In Chapter 6 the most apparent further work is to apply the algorithm in two-dimensional case studies, too. In addition to that, the nature of the algorithm is that so it can be tuned to calculate additional characteristics of the examined structure, such as acoustic and damping performance (STL, loss factor etc.). Furthermore, since as it is observed in the parametric analysis, there are several results and parameters combinations which might consist of a desired solution according to the specific needs of the application. Hence, a useful tool which would give the engineer the total number of these solutions (e.g. Pareto fronts) could consist one of the next steps. Additionally, the software could be possible to examine a family of several initial solutions and generate their optimal results.

Collectively, the work that is on the banded behaviour of the structures deals with one-dimensional solutions. One major step to bring this research a step forward is to examine two-dimensional solutions and even curved or other geometries, with no limits. This can lead to an integrated software package which, along with a design package, could focus on the examination and development of structures demonstrating banded behaviour. This will dictate the adaptation of the method to simulate finite structures and curved two-dimensional solutions.

In conclusion, the band gap structures are continually gaining increasing interest among the researchers and engineers and lately industrial applications are designed. Therefore, further decisive steps have to be taken

towards solutions that can be used by a wide number of industry sectors.

Bibliography

[1] D. Thorby, *Structural dynamics and vibration in practice : an engineering handbook*. Elsevier/Butterworth-Heinemann, 2008.

[2] J. S. Jensen, "Phononic band gaps and vibrations in one- and two-dimensional mass–spring structures," *Journal of Sound and Vibration*, vol. 266, no. 5, pp. 1053–1078, 2003.

[3] A. Peiffer, "Full frequency vibro-acoustic simulation in the aeronautics industry," in *ISMA2016*, (Leuven), 2016.

[4] B. R. Mace, D. Duhamel, M. J. Brennan, and L. Hinke, "Finite element prediction of wave motion in structural waveguides," *Acoustical Society of America*, vol. 117, no. 5, pp. 2835–2843, 2005.

[5] P. G. Domadiya, E. Manconi, M. Vanali, L. V. Andersen, and A. Ricci, "Numerical and experimental investigation of stop-bands in finite and infinite periodic one-dimensional structures," *Journal of Vibration and Control*, vol. 22, no. 4, pp. 920–931, 2016.

[6] J. Yang, J. Xiong, L. Ma, B. Wang, G. Zhang, and L. Wu, "Vibration and damping characteristics of hybrid carbon fiber composite pyramidal truss sandwich panels with viscoelastic layers," *Composite Structures*, vol. 106, pp. 570–580, 2013.

[7] Y. Pennec, B. Djafari-Rouhani, H. Larabi, J. O. Vasseur, and A. C. Hladky-Hennion, "Low-frequency gaps in a phononic crystal constituted of cylindrical dots deposited on a thin homogeneous plate," *Physical Review B - Condensed Matter and Materials Physics*, vol. 78, p. 104105, 2008.

[8] K. H. Matlack, A. Bauhofer, S. Krödel, A. Palermo, and C. Daraio, "Composite 3D-printed metastructures for low-frequency and broadband vibration absorption," *Proceedings of the National Academy of Sciences*, p. 201600171, 2016.

[9] M. Wormser, F. Wein, M. Stingl, and C. Körner, "Design and additive manufacturing of 3D phononic band gap structures based on gradient based optimization," *Materials*, vol. 10, no. 10, p. 1125, 2017.

[10] M. Ruzzene and F. Scarpa, "Control of wave propagation in sandwich beams with auxetic core," *Journal of intelligent material systems and structures*, vol. 14, no. 7, pp. 443–453, 2003.

[11] B. Sharma and C.-T. Sun, "Local resonance and Bragg bandgaps in sandwich beams containing periodically inserted resonators," *Journal of Sound and Vibration*, vol. 364, pp. 133–146, 2016.

[12] Y. Yu, N. G. Naganathan, and R. V. Dukkipati, "Literature review of automotive vehicle engine mounting systems," *Mechanism and Machine Theory*, vol. 36, pp. 123–142, 2001.

[13] L.-E. Ooi and Z. M. Ripin, "Optimization of an engine mounting system with consideration of frequency-dependent stiffness and loss factor," *Journal of Vibration and Control*, vol. 22, no. 10, pp. 2406–2419, 2016.

[14] M. D. Rao, "Recent applications of viscoelastic damping for noise control in automobiles and commercial airplanes," *Journal of Sound and Vibration*, vol. 262, pp. 457–474, 2003.

[15] Z. Kang, X. Zhang, S. Jiang, and G. Cheng, "On topology optimization of damping layer in shell structures under harmonic excitations," *Structural and Multidisciplinary Optimization*, vol. 46, pp. 51–67, 2012.

[16] K. S. Yun and S. K. Youn, "Topology optimization of viscoelastic damping layers for attenuating transient response of shell structures," *Finite Elements in Analysis and Design*, vol. 141, pp. 154–165, 2018.

[17] D. Chronopoulos, I. Antoniadis, and T. Ampatzidis, "Enhanced acoustic insulation properties of composite metamaterials having em-

bedded negative stiffness inclusions," *Extreme Mechanics Letters*, vol. 12, pp. 48–54, 2016.

[18] L. Salari-Sharif, S. M. Ryan, M. Pelacci, J. K. Guest, L. Valdevit, and S. Szyniszewski, "Damping of selectively bonded 3D woven lattice materials," *Scientific Reports*, vol. 8, no. 3, p. 14572, 2018.

[19] P. Gardonio, "Review of Active Techniques for Aerospace Vibro-Acoustic Control," *Journal of Aircraft*, vol. 39, no. 2, pp. 206–214, 2002.

[20] E. J. J. Doppenberg, A. P. Berkhoff, and M. van Overbeek, "Smart materials and active noise and vibration control in vehicles," in *Advances in Automotive Control 2001*, 2001.

[21] D. Mayer, J. Militzer, and T. Bein, "Integrated Solutions for Noise and Vibration Control in Vehicles," *SAE International Journal of Passenger Cars - Mechanical Systems*, vol. 7, pp. 1183–1193, 2014.

[22] M. I. Hussein, M. J. Leamy, and M. Ruzzene, "Dynamics of phononic materials and structures: Historical origins, recent progress, and future outlook," *Applied Mechanics Reviews*, vol. 66, no. 4, p. 40802, 2014.

[23] M. I. Hussein, G. M. Hulbert, and R. A. Scott, "Dispersive elastodynamics of 1D banded materials and structures: analysis," *Journal of sound and vibration*, vol. 289, no. 4, pp. 779–806, 2006.

[24] M. I. Hussein, G. M. Hulbert, and R. A. Scott, "Dispersive elastodynamics of 1D banded materials and structures: design," *Journal of Sound and Vibration*, vol. 307, no. 3-5, pp. 865–893, 2007.

[25] R. Martínez-Sala, J. Sancho, J. V. Sánchez, V. Gómez, J. Llinares, and F. Meseguer, "Sound attenuation by sculpture," *Nature*, vol. 378, no. 6554, pp. 241–241, 1995.

[26] Z. Liu, X. Zhang, Y. Mao, Y. Y. Zhu, Z. Yang, C. T. Chan, and P. Sheng, "Locally resonant sonic materials," *Science*, vol. 289, no. 5485, pp. 1734–1736, 2000.

[27] L. Liu and M. I. Hussein, "Wave motion in periodic flexural beams and characterization of the transition between Bragg scattering and local resonance," *Journal of Applied Mechanics*, vol. 79, no. 1, p. 11003, 2012.

[28] J. S. Chen and C. T. Sun, "Wave propagation in sandwich structures with resonators and periodic cores," *Journal of Sandwich Structures & Materials*, vol. 15, no. 3, pp. 359–374, 2013.

[29] A. Spadoni, M. Ruzzene, S. Gonella, and F. Scarpa, "Phononic properties of hexagonal chiral lattices," *Wave Motion*, vol. 46, pp. 435–450, 2009.

[30] C. Yilmaz and N. Kikuchi, "Analysis and design of passive low-pass filter-type vibration isolators considering stiffness and mass limitations," *Journal of Sound and Vibration*, vol. 293, no. 1-2, pp. 171–195, 2006.

[31] C. Yilmaz and G. Hulbert, "Theory of phononic gaps induced by inertial amplification in finite structures," *Physics Letters A*, vol. 374, no. 34, pp. 3576–3584, 2010.

[32] G. Acar and C. Yilmaz, "Experimental and numerical evidence for the existence of wide and deep phononic gaps induced by inertial amplification in two-dimensional solid structures," *Journal of Sound and Vibration*, vol. 332, no. 24, pp. 6389–6404, 2013.

[33] O. Yuksel and C. Yilmaz, "Shape optimization of phononic band gap structures incorporating inertial amplification mechanisms," *Journal of Sound and Vibration*, vol. 355, pp. 232–245, 2015.

[34] N. M. M. Frandsen, O. R. Bilal, J. S. Jensen, and M. I. Hussein, "Inertial amplification of continuous structures: Large band gaps from

small masses," *Journal of Applied Physics*, vol. 119, no. 12, p. 124902, 2016.

[35] J. Li and S. Li, "Generating ultra wide low-frequency gap for transverse wave isolation via inertial amplification effects," *Physics Letters A*, vol. 382, no. 5, pp. 241–247, 2018.

[36] K. F. Graff, *Wave motion in elastic solids*. Courier Corporation, 1991.

[37] L. Brillouin, *Wave propagation in periodic structures: electric filters and crystal lattices*. McGrawHil, 1946.

[38] J. N. Reddy, *Mechanics of laminated composite plates: theory and analysis*. CRC Press, 1997.

[39] J. M. Whitney and N. J. Pagano, "Shear deformation in heterogeneous anisotropic plates," *Journal of Applied Mechanics*, vol. 37, no. 4, pp. 1031–1036, 1970.

[40] F. G. Leppington, E. G. Broadbent, and K. H. Heron, "The Acoustic Radiation Efficiency of Rectangular Panels," *Proceedings of the Royal Society A: Mathematical, Physical and Engineering Sciences*, vol. 382, no. 1783, pp. 245–271, 1982.

[41] F. G. Leppington, K. H. Heron, and E. G. Broadbent, "Resonant and non–resonant transmission of random noise through complex plates," in *Proceedings of the Royal Society of London A: Mathematical, Physical and Engineering Sciences*, vol. 458, pp. 683–704, The Royal Society, 2002.

[42] S. S. Alieldin, A. E. Alshorbagy, and M. Shaat, "A first-order shear deformation finite element model for elastostatic analysis of laminated composite plates and the equivalent functionally graded plates," *Ain Shams Engineering Journal*, vol. 2, no. 1, pp. 53–62, 2011.

[43] H. T. Thai and D. H. Choi, "A simple first-order shear deformation theory for laminated composite plates," *Composite Structures*, vol. 106, pp. 754–763, 2013.

[44] G. Kurtze and B. G. Watters, "New wall design for high transmission loss or high damping," *The Journal of the Acoustical Society of America*, vol. 31, no. 6, pp. 739–748, 1959.

[45] C. L. Dym and M. A. Lang, "Transmission of sound through sandwich panels," *The Journal of the Acoustical Society of Amrica*, vol. 56, pp. 1523–1532, 1974.

[46] R. D. Ford, P. Lord, and A. W. Walker, "Sound transmission through sandwich constructions," *Journal of Sound and Vibration*, vol. 5, no. 1, pp. 9–21, 1967.

[47] V. S. Sokolinsky and S. R. Nutt, "Consistent higher-order dynamic equations for soft-core sandwich beams," *AIAA journal*, vol. 42, no. 2, pp. 374–382, 2004.

[48] G. Wang, S. Chen, and J. Wen, "Low-frequency locally resonant band gaps induced by arrays of resonant shunts with Antoniou's circuit: experimental investigation on beams," *Smart Materials and Structures*, vol. 20, no. 1, p. 015026, 2011.

[49] T. Wang, V. S. Sokolinsky, S. Rajaram, and S. R. Nutt, "Assessment of sandwich models for the prediction of sound transmission loss in unidirectional sandwich panels," *Applied Acoustics*, vol. 66, no. 3, pp. 245–262, 2005.

[50] T. Wang, S. Li, S. Rajaram, and S. R. Nutt, "Predicting the sound transmission loss of sandwich panels by statistical energy analysis approach," *Journal of Vibration and Acoustics*, vol. 132, p. 11004, 2010.

[51] R. H. Lyon, R. G. DeJong, and M. Heckl, *Theory and application of Statistical Energy Analysis*. Butterworth-Heinemann, 1995.

[52] S. Finnveden, "Evaluation of modal density and group velocity by a finite element method," *Journal of Sound and Vibration*, vol. 273, no. 1-2, pp. 51–75, 2004.

[53] E. Barbieri, A. Cammarano, S. D. Rosa, and F. Franco, "Waveguides fo a composite plate by using the Spectral Finite Element Approach," *Journal of Vibration and Control*, vol. 15, no. 3, pp. 347–367, 2009.

[54] V. Cotoni, R. S. Langley, and P. J. Shorter, "A statistical energy analysis subsystem formulation using finite element and periodic structure theory," *Journal of Sound and Vibration*, vol. 318, no. 4, pp. 1077–1108, 2008.

[55] S. Ghinet and N. Atalla, "Vibro-acoustic behaviors of flat sandwich composite panels," *Transactions of the Canadian Society for Mechanical Engineering*, vol. 30, no. 4, pp. 473–493, 2006.

[56] S. Ghinet, N. Atalla, and . Osman, "The transmission loss of curved laminates and sandwich composite panels," *The Journal of the Acoustical Society of America*, vol. 118, pp. 774–790, 2005.

[57] S. Ghinet and N. Atalla, "Modeling thick composite laminate and sandwich structures with linear viscoelastic damping," *Computers and Structures*, vol. 89, no. 15-16, pp. 1547–1561, 2011.

[58] D. J. Mead, "A general theory of harmonic wave propagation in linear periodic systems with multiple coupling," *Journal of Sound and Vibration*, vol. 27, no. 2, pp. 235–260, 1973.

[59] L. Hinke, B. R. Mace, and M. J. Brennan, "Finite Element Analysis of Waveguides," *Institute of Sound and Vibration Research Technical Memorandum*, no. 932, 2004.

[60] D. M. Mead, "Wave propagation in continuous periodic structures: research contributions from Southampton, 1964–1995," *Journal of sound and vibration*, vol. 190, no. 3, pp. 495–524, 1996.

[61] B. R. Mace and E. Manconi, "Modelling wave propagation in two-dimensional structures using finite element analysis," *Journal of Sound and Vibration*, vol. 318, no. 4, pp. 884–902, 2008.

[62] E. Manconi and B. R. Mace, "Estimation of the loss factor of viscoelastic laminated panels from finite element analysis," *Journal of Sound and Vibration*, vol. 329, no. 19, pp. 3928–3939, 2010.

[63] C. D. Johnson and D. A. Kienholz, "Finite element prediction of damping in structures with constrained viscoelastic layers," *AIAA Journal*, vol. 20, no. 9, pp. 1284–1290, 1982.

[64] E. Manconi, B. R. Mace, and R. Garziera, "The loss-factor of prestressed laminated curved panels and cylinders using a wave and finite element method," *Journal of Sound and Vibration*, vol. 332, pp. 1704–1711, 2013.

[65] D. Chronopoulos, B. Troclet, M. Ichchou, and O. Bareille, "On the vibroacoustic response of aerospace sandwich structures: Bridging the gap between experimental and numerical results," in *Proceedings of the International Conference on Noise and Vibration Engineering ISMA 2012*, pp. 1693–1704, Proceedings of ISMA2012, 2012.

[66] D. Chronopoulos, B. Troclet, M. Ichchou, and J. P. Lainé, "A unified approach for the broadband vibroacoustic response of composite shells," *Composites Part B: Engineering*, vol. 43, no. 4, pp. 1837–1846, 2012.

[67] D. Chronopoulos, M. Ichchou, B. Troclet, and O. Bareille, "Computing the broadband vibroacoustic response of arbitrarily thick layered panels by a wave finite element approach," *Applied Acoustics*, vol. 77, pp. 89–98, 2014.

[68] C. Droz, C. Zhou, M. N. Ichchou, and J. P. Lainé, "A hybrid wave-mode formulation for the vibro-acoustic analysis of 2D periodic structures," *Journal of Sound and Vibration*, vol. 363, pp. 285–302, 2016.

[69] Y. Waki, B. R. Mace, and M. J. Brennan, "Numerical issues concerning the wave and finite element method for free and forced vibrations of waveguides," *Journal of Sound and Vibration*, vol. 327, no. 1-2, pp. 92–108, 2009.

[70] R. Chandra, S. Singh, and K. Gupta, "Damping studies in fiber-reinforced composites a review," *Composite Structures*, vol. 46, no. 1, pp. 41–51, 1999.

[71] M. Maheri and R. Adams, "Vibration Properties of Structural FRP Composites.," *JSME International Journal Series A*, vol. 42, no. 3, pp. 307–320, 1999.

[72] D. Saravanos and C. Chamis, "Tailoring of Composite Links for Optimal Damped Elasto-Dynamic Performance," tech. rep., NASA, Cleveland, Ohio, 1989.

[73] M. Jaber, H. Schneeweiss, J. Bös, and T. Melz, "Vibrational Energy Flow in Carbon Composite Structures," in *Inter.Noise*, (Melbourne), pp. 1–17, 2014.

[74] M. Akbulut and H. Erol, "Damping layer application in design of robust battery pack for space equipment," *Applied Acoustics*, vol. 150, pp. 81–88, 2019.

[75] T. Bein, S. Elliott, L. Ferralli, M. Casella, J. Meschke, E.-U. Saemann, F.-K. Nielsen, and W. Kropp, "Integrated Solutions for Noise & Vibration Control in Vehicles," *Procedia - Social and Behavioral Sciences*, vol. 48, pp. 919–931, 2012.

[76] M. Furukava, S. Gerges, M. M. Neves, and B. J. L. Coelho, "Analysis of structural damping performance in passenger vehicles chasis.," *The Journal of the Acoustical Society of America*, vol. 126, no. 4, p. 2280, 2009.

[77] M. Assarar, W. Zouari, R. Ayad, H. Kebir, and J.-M. Berthelot, "Improving the damping properties of carbon fibre reinforced composites by interleaving flax and viscoelastic layers," *Composites Part B: Engineering*, vol. 152, pp. 248–255, 2018.

[78] F. Duvigneau, S. Koch, E. Woschke, and U. Gabbert, "An effective vibration reduction concept for automotive applications based

on granular-filled cavities," *Journal of Vibration and Control*, vol. 24, no. 1, pp. 73–82, 2018.

[79] W. P. Syam, W. Jianwei, B. Zhao, I. Maskery, W. Elmadih, and R. Leach, "Design and analysis of strut-based lattice structures for vibration isolation," *Precision Engineering*, vol. 52, pp. 494–506, 2017.

[80] J. Yang, J. Xiong, L. Ma, G. Zhang, X. Wang, and L. Wu, "Study on vibration damping of composite sandwich cylindrical shell with pyramidal truss-like cores," *Composite Structures*, vol. 117, pp. 362–372, 2014.

[81] J.-S. Yang, L. Ma, R. Schmidt, G. Qi, K.-U. Schröder, J. Xiong, and L.-Z. Wu, "Hybrid lightweight composite pyramidal truss sandwich panels with high damping and stiffness efficiency," *Composite Structures*, vol. 148, pp. 85–96, 2016.

[82] I. Newton, *Philosophiae Naturalis Principia Mathematica*. Royal Society, 1687.

[83] G. Floquet, "Sur les équations différentielles linéaires à coefficients périodiques," in *Annales scientifiques de l'École normale supérieure*, vol. 12, pp. 47–88, 1883.

[84] L. Rayleigh, "XVII. On the maintenance of vibrations by forces of double frequency, and on the propagation of waves through a medium endowed with a periodic structure," *The London, Edinburgh, and Dublin Philosophical Magazine and Journal of Science*, vol. 24, no. 147, pp. 145–159, 1887.

[85] D. J. Mead, "Wave propagation and natural modes in periodic systems: I. Mono-coupled systems," *Journal of Sound and Vibration*, vol. 40, no. 1, pp. 1–18, 1975.

[86] D. J. Mead, "Wave propagation and natural modes in periodic systems: II. Multi-coupled systems, with and without damping," *Journal of Sound and Vibration*, vol. 40, no. 1, pp. 19–39, 1975.

[87] S. Sadat-Saleh, S. Benchabane, F. Baida, M.-P. Bernal, and V. Laude, "Tailoring simultaneous photonic and phononic band gaps," *J. Appl. Phys.*, vol. 106, p. 074912, 2009.

[88] M. Maldovan and E. L. Thomas, "Simultaneous localization of photons and phonons in two-dimensional periodic structures," *Applied Physics Letters*, vol. 88, p. 251907, 2006.

[89] D. Bria, M. B. Assouar, M. Oudich, Y. Pennec, J. Vasseur, and B. Djafari-Rouhani, "Opening of simultaneous photonic and phononic band gap in two-dimensional square lattice periodic structure," *Journal of Applied Physics*, vol. 109, p. 014507, 2011.

[90] Y. Pennec, J. O. Vasseur, B. Djafari-Rouhani, L. Dobrzyński, and P. A. Deymier, "Two-dimensional phononic crystals: Examples and applications," *Surface Science Reports*, vol. 65, pp. 229–291, 2010.

[91] A. Khelif, A. Choujaa, B. Djafari-Rouhani, M. Wilm, S. Ballandras, and V. Laude, "Trapping and guiding of acoustic waves by defect modes in a full-band-gap ultrasonic crystal," *Physical Review B - Condensed Matter and Materials Physics*, vol. 68, p. 214301, 2003.

[92] A. Khelif, P. A. Deymier, B. Djafari-Rouhani, J. O. Vasseur, and L. Dobrzynski, "Two-dimensional phononic crystal with tunable narrow pass band: Application to a waveguide with selective frequency," *Journal of Applied Physics*, vol. 94, no. 3, pp. 1308–1311, 2003.

[93] A. Khelif, A. Choujaa, S. Benchabane, B. Djafari-Rouhani, and V. Laude, "Guiding and bending of acoustic waves in highly confined phononic crystal waveguides," *Applied Physics Letters*, vol. 84, no. 22, pp. 4400–4402, 2004.

[94] S. Benchabane, A. Khelif, J. Y. Rauch, L. Robert, and V. Laude, "Evidence for complete surface wave band gap in a piezoelectric phononic crystal," *Physical Review E - Statistical, Nonlinear, and Soft Matter Physics*, vol. 73, p. 065601, 2006.

[95] A. Khelif, B. Aoubiza, S. Mohammadi, A. Adibi, and V. Laude, "Complete band gaps in two-dimensional phononic crystal slabs," *Physical Review E*, vol. 74, no. 4, p. 046610, 2006.

[96] J. Gomis-Bresco, D. Navarro-Urrios, M. Oudich, S. El-Jallal, A. Griol, D. Puerto, E. Chavez, Y. Pennec, B. Djafari-Rouhani, F. Alzina, A. Martínez, and C. M. Torres, "A one-dimensional optomechanical crystal with a complete phononic band gap," *Nature Communications*, 2014.

[97] S. Mohammadi, A. Eftekhar, A. Khelif, H. Moubchir, R. Westafer, W. Hunt, and A. Adibi, "Complete phononic bandgaps and bandgap maps in two-dimensional silicon phononic crystal plates," *Electronics Letters*, vol. 43, no. 16, 2007.

[98] F.-l. Hsiao, C.-c. Chen, and V. Laude, "Waveguiding inside the complete band gap of a phononic crystal slab," *Physical Review E*, vol. 76, p. 056601, 2007.

[99] J. O. Vasseur, P. A. Deymier, B. Chenni, B. Djafari-Rouhani, L. Dobrzynski, and D. Prevost, "Experimental and Theoretical Evidence for the Existence of Absolute Acoustic Band Gaps in Two-Dimensional Solid Phononic Crystals," *Physical Review Letters*, vol. 86, no. 14, pp. 3012–3015, 2001.

[100] J. O. Vasseur, P. A. Deymier, A. Khelif, P. Lambin, B. Djafari-Rouhani, A. Akjouj, L. Dobrzynski, N. Fettouhi, and J. Zemmouri, "Phononic crystal with low filling fraction and absolute acoustic band gap in the audible frequency range: A theoretical and experimental study," *Physical Review E - Statistical Physics, Plasmas, Fluids, and Related Interdisciplinary Topics*, vol. 65, p. 056608, 2002.

[101] H. Pichard, O. Richoux, and J.-P. Groby, "Experimental demonstrations in audible frequency range of band gap tunability and negative refraction in two-dimensional sonic crystal," *The Journal of the Acoustical Society of America*, vol. 132, no. 4, pp. 2816–2822, 2012.

[102] B. Troia, A. Paolicelli, F. De, and V. M. N. Passaro, "Photonic Crystals for Optical Sensing: A Review," in *Advances in Photonic Crystals*, InTech, 2013.

[103] Y. Pennec, B. D. Rouhani, E. H. El Boudouti, C. Li, Y. El Hassouani, J. O. Vasseur, N. Papanikolaou, S. Benchabane, V. Laude, and A. Martinez, "Simultaneous existence of phononic and photonic band gaps in periodic crystal slabs," *Optics Express*, vol. 18, no. 13, pp. 14301–14310, 2010.

[104] M. H. Lu, L. Feng, and Y. F. Chen, "Phononic crystals and acoustic metamaterials," 2009.

[105] M. N. Armenise, C. E. Campanella, C. Ciminelli, F. Dell'Olio, and V. M. Passaro, "Phononic and photonic band gap structures: Modelling and applications," *Physics Procedia*, vol. 3, pp. 357–364, 2010.

[106] G. Ma and P. Sheng, "Acoustic metamaterials: From local resonances to broad horizons," *Science Advances*, vol. 2, no. 2, p. e1501595, 2016.

[107] A. Qureshi, B. Li, and K. T. Tan, "Numerical investigation of band gaps in 3D printed cantilever-in-mass metamaterials," *Scientific reports*, vol. 6, p. 28314, 2016.

[108] C. Claeys, E. Deckers, B. Pluymers, and W. Desmet, "A lightweight vibro-acoustic metamaterial demonstrator: Numerical and experimental investigation," *Mechanical Systems and Signal Processing*, vol. 70, pp. 853–880, 2016.

[109] F. Warmuth, M. Wormser, and C. Körner, "Single phase 3D phononic band gap material," *Scientific reports*, vol. 7, no. 1, p. 3843, 2017.

[110] O. R. Bilal, A. Foehr, and C. Daraio, "Observation of trampoline phenomena in 3D-printed metamaterial plates," *Extreme Mechanics Letters*, vol. 15, pp. 103–107, 2017.

[111] S. Taniker and C. Yilmaz, "Design, analysis and experimental investigation of three-dimensional structures with inertial amplification

induced vibration stop bands," *International Journal of Solids and Structures*, vol. 72, pp. 88–97, 2015.

[112] A. T. Fabro, D. Beli, J. R. F. Arruda, N. Ferguson, and B. Mace, "Uncertainty analysis of band gaps for beams with periodically distributed resonators produced by additive manufacturing," in *ISMA 2016 Conference on Noise and Vibration Engineering, Belgium*, 2016.

[113] D. Beli and J. R. F. Arruda, "Influence of additive manufacturing variability in elastic band gaps of beams with periodically distributed resonators," in *Proceedings of the 3rd International Symposium on Uncertainty Quantification and Stochastic Modeling, Brazil*, 2016.

[114] J. Jensen and J. Kook, "Coupled Acoustic-Mechanical Bandgaps," *Crystals*, vol. 112, no. 6, pp. 1–12, 2016.

[115] J. Kook and J. S. Jensen, "Investigation of bandgap structure in coupled acoustic-mechanical system," in *45th International Congress and Exposition on Noise Control Engineering: Towards a Quieter Future, INTER-NOISE Hamburg 2016*, 2016.

[116] M. Reynolds, Y. Gao, and S. Daley, "Experimental validation of the band-gap and dispersive bulk modulus behavior of locally resonant acoustic metamaterials," *The Journal of the Acoustical Society of America*, vol. 19, 2013.

[117] N. Olhoff, B. Niu, and G. Cheng, "Optimum design of band-gap beam structures," *International Journal of Solids and Structures*, vol. 49, no. 22, pp. 3158–3169, 2012.

[118] M. I. Hussein, K. Hamza, G. M. Hulbert, R. A. Scott, and K. Saitou, "Multiobjective evolutionary optimization of periodic layered materials for desired wave dispersion characteristics," *Structural and Multidisciplinary Optimization*, vol. 31, no. 1, pp. 60–75, 2006.

[119] M. I. Hussein, K. Hamza, G. M. Hulbert, and K. Saitou, "Tailoring of two-dimensional band-gap materials for broadband frequency

isolation," in *ASME Conference Proceedings eds. Proceedings of the ASME 2007 International Design Engineering Technical Conferences & Computers and Information in Engineering Conference. Las Vegas: ASME*, pp. 485–494, 2007.

[120] O. Sigmund and J. S. Jensen, "Systematic design of phononic band–gap materials and structures by topology optimization," *Philosophical Transactions of the Royal Society of London A: Mathematical, Physical and Engineering Sciences*, vol. 361, no. 1806, pp. 1001–1019, 2003.

[121] R. S. Langley, N. S. Bardell, and P. M. Loasby, "The optimal design of near-periodic structures to minimize vibration transmission and stress levels," *Journal of Sound and Vibration*, vol. 207, no. 5, pp. 627–646, 1997.

[122] C. Zweben, *Composite Materials*. CRC Press, 2007.

[123] D. B. Miracle, S. L. Donaldson, S. D. Henry, W. W. Scott, J. J. Brown Kelly Ferjutz Edward Kubel, and J. Heather Lampman Elizabeth Marquard Beverly Musgrove Mary Jane Riddlebaugh Juli Williamson, "ASM Handbook Volume 21 Composites Prepared under the direction of the ASM International Handbook Committee," tech. rep., 2001.

[124] L. Torre and J. M. Kenny, "Impact testing and simulation of composite sandwich structures for civil transportation," *Composite structures*, vol. 50, no. 3, pp. 257–267, 2000.

[125] H. Ning, G. M. Janowski, U. K. Vaidya, and G. Husman, "Thermoplastic sandwich structure design and manufacturing for the body panel of mass transit vehicle," *Composite Structures*, vol. 80, no. 1, pp. 82–91, 2007.

[126] A. S. Herrmann, P. C. Zahlen, and I. Zuardy, "Sandwich structures technology in commercial aviation," in *Sandwich structures 7: Advancing with sandwich structures and materials*, pp. 13–26, Springer, 2005.

[127] J. Hegger and M. Horstmann, "Light-weight TRC sandwich building envelopes," in *Proceedings of the International Conference Excellence in Concrete Construction through Innovation*, pp. 187–194, 2008.

[128] W. Li, F. Sun, P. Wang, H. Fan, and D. Fang, "A novel carbon fiber reinforced lattice truss sandwich cylinder: fabrication and experiments," *Composites Part A: Applied Science and Manufacturing*, vol. 81, pp. 313–322, 2016.

[129] S. Jiang, F. Sun, H. Fan, and D. Fang, "Fabrication and testing of composite orthogrid sandwich cylinder," *Composites Science and Technology*, vol. 142, pp. 171–179, 2017.

[130] J. V. Nygaard and A. Lyckegaard, "Sandwich beam with a periodical and graded core manufactured using rapid prototyping," *Journal of Sandwich Structures & Materials*, vol. 9, no. 4, pp. 365–376, 2007.

[131] B. Han, K.-K. Qin, B. Yu, Q.-C. Zhang, C.-Q. Chen, and T. J. Lu, "Design optimization of foam-reinforced corrugated sandwich beams," *Composite Structures*, vol. 130, pp. 51–62, 2015.

[132] R. Biagi and H. Bart-Smith, "In-plane column response of metallic corrugated core sandwich panels," *International Journal of Solids and Structures*, vol. 49, no. 26, pp. 3901–3914, 2012.

[133] M. R. M. Rejab and W. J. Cantwell, "The mechanical behaviour of corrugated-core sandwich panels," *Composites Part B: Engineering*, vol. 47, pp. 267–277, 2013.

[134] M. Ruzzene and P. Tsopelas, "Control of wave propagation in sandwich plate rows with periodic honeycomb core," *Journal of engineering mechanics*, vol. 129, no. 9, pp. 975–986, 2003.

[135] Y. Pang and B. Gao, "A new sandwich structure of photonic bandgap," in *Microwave Symposium Digest, 2002 IEEE MTT-S International*, vol. 2, pp. 1157–1160, IEEE, 2002.

[136] Y. Cheng, X. J. Liu, and D. J. Wu, "Band structures of phononic-crystal plates in the form of a sandwich-layered structure," *The Journal of the Acoustical Society of America*, vol. 130, no. 5, pp. 2738–2745, 2011.

[137] X.-f. Liu, Y.-f. Wang, and Y.-s. Wang, "Complete band gaps in sandwich phononic crystal plates," in *Piezoelectricity, Acoustic Waves and Device Applications (SPAWDA), 2011 Symposium on*, pp. 433–436, IEEE, 2011.

[138] S. Jiang, H. Chen, L. Dai, H. Hu, and V. Laude, "Multiple low-frequency broad band gaps generated by a phononic crystal of periodic circular cavity sandwich plates," *Composite Structures*, vol. 176, pp. 294–303, 2017.

[139] H. Badran, M. Tawfik, and H. Negm, "Vibration characteristics of periodic sandwich beams," in *Proceedings of the 13th International Conference on Applied Mechanics and Mechanical Engineering*, 2008.

[140] Z. Guo, M. Sheng, and J. Pan, "Flexural wave attenuation in a sandwich beam with viscoelastic periodic cores," *Journal of Sound and Vibration*, vol. 400, pp. 227–247, 2017.

[141] M. Sheng, Z. Guo, Q. Qin, and Y. He, "Vibration characteristics of a sandwich plate with viscoelastic periodic cores," *Composite Structures*, vol. 206, pp. 54–69, 2018.

[142] Y. Song, L. Feng, J. Wen, D. Yu, and X. Wen, "Reduction of the sound transmission of a periodic sandwich plate using the stop band concept," *Composite Structures*, vol. 128, pp. 428–436, 2015.

[143] Z. Liu, R. Rumpler, and L. Feng, "Broadband locally resonant metamaterial sandwich plate for improved noise insulation in the coincidence region," *Composite Structures*, vol. 200, pp. 165–172, 2018.

[144] V. Birman and G. A. Kardomatea, "Review of current trends in research and applications of sandwich structures," *Composites Part B: Engineering*, vol. 142, pp. 221–240, 2018.

[145] S. Neumark, *Concept of complex stiffness applied to problems of oscillations with viscous and hysteretic damping*. HM Stationery Office, 1962.

[146] S. Adhikari, "Damping modelling using generalized proportional damping," *Journal of Sound and Vibration*, vol. 293, no. 1-2, pp. 156–170, 2006.

[147] F. Tisseur and K. Meerbergen, "The quadratic eigenvalue problem," *SIAM review*, vol. 43, no. 2, pp. 235–286, 2001.

[148] A. Inc, "Stress stiffening," *Ansys ®14.0 Help System*, 2011.

[149] M. Petyt, *Introduction to finite element vibration analysis*. Cambridge university press, 2010.

[150] R. S. Langley, "The modal density of anisotropic structural components," *The Journal of the Acoustical Society of America*, vol. 99, no. 6, pp. 3481–3487, 1996.

[151] P. J. Shorter, "Wave propagation and damping in linear viscoelastic laminates," *Journal of the Acoustical Society of America*, vol. 115, pp. 1917–1925, 2004.

[152] J. Allard and N. Atalla, *Propagation of Sound in Porous Media: Modelling Sound Absorbing Materials 2e*. Wiley, 2009.

[153] I. Duff, R. Grimes, and J. Lewis, "User's Guide for the Harwell-Boeing Sparse Matrix Collection," tech. rep., 1992.

[154] S. Adhikari and M. I. Friswell, "Eigenderivative analysis of asymmetric non-conservative systems," *International Journal for Numerical Methods in Engineering*, vol. 51, no. 6, pp. 709–733, 2001.

[155] D. Chronopoulos, "Design optimization of composite structures operating in acoustic environments," *Journal of Sound and Vibration*, vol. 355, pp. 322–344, 2015.

[156] C. A. Felippa and R. W. Clough, *The finite element method in solid mechanics*. American Mathematical Society, 1970.

[157] T. Coleman, M. A. Branch, and A. Grace, "Optimization toolbox," *For Use with MATLAB. User's Guide for MATLAB 5, Version 2, Release II*, 1999.

[158] A. Dademir, "Forced Vibrations of Pre-Stressed Sandwich Plate-Strip with Elastic Layers and Piezoelectric Core*," *International Applied Mechanics*, vol. 54, no. 4, pp. 480–493, 2018.

[159] S. A. Gelfand, *Essentials of audiology*. Thieme, 2009.